UNIVERSITÀ DEGLI STUDI DI TRIESTE

XXX CICLO DEL DOTTORATO DI RICERCA IN NANOTECNOLOGIE

Study of the growth and of the electronic and structural properties of two-dimentional materials

Settore scientifico-disciplinare: **FIS/03 Fisica della Materia**

DOTTORANDA
Elisabetta TRAVAGLIA

COORDINATORE
Prof.ssa Lucia PASQUATO

SUPERVISORE DI TESI
Dott. Silvano LIZZIT

CO-SUPERVISORE DI TESI
Prof. Alessandro BARALDI

ANNO ACCADEMICO 2016/2017

UNIVERSITY OF TRIESTE

Department of Physics

Graduate School in Nanotechnology, Cycle XXX

PhD Thesis

Study of the growth and of the electronic and structural properties of two-dimensional materials

Supervisor:
Dott. Silvano Lizzit

Cosupervisor:
Prof. Alessandro Baraldi

Candidate:
Elisabetta Travaglia

Academic Year 2016-2017

A Giulio e Teresa

Sommario

Negli ultimi dieci anni, dopo l'isolamento del grafene e lo studio delle sue eccezionali proprietà, la comunità scientifica ha rivolto la propria attenzione ai cristalli bidimensionali (2D), ed in particolare ai dicalcogenuri dei metalli di transizione (TMDCs). Sebbene molto sforzo sia stato profuso per portare la loro produzione su scala industriale e integrarli all'interno dei futuri dispositivi elettronici ed optoelettronici, un metodo che porti alla scalabilità di questi materiali è ancora una sfida. Questa tesi è focalizzata sul meccanismo di crescita dei TMDCs e studia gli aspetti legati al processo di nucleazione e le fasi che portano alla formazione del cristallo, in modo da identificare le condizioni ottimali per promuovere l'estensione dei domini dei layer. Inoltre la tesi investiga i metodi che permettono la produzione di campioni TMDCs con una singola orientazione, consentendo di ottenere una migliore qualità dei layer, grazie alla riduzione del numero di bordi di grano formati dalla coalescenza di isole con diversa orientazione e aprendo strade nuove verso l'applicazione di concetti come la spin-valletronica ai dispositivi di nuova generazione. La prima parte della tesi è dedicata alla crescita di MoS_2 su diversi substrati metallici, come Au(111), Ag(111) e Ag(110), con lo scopo di investigare l'effetto dell'interazione tra il layer sovrastante e il substrato, e l'effetto della simmetria del substrato sulla formazione di layer estesi di MoS_2. Per ottenere layer altamente cristallini formati da domini orientati allo stesso modo, è stato implementato un nuovo protocollo di crescita su Au(111) ed adattato poi per gli altri substrati, sebbene esso su questi ultimi producesse due orientazioni, pur mantenendo alta la cristallinità. È stata caratterizzata la struttura elettronica del MoS_2/Au(111), con particolare interesse alla polarizzazione di spin fuori dal piano delle bande vicino a K e -K della zona di Brillouin. Abbiamo successivamente esplorato la crescita di WS_2 su Au(111) per valutare la versatilità del metodo di crescita da noi sviluppato. Mediante la calibrazione dei parametri di crescita, sono stati ottenuti dei campioni altamente cristallini di WS_2 con una singola orientazione, che sono stati successivamente utilizzati per studiare il coupling elettrone-fonone, derivando quindi preziose informazioni per le applicazioni sui device. L'ultima parte della tesi è dedicata all'intercalazione dell'ossigeno al di sotto del grafene cresciuto su Ir(111), con lo scopo di verificare se la presenza del grefene possa cambiare la geometria degli atomi di ossigeno sull'Ir(111). Comparando i risultati ottenuti dall'adsorbimento dell'ossigeno sull'Ir(111) pulito con quelli in presenza del grafene, è stato possibile vedere che le strutture dell'ossigeno formate sotto il grafene possono essere riprodotte sull'Ir(111) dosando delle specie fortemente ossidanti come l'NO_2, concludendo che il grafene non interferisce in maniera apprezzabile con l'interazione adsorbato-substrato.

Abstract

In the past ten years, after the isolation of graphene and the investigation of its outstanding properties, the scientific community has focused on the study of other two-dimensional (2D) atomic crystals, and particularly on the transition metal dichalcogenides (TMDCs). Though much effort is spent in the perspective of scaling up the production and integrating these materials in future electronic and optoelectronic devices, so far, a way towards sizable growth of 2D-TMDCs is still a challenge. This thesis is focused on the growth mechanism of TMDCs and studies aspects related to the nucleation process and the steps that lead to the formation of the crystals, in order to identify the optimal conditions to promote the increase of the domain size of the layers. In addition, the thesis investigates on the methods to produce TMDCs samples with a single orientation that allows to obtain better quality layers, thanks to the reduced presence of grain boundaries formed by the coalescence of islands with different orientations, and allows to open the path towards novel device concepts such as those based on the spin-valleytronics.

The first part of the thesis is devoted to the growth of MoS_2 on different metallic substrates, namely Au(111), Ag(111) and Ag(110), with the aim of investigating the effect of the interaction between adlayer and substrate, and the effect of the substrate symmetry in the formation of extended layers of MoS_2. In order to obtain a high quality layer with single domain orientation, a new growth protocol was developed on Au(111) and adapted also for the other substrates, where the high quality is presernved but with the presence of two orientations. The electronic structure of the MoS_2/Au(111) sample was characterized, with a special attention to the out-of plane spin polarization of the bands near K and -K points of the Brillouin zone.

We have subsequently explored the growth of single layer WS_2 on Au(111) in order to evaluate the versatility of the developed growth method. By finding the proper growth parameters, we obtained high quality WS_2 samples with a single orientation, that has been subsequently used to study the electron-phonon coupling thus deriving useful information for electronic device applications.

The last part of the thesis is dedicated to the oxygen intercalation under graphene grown on Ir(111), with the aim of verifying whether the presence of graphene changes the adsorption geometry of the oxygen atoms on Ir(111). By comparing the results of oxygen adsorption on the bare Ir surface with those in the presence of graphene, it was possible to see that the oxygen overstructures formed under graphene can be reproduced on bare Ir(111) by dosing strongly oxidizing species such as NO_2, concluding that graphene does not appreciably affect the adsorbate-substrate interaction.

Contents

Chapter 1

Introduction

In 1965 Gordon Moore predicted that the number of transistors per unit area in a microchip would double approximately every two years[1] and this is one of the most accurate prediction in the field of electronics. In fact, semiconductor companies have managed to follow this trend over the past 50 years despite several announcements of an impeding stop given first by concerns about lithography resolution[2], and later, about the tunneling through the thin gate insulator, and the resulting high gate leakage and oxide breakdown[3]. The reason for the reduction of the transistor geometrical size must be sought in the peculiar feature of the silicon planar metal-oxide-semiconductor field-effect transistor (MOSFET), that is, the increase of the performance for digital circuits as its dimensions are reduced[4]. Such geometrical reduction has led to an exponential increase of the switching speed, a decrease of the switching energy, a decrease in the power supply voltage and, obviously, to an increased packing density. However, the merely reduction of the MOSFET dimensions has been possible up to approximately gate lengths of 100-200 nm because of increased degrading effects like the short channel effects and gate oxide tunneling. To overcome these issues, other technology boosters have provided some relief by also allowing an aggressive scale of the supply voltage for the reduction of the power consumption as, for example, new oxides for the gate dielectric in replacement of the SiO_2 (the so called high-k oxides), alternative device architectures (Tri-gate FETs, FinFETs, nanowire FETs), process-induced strain and high-mobility channel materials belonging to the III-V group of the periodic table of elements[5–8], but also more innovative device concepts have been recently explored, such as Tunnel FETs, Negative Capacitance FETs and Piezoelectric FETs. To give an idea about the impressing progress of the silicon based semiconductor manufacturing process, in the early seventies the average MOSFET gate length was about 10μm, whereas in April 2017 Samsung started to sell smartphones with a 10 nm processor[1]. Despite the successful scaling of FETs, a further

[1] http://www.samsung.com/uk/smartphones/galaxy-s8/performance/

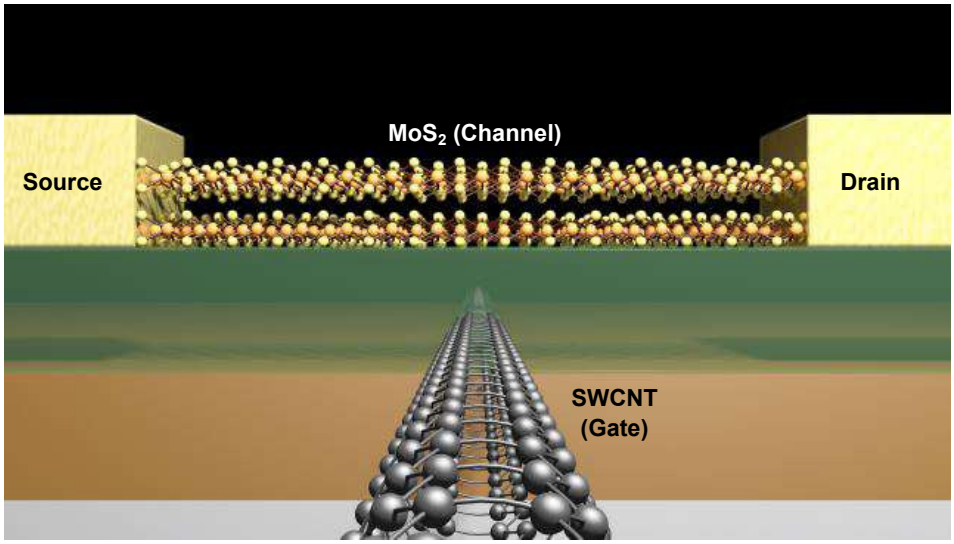

Figure 1.1: Scheme of a FET transistor with a MoS_2 channel and a 1-nanometer single-walled carbon nanotube (SWCNT) gate, adapted from [9].

reduction of the geometrical dimensions by employing the standard industry technology solutions already cited is predicted to be unreliable below 5-nanometer gate lengths because of severe short channel effects thus leading to the necessity of finding new materials and/or architectures to maintain a high device performance at low supply voltage, necessary for the progress of nanoscale technologies. Among them, it has been recently demonstrated that it is possible to produce 1 nm gate transistor using low dimensional materials such as double layer molybdenum disulphide and single walled carbon nanotubes, as shown in the sketch of figure 1.1[9]. This opened a possible new path in the Post-Silicon Era, showing that a technology based on a novel family of materials is possible. This class of materials is very wide and the classification is based according to the number of dimensions which are not confined to the nanoscale range. Hence, one can distinguish between two-dimensional (2D) materials in which quantum confinement occurs along one dimension, one-dimensional (1D) and even zero-dimensional (0D) materials. Due to the quantum confinement, the constraints on the physical dimensions, surface effects and the higher surface-to-volume ratio, the research was boosted towards this field, in order to integrate them in already existing technology or to develop novel applications.

The intense effort made in the field of the 2D materials is also due to the fact that they can be combined to build heterostructures, new materials which electronic structure can be engineered. Two or more 2D materials can be vertically stacked one onto the other to create FET transistors[10], light emitting diodes[11] and photovoltaic systems[12]. Moreover, the preparation

of heterostructures on thin and elastic substrates opens to the possibility of flexible and transparent technology. Finally, two different 2D materials can also be integrated in the same plane and they can be exploited as p-n junctions[13].

1.1 The 2D materials

Among low-dimensional materials, the two dimensional (2D) class gained a lot of interest since the isolation and the development of a reliable process to produce graphene[14]. The 2D family is formed by crystalline materials that do not need to be supported by a substrate to exist and therefore can be isolated as free-standing layers. Thanks to the great effort spent in the field of graphene, a lot of 2D systems, such as hexagonal boron nitride (h-BN), transition metal dichalcogenides (TMDCs), borophene, stanene and phosphorene, have been deeply studied. Ideally speaking, every layered material could be cleaved down to their atomic planes[14]. However, some issues must be taken into account: as the melting temperature decreases with dimensionality, 3D materials that melt at sufficiently high temperature are likely to be stable in their 2D form at room temperature. Moreover, 3D materials that are chemically inert with no decomposed surface layer in air, are suitable to produce 2D materials when exfoliated. On the other hand, the stability of 2D materials depends also on the semiconducting or insulating character that, as compared to the metallic one, results in lower reactivity. These are the reasons why nowadays 2D crystals that are stable under ambient conditions are approximately a dozen. Some of the most studied 2D materials are discussed in the following.

Graphene. Graphene is an allotrope of carbon, in the form of a single layer of carbon atoms arranged in a honeycomb lattice. The 1D nanotubes and 3D graphite are other carbon structures related to it. Even if the study of graphene is not new, research in this field has been boosted by the isolation of this material in 2004 by Novoselov and Geim, who were awarded with the Nobel prize just six years later, in 2010. This material gained a lot of attention from the scientific community thanks to its exotic properties: it shows high carrier mobility at room temperature ($2.5 \times 10^5\,\mathrm{cm^2V^{-1}s^{-1}}$)[15], high thermal conductivity (more than $3000\,\mathrm{Wm^{-1}K^{-1}}$)[16], high Young's modulus (around 1 TPa)[17], good optical transparency (97.7 %)[18] and an anomalous Hall effect[19]. Moreover it shows linear pi-bands dispersion at the Fermi Level at the K-point of the Brillouin zone[20], as theoretically predicted by Wallace already in 1947[21]. Thanks to all these unique properties, together with its very high stability under ambient conditions, graphene is suitable for a lot of different applications such as spintronic device[22], molecular sensing[23], flexible electronics[24] and other devices. There are also several graphene derivatives, such as fluorographene, a stable insulator, that can be

produced by fluorination of graphene[25]; graphane, the fully hydrogenated graphene[26]; graphene oxide[27] and boron carbon nitride[28, 29].

Hexagonal boron nitride. Hexagonal boron nitride single layer is another very important 2D material, being an insulator with a band gap of 5.9 eV[30]. Isostructural to graphene, it is a single sheet of alternating boron and nitrogen atoms arranged in a sp^2-honeycomb lattice[31], with strong covalent bonds, that give rise to its high mechanical strength, good thermal conductivity, excellent chemical and thermal stability[32]. Since the lattice mismatch between h-BN and graphene is very small, it can be exploited as an insulating layer to build graphene devices. Indeed it was shown that the carrier mobility is one order of magnitude better with respect to graphene on SiO_2[33].

2D oxides. 2D oxides, like for example MnO_2, TiO_2, TaO_3 and V_2O_5[2], raised attention for their potential use as high-k dielectrics in FET devices and because, being oxides, they are quite inert, even if they tend to react with molecules such water and hydrogen and may lose oxygen. Layered oxides are commonly polycrystalline and mechanical exfoliation can normally be used with high quality crystals. This entails that only a few 2D oxides can be obtained via exfoliation method. Therefore, a generalized bottom-up strategy for controlled synthesis of metal oxides in 2D nanostructures is highly desirable to satisfy the demand in various applications related to sensing, catalysis, energy storage and electronic devices [35].

1.2 The transition metal dichalcogenides

1.2.1 Structure and properties

Transition metal dichalcogenides (TMDCs) are an important class of 2D materials. The single layer (SL) consists of three atomic sheets, one of a transition metal from group 4-10 (M; typically Mo, W, Nb, Re, Ni or V), between two layers of a chalcogen (X; typically S, Se or Te) with a stoichiometry MX_2. The atoms inside the three layers are hexagonally packed and the M atoms can have octahedral or trigonal prismatic coordination as shown in figure 1.2. Moreover, bulk crystals can crystallize in different forms, with different properties and stability, depending on the M atom coordination and on the stacking order of the SL. M and X atoms are covalently bonded within the molecular layer whereas the MX_2 sheets mutually interact through van der Waals forces. Depending on the coordination and oxidation state of the metal atom, bulk TMDCs can be metallic, like NbS_2 and VS_2, semiconducting such as MoS_2 and WS_2 or insulating like HfS_2. We note, incidentally, that the interest toward these materials is not recent, indeed the

[2]Note that they can exhibit stoichiometry different from their 3D counterparts after intercalation and exfoliation[34]

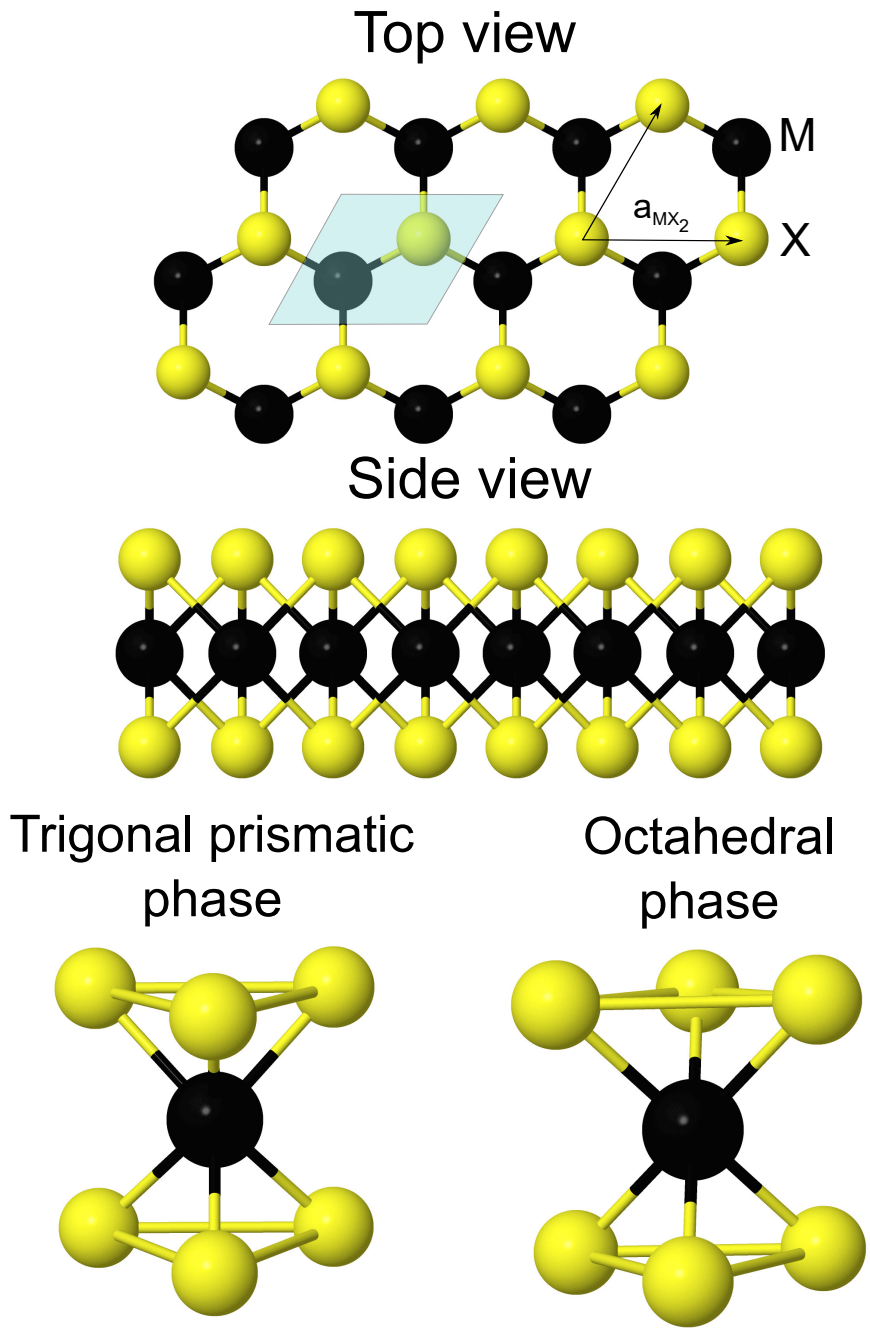

Figure 1.2: TMDCs general structure. MX_2 top view where the unit cell is highlighted with a light blue rhombus and the lattice constant a_{MX_2} with the arrows. MX_2 side view. Trigonal prismatic and octahedral MX_2 phases.

structure of MoS_2 was already determined in 1923[36] and used for industrial applications as a dry lubricant thanks to its low friction coefficient given by its layered structure[37, 38] and to the fact that it is relatively inert in ambient air. Moreover, it is exploited in the industrial field as a catalyst for the hydrodesulfurization process for the removal of sulfur from petroleum fractions[39].

TMDCs, and in particular SL MoS_2, have attracted remarkable attention for future electronic devices and many studies have been performed on characterizing the electronics and optical properties[40–44]. In fact, by scaling down to single layer, TMDCs show unique optical and electronic properties that differ from the ones of the bulk TMDCs because of the lateral confinement. In particular, MoS_2 exhibits a transition from an indirect band gap (E_g=1.29 eV) in its bulk form to a direct band gap (E_g=1.90 eV) in the monolayer form. This confers a high absorbance coefficient and a high efficiency in the core-hole couples in the photo-excitation process, allowing, for instance, the production of high sensitivity photo-transistors, opening a path for the use of this material in the nanotechnology field, in the optoelectronic integrated circuits[40–42], light sensors, biomedical imaging[45], as well as for field effect transistors (FETs) based on the interband tunnel effect for low power device applications[46, 47] The bandgap engineering as a function of the number of SLs and of the applied stressors[48], together with the scalability of the MoS_2, its band structure, and the low density of defects at the MoS_2-dielectric interface[46] makes it a promising candidate for future generations of switching FET devices featuring nanoscale dimensions and few devices have already been demonstrated in the literature with on/off ratios larger that 10^8 and room temperature mobility larger than $200\,cm^2V^{-1}s^{-1}$[9, 49, 50].

Another interesting feature of TMDCs comes from the possibility to exploit degrees of freedom that go beyond the standard one based on the electronic charge to encode and process information. In fact, current technology exploits the charge of electrons as a mean for storing bits of information by probing it through electric fields, but additional degrees of freedom given by the spin of electrons and the valley to which they belong can also be exploited, leading to spin- and valleytronic based devices. Spin-dependent electron transport phenomena in solid-state devices are studied by more than 30 years[51] and spintronics aims to control the carrier spin to store, manipulate and retrieve bits of information to make, at least from theoretical point of view, data more robust and reproducible, preventing misleading readings[52–54], due to the shielding from undesired electric fluctuations always present in standard charged-based devices. Concerning the valleytronics, the concept of valleys comes from the inspection of the band structure of a crystal, that is the dispersion of the allowed electronic states in the energy-momentum space, in which can be identified local maximum in the valence band or local minima in the conduction band that are referred to as a valley. Similar to the

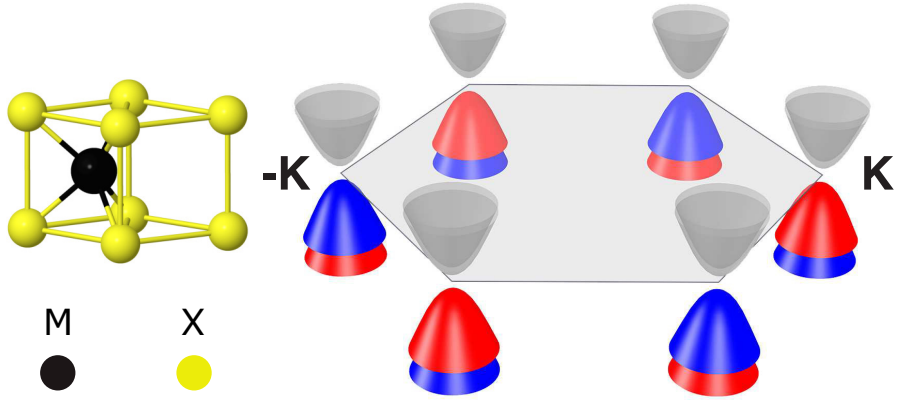

Figure 1.3: MX_2 structure and schematic Brillouin zone band structure. The colors of the split valence band maximum (blue/red) refer to the different spin orientation of these states, which is inverted in K and -K points of the Brillouin zone.

spintronics, valleytronic aims at controlling the carriers by localizing them to one specific valley (valley polarization), leading to a pseudospin index that is associated with the valley type. Pioneering experiments have successfully demonstrated the capability to induce valley and spin polarization in AlAs[55, 56] and bismuth[57] and, with the discovery of graphene, the manipulation of the valley index has become more attractive[58–61]. However, the existence of inversion symmetry in the graphene crystal structure makes the control of the valley degree of freedom quite complicated[62] and some efforts have been made in this direction to break the inversion symmetry by using external electric fields[59].

In this context, SL TMDCs play an important role because of manifold reasons. In fact, it is well known that in the SL limit these materials have non-equivalent degenerate valleys in the valence band at the K and K' points of the Brillouin zone with a strong spin-splitting as shown in figure 1.3. In such SL, the inversion symmetry is explicitly broken and, therefore, electrons in the K and K' valleys have finite but opposite Berry curvature that gives rise to interesting topological transport properties[53, 56, 59]. This means that electrons in the two different K-valleys experience effective magnetic fields that are proportional to the Berry curvature with equal magnitudes but opposite signs[59, 62]. This aspect is relevant because it defines the optical pumping selection rules that allow optical pumping of valley-polarized carriers by circularly polarized photons and it is responsible for the Valley Hall Effect (analogous to the spin Hall effect[63, 64]) in which electrons from K and K' valleys in the presence of a in-plane longitudinal electric field experience opposite forces that make them drift perpendicularly to the

electric field[53–60, 65]. Therefore, in the case of a net valley polarization (different population of the two valleys) obtained, for example, with optical pumping, the valley polarization can be detected by measuring a voltage drop at the edges of the SL TMDCs[53, 62]. Moreover, SL TMDCs with heavy metal atoms show a strong spin-orbit coupling originated from the d orbitals that lead to nearly fully spin polarized K-valleys. This coupling between spin and valleys translates into spin- and valley-dependent optical selection rules and carriers with various combination of valley and spin indexes can be selectively optically-excited[53]. In addition, a strong stability (long lifetime) of such a spin- and valley- polarized carriers in TMDCs is predicted because of two aspects: the flipping of the valley occurs over long distances in the k-space since K-valleys are separated by wave vectors comparable with the size of Brillouin zone thus requiring atomic scale scatterers. Furthermore, elastic scattering of carriers lying in the K-valleys requires simultaneous valley and spin flip supported by atomic scale magnetic scatterers[53].

1.2.2 Growth approaches for the synthesis of TMDCs

In order to produce single-layer TMDCs, different approaches have been developed and they can be divided into top-down and bottom-up approaches. The top-down approaches include the micromechanical exfoliation, which is nowadays the easiest and fastest method to obtain two-dimensional materials and indeed, devices based on exfoliated MoS_2 have already been produced[66]. This method, in the case of MoS_2, consists in exfoliating from commercially available crystals of molybdenite a single layer of MoS_2 through repeated peeling of the bulk crystal by using an adhesive scotch tape. However, even though this approach allows the production of single flake of high purity, it is not suitable for large scale applications because of the lack of reproducibility in terms of thickness and size of the flakes[67]. Also liquid exfoliation, consisting in dispersing layered compounds in common organic solvents[68], and intercalation of lithium ions using an electrochemical set-up do not lead to satisfactory results[69]. Within the bottom-up methods we find the thermolysis of compounds containing Mo or W and S atoms decomposing in oleylamine, an organic surfactant[70], or layers of ammonium thiomolybdate $(NH_4)MoS_4$ in presence of S[71]. TMDCs can also be grown through sulphurization of films containing metallic atoms in solid phase[72]. Chemical vapor deposition (CVD), starting from the metal and the chalcogen[72], or from metal oxides and chalcogen precursors[73–75], is the most promising method towards large-scale production of extended monocrystalline single layers, though the presence of defects like grain boundaries and the lack of control on the homogeneity of the layer are unavoidable. On the other hand, another approach that gives good results in growing high quality single layer TMDCs is the physical vapor deposition (PVD), starting from a metal, and a gaseous S source, such as H_2S[76]. It allows the synthesis of highly pure

single layer MoS_2 nano-islands, that are a good template for the study of the physics of this material.

1.3 Our aim

As mentioned before, one of the most promising methods to produce highly crystalline single layer TMDCs is the PVD. However, it is important to stress the fact that, so far, this method has allowed to obtain nano-islands, difficultly compatible with the micro and nanofabrication processes for the integration in the future devices. Therefore, in the perspective of scaling up the production, it is necessary to find a way towards sizable growth of 2D layers. The first point in order to achieve this result is to better understand the growth mechanism. A turning point in this sense can be obtained through a deep comprehension of the nucleation process and the detailed study of the steps that lead to the formation of the crystals, such as transition metal and chalcogen adsorption and their bond, and, how the temperature affects the growth. Only in this way, it is possible to identify the optimal conditions to promote the increase of the domain size of the layers. Moreover, for a better quality of the layer, the presence of domains with a single orientation is highly desirable because of the reduced presence of grain boundaries, formed by the coalescence of islands. In addition, singly oriented domains open the path to novel applications such as spin- and valleytronics and the possibility of studying in details all the electronic properties of these materials. For these reasons, the aim of this thesis is to provide an insight on the growth of the TMDCs on transition metal substrates and a detailed investigation of their structural and electronic properties are presented in the following chapters.

With the purpose of improving the quality of these layers, much effort was spent to carefully study the PVD growth process reported in the literature[76], consisting in dosing the sample at room temperature with Mo in H_2S atmosphere, followed by thermal annealing to produce the MoS_2 layer (Temperature Programmed Growth (TPG)). In Chapter 3 we describe the growth of MoS_2 on Au(111) substrate. In the first part, we analyzed the processes involved in the transition between the sulfided Mo clusters on the gold surface to single layer MoS_2. Fast-XPS measurements were used to study the evolution of the intermediate species present on the surface and their role in the formation of MoS_2. In the second part of the chapter, we focused on another crucial point, namely the possibility of growing MoS_2 with a single domain orientation with respect to the Au substrate. In this view, a new growth protocol, consisting in keeping the sample at high temperature during dose (High Temperature Growth (HTG)), was developed. This method promoted the MoS_2 formation from the beginning of the growth procedure and the final layer showed very high quality. The important outcome of this

procedure is the formation of MoS_2 domains of a single orientation, determined by comparing XPD results with multiple scattering simulations. The unique orientation of the layer allowed us to measure the complete out-of plane spin polarization of the bands near K and -K points of the Brillouin zone.

After having developed a new growth protocol that leads to undeniable advantages, we wanted to understand if this approach could have been applied for the growth of MoS_2 on a different substrate. We studied its growth on another high symmetry surface, Ag(111), with the aim of investigating the effect of a higher interaction between adlayer and substrate in the formation of extended layers of MoS_2. We used the HTG approach and by means of fast-XPS, we studied the dynamics of the process which results in the direct formation of MoS_2. The results obtained have been summarized in chapter 4, where the we show that indeed extended layers of MoS_2 can be formed, but with the presence of two antiparallel domains in equal proportion. Moreover, the XPS data analysis suggested the metallicity of the layer due to the interaction with the substrate. With the aim of investigating the effect of the substrate symmetry, we chose Ag(110) and we successfully grew MoS_2 through a combination of TPG and HTG methods, obtaining a well ordered layer with equal amount of the two antiparallel domains, as expected from the symmetry of the subtrate.

Once the growth of MoS_2 was fully characterized, in chapter 5, we explored the growth of WS_2 on Au(111) with the HTG growth method. WS_2 was chosen because, like MoS_2, it can be exploited for the creation of future devices for the storage or transmission of quantum information, due to the strong lifting of the spin-degeneracy in the band structure, in particular near the valence band (VB) maximum at K point. By using fast-XPS during growth it was possible to find the proper growth parameters to obtain just one single orientation of the layer. The high quality WS_2 samples obtained where then used for the study of many body effects in this material such as the branch dependent electron-phonon coupling strength.

Chapter 6 is devoted to another very interesting 2D material, that is graphene. We studied the oxygen intercalation under graphene grown on Ir(111). It is known that graphene can be successfully decoupled from the substrate by oxygen, leading to a quasi free-standing graphene. However, the aim of this study was to verify whether the presence of graphene changes the adsorption geometry of the oxygen atoms on Ir(111). In order to verify this aspect, we compared the results of oxygen adsorption on the bare Ir surface with those in the presence of graphene; it was possible to see that the graphene layer allows to reach a higher oxygen coverage on Ir, with the oxygen atoms sitting always in the same adsorption site. However, the same structures can be reproduced on bare Ir(111) by dosing strongly oxidizing species such as NO_2, concluding that graphene does not affect the adsorbate-substrate interaction.

References

[1] Moore, G. E. Cramming more components onto integrated circuits, Reprinted from Electronics, volume 38, number 8, April 19, 1965, pp.114 ff. *IEEE Solid-State Circuits Society Newsletter* **2006**, *11*, 33–35.

[2] Wallmark, J. T. Fundamental physical limits in integrated electronic circuits. *Institute of Physics Conference* **1975**, *25*, 133–167.

[3] Stathis, J. H.; DiMaria, D. J. Reliability projection for ultra-thin oxides at low voltage. International Electron Devices Meeting 1998. Technical Digest (Cat. No.98CH36217). 1998; pp 167–170.

[4] Ferain, I.; Colinge, C. A.; Colinge, J.-P. Multigate transistors as the future of classical metal-oxide-semiconductor field-effect transistors. *Nature* **2011**, *479*, 310–316.

[5] Ghani, T. et al. A 90nm high volume manufacturing logic technology featuring novel 45nm gate length strained silicon CMOS transistors. IEEE International Electron Devices Meeting 2003. 2003; pp 11.6.1–11.6.3.

[6] Tyagi, S. et al. An advanced low power, high performance, strained channel 65nm technology. IEEE InternationalElectron Devices Meeting, 2005. IEDM Technical Digest. 2005; pp 245–247.

[7] Mistry, K. et al. A 45nm Logic Technology with High-k+Metal Gate Transistors, Strained Silicon, 9 Cu Interconnect Layers, 193nm Dry Patterning, and 100Devices Meeting. 2007; pp 247–250.

[8] Packan, P. et al. High performance 32nm logic technology featuring 2^{nd} generation high-k + metal gate transistors. 2009 IEEE International Electron Devices Meeting (IEDM). 2009; pp 1–4.

[9] Desai, S. B.; Madhvapathy, S. R.; Sachid, A. B.; Llinas, J. P.; Wang, Q.; Ahn, G. H.; Pitner, G.; Kim, M. J.; Bokor, J.; Hu, C.; Wong, H.-S. P.; Javey, A. MoS_2 transistors with 1-nanometer gate lengths. *Science* **2016**, *354*, 99–102.

[10] Britnell, L.; Gorbachev, R. V.; Jalil, R.; Belle, B. D.; Schedin, F.; Mishchenko, A.; Georgiou, T.; Katsnelson, M. I.; Eaves, L.; Morozov, S. V.; Peres, N. M. R.; Leist, J.; Geim, A. K.; Novoselov, K. S.; Ponomarenko, L. A. Field-Effect Tunneling Transistor Based on Vertical Graphene Heterostructures. *Science* **2012**, *335*, 947–950.

[11] Withers, F.; Del Pozo-Zamudio, O.; Mishchenko, A.; Rooney, A. P.; Gholinia, A.; Watanabe, K.; Taniguchi, T.; Haigh, S. J.; Geim, A. K.;

Tartakovskii, A. I.; Novoselov, K. S. Light-emitting diodes by band-structure engineering in van der Waals heterostructures. *Nature Materials* **2015**, *14*, 301–306.

[12] Ye, Y.; Ye, Z.; Gharghi, M.; Zhu, H.; Zhao, M.; Wang, Y.; Yin, X.; Zhang, X. Exciton-dominant electroluminescence from a diode of monolayer MoS_2. *Applied Physics Letters* **2014**, *104*, 193508.

[13] Levendorf, M. P.; Kim, C.-J.; Brown, L.; Huang, P. Y.; Havener, R. W.; Muller, D. A.; Park, J. Graphene and boron nitride lateral heterostructures for atomically thin circuitry. *Nature* **2012**, *488*, 627–632.

[14] Novoselov, K. S.; Jiang, D.; Schedin, F.; Booth, T. J.; Khotkevich, V. V.; Morozov, S. V.; Geim, A. K. Two-dimensional atomic crystals. *Proceedings of the National Academy of Sciences of the United States of America* **2005**, *102*, 10451–10453.

[15] Mayorov, A. S.; Gorbachev, R. V.; Morozov, S. V.; Britnell, L.; Jalil, R.; Ponomarenko, L. A.; Blake, P.; Novoselov, K. S.; Watanabe, K.; Taniguchi, T.; Geim, A. K. Micrometer-Scale Ballistic Transport in Encapsulated Graphene at Room Temperature. *Nano Letters* **2011**, *11*, 2396–2399.

[16] Balandin, A. A. Thermal properties of graphene and nanostructured carbon materials. *Nature Materials* **2011**, *10*, 569–581.

[17] Lee, C.; Wei, X.; Kysar, J. W.; Hone, J. Measurement of the Elastic Properties and Intrinsic Strength of Monolayer Graphene. *Science* **2008**, *321*, 385–388.

[18] Nair, R. R.; Blake, P.; Grigorenko, A. N.; Novoselov, K. S.; Booth, T. J.; Stauber, T.; Peres, N. M. R.; Geim, A. K. Fine Structure Constant Defines Visual Transparency of Graphene. *Science* **2008**, *320*, 1308–1308.

[19] Zhang, Y.; Tan, Y.-W.; Stormer, H. L.; Kim, P. Experimental observation of the quantum Hall effect and Berry's phase in graphene. *Nature* **2005**, *438*, 201–204.

[20] Novoselov, K. S.; Geim, A. K.; Morozov, S. V.; Jiang, D.; Katsnelson, M. I.; Grigorieva, I. V.; Dubonos, S. V.; Firsov, A. A. Two-dimensional gas of massless Dirac fermions in graphene. *Nature* **2005**, *438*, 197–200.

[21] Wallace, P. R. The Band Theory of Graphite. *Phys. Rev.* **1947**, *71*, 622–634.

[22] Han, W.; Kawakami, R. K.; Gmitra, M.; Fabian, J. Graphene spintronics. *Nature Nanotechnology* **2014**, *9*, 794–807.

[23] Schedin, F.; Geim, A. K.; Morozov, S. V.; Hill, E. W.; Blake, P.; Katsnelson, M. I.; Novoselov, K. S. Detection of individual gas molecules adsorbed on graphene. *Nature Materials* **2007**, *6*, 652–655.

[24] Kim, K. S.; Zhao, Y.; Jang, H.; Lee, S. Y.; Kim, J. M.; Kim, K. S.; Ahn, J.-H.; Kim, P.; Choi, J.-Y.; Hong, B. H. Large-scale pattern growth of graphene films for stretchable transparent electrodes. *Nature* **2009**, *457*, 706–710.

[25] Nair, R. R. et al. Fluorographene: A Two-Dimensional Counterpart of Teflon. *Small* **2010**, *6*, 2877–2884.

[26] Elias, D. C.; Nair, R. R.; Mohiuddin, T. M. G.; Morozov, S. V.; Blake, P.; Halsall, M. P.; Ferrari, A. C.; Boukhvalov, D. W.; Katsnelson, M. I.; Geim, A. K.; Novoselov, K. S. Control of Graphene's Properties by Reversible Hydrogenation: Evidence for Graphane. *Science* **2009**, *323*, 610–613.

[27] Park, S.; Ruoff, R. S. Chemical methods for the production of graphenes. *Nature Nanotechnology* **2009**, *4*, 217–224.

[28] Jin, Z.; Yao, J.; Kittrell, C.; Tour, J. M. Large-Scale Growth and Characterizations of Nitrogen-Doped Monolayer Graphene Sheets. *ACS Nano* **2011**, *5*, 4112–4117.

[29] Ci, L.; Song, L.; Jin, C.; Jariwala, D.; Wu, D.; Li, Y.; Srivastava, A.; Wang, Z. F.; Storr, K.; Balicas, L.; Liu, F.; Ajayan, P. M. Atomic layers of hybridized boron nitride and graphene domains. *Nature Materials* **2010**, *9*, 430–435.

[30] Watanabe, K.; Taniguchi, T.; Kanda, H. Direct-bandgap properties and evidence for ultraviolet lasing of hexagonal boron nitride single crystal. *Nature Materials* **2004**, *3*, 404–409.

[31] Paffett, M.; Simonson, R.; Papin, P.; Paine, R. Borazine adsorption and decomposition at Pt(111) and Ru(001) surfaces. *Surface Science* **1990**, *232*, 286–296.

[32] Kim, K. K.; Hsu, A.; Jia, X.; Kim, S. M.; Shi, Y.; Hofmann, M.; Nezich, D.; Rodriguez-Nieva, J. F.; Dresselhaus, M.; Palacios, T.; Kong, J. Synthesis of Monolayer Hexagonal Boron Nitride on Cu Foil Using Chemical Vapor Deposition. *Nano Letters* **2012**, *12*, 161–166.

[33] Dean, C. R.; Young, A. F.; Meric, I.; Lee, C.; Wang, L.; Sorgenfrei, S.; Watanabe, K.; Taniguchi, T.; Kim, P.; Shepard, K. L.; Hone, J. Boron

nitride substrates for high-quality graphene electronics. *Nature Nanotechnology* **2010**, *5*, 722–726.

[34] Geim, A. K.; Grigorieva, I. V. Van der Waals heterostructures. *Nature* **2013**, *499*, 419–425.

[35] Sun, Z.; Liao, T.; Dou, Y.; Hwang, S. M.; Park, M.-S.; Jiang, L.; Kim, J. H.; Dou, S. X. Generalized self-assembly of scalable two-dimensional transition metal oxide nanosheets. *Nature Communications* **2014**, *5*, 3813–3822.

[36] Dickinson, R. G.; Pauling, L. The crystal structure of molybdenite. *Journal of the American Chemical Society* **1923**, *45*, 1466–1471.

[37] Spalvins, T. A review of recent advances in solid film lubrication. *Journal of Vacuum Science & Technology A: Vacuum, Surfaces, and Films* **1987**, *5*, 212–219.

[38] Fleischauer, P. D.; Lince, J. R. A comparison of oxidation and oxygen substitution in MoS2 solid film lubricants. *Tribology International* **1999**, *32*, 627–636.

[39] Chianelli, R. R.; Siadati, M. H.; la Rosa, M. P. D.; Berhault, G.; Wilcoxon, J. P.; Jr., R. B.; Abrams, B. L. Catalytic Properties of Single Layers of Transition Metal Sulfide Catalytic Materials. *Catalysis Reviews* **2006**, *48*, 1–41.

[40] Mak, K. F.; Lee, C.; Hone, J.; Shan, J.; Heinz, T. F. Atomically Thin MoS_2: A New Direct-Gap Semiconductor. *Physical Review Letters* **2010**, *105*, 136805.

[41] Splendiani, A.; Sun, L.; Zhang, Y.; Li, T.; Kim, J.; Chim, C.-Y.; Galli, G.; Wang, F. Emerging Photoluminescence in Monolayer MoS_2. *Nano Letters* **2010**, *10*, 1271–1275.

[42] Wang, Q. H.; Kalantar-Zadeh, K.; Kis, A.; Coleman, J. N.; Strano, M. S. Electronics and optoelectronics of two-dimensional transition metal dichalcogenides. *Nature Nanotechnology* **2012**, *7*, 699–712.

[43] Fiori, G.; Bonaccorso, F.; Iannaccone, G.; Palacios, T.; Neumaier, D.; Seabaugh, A.; Banerjee, S. K.; Colombo, L. Electronics based on two-dimensional materials. *Nature Nanotechnology* **2014**, *9*, 768–779.

[44] Alidoust, N.; Bian, G.; Xu, S.-Y.; Sankar, R.; Neupane, M.; Liu, C.; Belopolski, I.; Qu, D.-X.; Denlinger, J. D.; Chou, F.-C.; Hasan, M. Z. Observation of monolayer valence band spin-orbit effect and induced quantum well states in MoX_2. *Nature Communications* **2014**, *5*, 4673–4682.

[45] Lopez-Sanchez, O.; Lembke, D.; Kayci, M.; Radenovic, A.; Kis, A. Ultrasensitive photodetectors based on monolayer MoS_2. *Nature Nanotechnology* **2013**, *8*, 497–501.

[46] Jena, D. Tunneling Transistors Based on Graphene and 2-D Crystals. *Proceedings of the IEEE* **2013**, *101*, 1585–1602.

[47] Li, M. O.; Esseni, D.; Snider, G.; Jena, D.; Xing, H. G. Single particle transport in two-dimensional heterojunction interlayer tunneling field effect transistor. *Journal of Applied Physics* **2014**, *115*, 074508.

[48] Conley, H. J.; Wang, B.; Ziegler, J. I.; Haglund, R. F.; Pantelides, S. T.; Bolotin, K. I. Bandgap Engineering of Strained Monolayer and Bilayer MoS_2. *Nano Letters* **2013**, *13*, 3626–3630.

[49] Radisavljevic, B.; Radenovic, A.; Brivio, J.; Giacometti, V.; Kis, A. Single-layer MoS_2 transistors. *Nature Nanotechnology* **2011**, *6*, 147–150.

[50] Krasnozhon, D.; Lembke, D.; Nyffeler, C.; Leblebici, Y.; Kis, A. MoS_2 Transistors Operating at Gigahertz Frequencies. *Nano Letters* **2014**, *14*, 5905–5911.

[51] Johnson, M.; Silsbee, R. H. Interfacial charge-spin coupling: Injection and detection of spin magnetization in metals. *Physical Review Letters* **1985**, *55*, 1790–1793.

[52] Nebel, C. E. Valleytronics: Electrons dance in diamond. *Nature Materials* **2013**, *12*, 690–691.

[53] Xiao, D.; Liu, G.-B.; Feng, W.; Xu, X.; Yao, W. Coupled Spin and Valley Physics in Monolayers of MoS_2 and Other Group-VI Dichalcogenides. *Physical Review Letters* **2012**, *108*, 196802.

[54] Xu, X.; Yao, W.; Xiao, D.; Heinz, T. F. Spin and pseudospins in layered transition metal dichalcogenides. *Nat Phys* **2014**, *10*, 343–350.

[55] Bishop, N. C.; Padmanabhan, M.; Vakili, K.; Shkolnikov, Y. P.; De Poortere, E. P.; Shayegan, M. Valley Polarization and Susceptibility of Composite Fermions around a Filling Factor $\nu = \frac{3}{2}$. *Physical Review Letters* **2007**, *98*, 266404.

[56] Gunawan, O.; Shkolnikov, Y. P.; Vakili, K.; Gokmen, T.; De Poortere, E. P.; Shayegan, M. Valley Susceptibility of an Interacting Two-Dimensional Electron System. *Physical Review Letters* **2006**, *97*, 186404.

[57] Zhu, Z.; Collaudin, A.; Fauque, B.; Kang, W.; Behnia, K. Field-induced polarization of Dirac valleys in bismuth. *Nature Physics* **2012**, *8*, 89–94.

[58] Rycerz, A.; Tworzydlo, J.; Beenakker, C. W. J. Valley filter and valley valve in graphene. *Nature Physics* **2007**, *3*, 172–175.

[59] Xiao, D.; Yao, W.; Niu, Q. Valley-Contrasting Physics in Graphene: Magnetic Moment and Topological Transport. *Physical Review Letters* **2007**, *99*, 236809.

[60] Dyakonov, M. Introduction to spin physics in semiconductors. *Physica E: Low-dimensional Systems and Nanostructures* **2006**, *35*, 246 – 250.

[61] Akhmerov, A. R.; Beenakker, C. W. J. Detection of Valley Polarization in Graphene by a Superconducting Contact. *Physical Review Letters* **2007**, *98*, 157003.

[62] Mak, K. F.; McGill, K. L.; Park, J.; McEuen, P. L. The valley Hall effect in MoS_2 transistors. *Science* **2014**, *344*, 1489–1492.

[63] Murakami, S.; Nagaosa, N.; Zhang, S.-C. Dissipationless Quantum Spin Current at Room Temperature. *Science* **2003**, *301*, 1348–1351.

[64] Sinova, J.; Culcer, D.; Niu, Q.; Sinitsyn, N. A.; Jungwirth, T.; MacDonald, A. H. Universal Intrinsic Spin Hall Effect. *Physical Review Letters* **2004**, *92*, 126603.

[65] Lee, J.; Mak, K. F.; Shan, J. Electrical control of the valley Hall effect in bilayer MoS_2 transistors. *Nature Nanotechnology* **2016**, *11*, 421–425.

[66] Bertolazzi, S.; Krasnozhon, D.; Kis, A. Nonvolatile Memory Cells Based on MoS_2/Graphene Heterostructures. *ACS Nano* **2013**, *7*, 3246–3252.

[67] Kolobov, A. V.; Tominaga, J. *Two-Dimensional Transition-Metal Dichalcogenides*; Springer International Publishing: Cham, 2016; pp 79–107.

[68] Coleman, J. N. et al. Two-Dimensional Nanosheets Produced by Liquid Exfoliation of Layered Materials. *Science* **2011**, *331*, 568–571.

[69] Zeng, Z.; Yin, Z.; Huang, X.; Li, H.; He, Q.; Lu, G.; Boey, F.; Zhang, H. Single-Layer Semiconducting Nanosheets: High-Yield Preparation and Device Fabrication. *Angewandte Chemie International Edition* **2011**, *50*, 11093–11097.

[70] Altavilla, C.; Sarno, M.; Ciambelli, P. A Novel Wet Chemistry Approach for the Synthesis of Hybrid 2D Free-Floating Single or Multilayer Nanosheets of MS_2@oleylamine (M=Mo, W). *Chemistry of Materials* **2011**, *23*, 3879–3885.

[71] Liu, K.-K.; Zhang, W.; Lee, Y.-H.; Lin, Y.-C.; Chang, M.-T.; Su, C.-Y.; Chang, C.-S.; Li, H.; Shi, Y.; Zhang, H.; Lai, C.-S.; Li, L.-J. Growth of Large-Area and Highly Crystalline MoS_2 Thin Layers on Insulating Substrates. *Nano Letters* **2012**, *12*, 1538–1544.

[72] Zhan, Y.; Liu, Z.; Najmaei, S.; Ajayan, P. M.; Lou, J. Large-Area Vapor-Phase Growth and Characterization of MoS_2 Atomic Layers on a SiO_2 Substrate. *Small* **2012**, *8*, 966–971.

[73] Lee, Y.-H.; Zhang, X.-Q.; Zhang, W.; Chang, M.-T.; Lin, C.-T.; Chang, K.-D.; Yu, Y.-C.; Wang, J. T.-W.; Chang, C.-S.; Li, L.-J.; Lin, T.-W. Synthesis of Large-Area MoS_2 Atomic Layers with Chemical Vapor Deposition. *Advanced Materials* **2012**, *24*, 2320–2325.

[74] Najmaei, S.; Liu, Z.; Zhou, W.; Zou, X.; Shi, G.; Lei, S.; Yakobson, B. I.; Idrobo, J.-C.; Ajayan, P. M.; Lou, J. Vapour phase growth and grain boundary structure of molybdenum disulphide atomic layers. *Nature Materials* **2013**, *12*, 754–759.

[75] Van der Zande, A. M.; Huang, P. Y.; Chenet, D. A.; Berkelbach, T. C.; You, Y.; Lee, G.-H.; Heinz, T. F.; Reichman, D. R.; Muller, D. A.; Hone, J. C. Grains and grain boundaries in highly crystalline monolayer molybdenum disulphide. *Nature Materials* **2013**, *12*, 554–561.

[76] Sørensen, S. G.; Füchtbauer, H. G.; Tuxen, A. K.; Walton, A. S.; Lauritsen, J. V. Structure and Electronic Properties of In Situ Synthesized Single-Layer MoS_2 on a Gold Surface. *ACS Nano* **2014**, *8*, 6788–6796.

Chapter 2

Experimental techniques and setup

2.1 Photoelectron Spectroscopy

Photoelectron Spectroscopy (XPS) is a very powerful non-destructive technique suitable for chemical analysis: it gives information about the elements present in the sample and their chemical state. These features make it useful in many fields, in particular in materials science. XPS relies on the photoelectric effect, first observed by Hertz in 1887[1], and for which formalization Albert Einstein in 1921 was awarded with the Nobel Prize in Physics. This section briefly describes the processes that underlie the photoelectric effect and some aspects required for the interpretation of the experimental results. As depicted in figure 2.1, when a photon with a certain energy interacts with a solid, it can remove an electron from an atomic core level or a molecular orbital, promoting it above the vacuum level. This process is usually described with a three step model[2]:

1. photoelectron excitation due to photon absorption;
2. transport of the photoelectron from the emitter atom towards the surface;
3. electron escape from the surface into the vacuum.

In order for this to happen, the photon energy must be higher than the sum of the initial electron binding energy and the work function of the solid. Within the one-electron approximation, the kinetic energy of the photoelectron in vacuum E_{kin}^{vac} can be written as

$$E_{kin}^{vac} = h\nu - E_b^F - \phi \tag{2.1}$$

where $h\nu$ is the photon energy, E_b^F is the binding energy referenced to the Fermi level (E_F) and ϕ is the work function of the material, defined as the

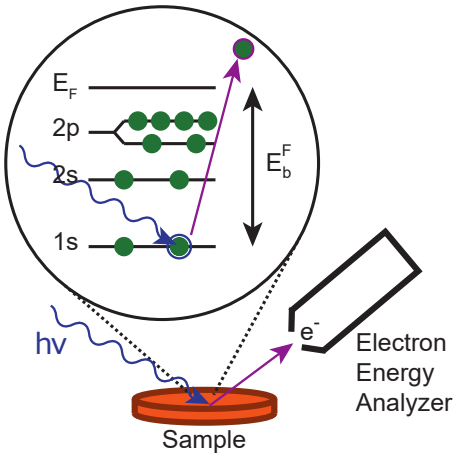

Figure 2.1: Schematic illustration of the photoemission process.

minimum energy required to remove an electron from the solid, that is the energy difference between the Fermi level and the electrostatic potential in the vacuum (nearby the surface)[3]. From this formula, it is possible to estimate E_b^F if the other quantities are known. E_b^F is characteristic for each element, hence XPS can be used for chemical identification. Another important property of photoemission spectroscopy is the surface sensitivity. This is related to the inelastic mean free path (IMFP) of the electrons, i.e. the average distance that an electron can travel before suffering energy losses due to inelastic scattering. Figure 2.2 reports the IMFP for different energies and materials, and it is worth noting that, while it strongly depends on the electron energy, it is almost independent from the material, leading to a general trend called universal curve. The IMFP at kinetic energy lower than 50 eV is dominated by collective excitations of atoms (phonons) and electrons (plasmons), while at kinetic energy higher than ∼100 eV one electron excitations dominate. These two trends lead to the formation of a minimum between 50 and 100 eV kinetic energy. In general, between 20 eV and 500 eV, the IMFP is less than 10 Å, which means that the photo-electrons observed without energy loss come from the first few layers of the solid and hence this guarantees the surface sensitivity of the technique. XPS can be used for quantitative analysis but, in order to do this, we must know the cross-section σ, defined as the probability per unit time for a system to be promoted from its initial electronic state Ψ_i to a final state Ψ_f thanks to the absorption of a photon with energy $h\nu{=}h\omega/2\pi$, divided by the photon flux. The cross-section σ_{fi} can be written as

$$\sigma_{fi} = \frac{4\pi^2 e^2}{3\hbar c}\omega \left|\langle \Psi_f | \hat{\mathbf{r}} | \Psi_i \rangle\right|^2 \tag{2.2}$$

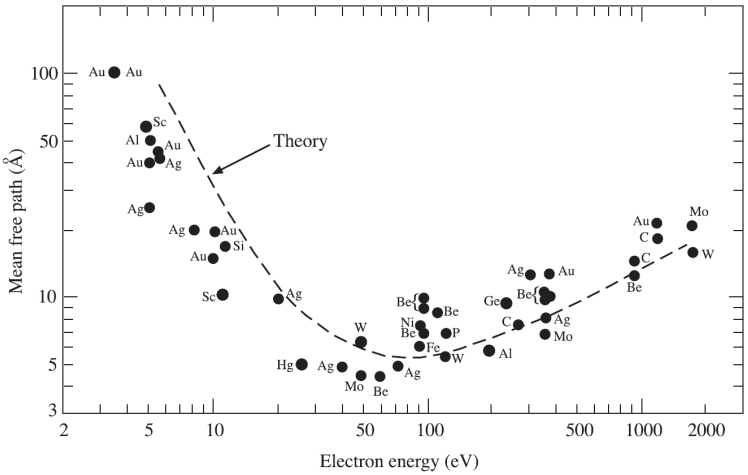

Figure 2.2: Electron IMFP as a function of the electron kinetic energy for different elements leading to the so-called universal curve.

where $\hat{\mathbf{r}}$ is the position operator. The photoemission cross-section depends on the atomic level and on the atomic number of the element but it is independent from the chemical environment of the atoms[4]. Figure 2.3 shows, as an example, the variation of the photoemission cross-section as a function of the photon energy for some of the core levels analyzed in this thesis work, specifically Au 4f, Mo 3d and S 2p core levels. This figure underlines the convenience offered by a synchrotron facility, namely the possibility to choose a suitable photon energy. Indeed, by tuning the energy, it is possible to maximize, or minimize, the sensitivity to a certain core level, enhancing or diminishing the corresponding photoelectron cross-section.

Now, we take a step back and focus on the physical meaning of the binding energy term obtained by means of equation 2.1. Let us first consider the approximated model used so far for the determination of equation 2.1, that is the single particle approximation. In this case, the photoemission process removes an electron from the atom leaving the other electrons unchanged. Therefore, by considering an atomic system with N electrons, and by assuming that the system after the photoemission process remains unperturbed in the same state as before the event (frozen orbital approximation), Koopmans in 1934[5], showed that

$$E_b^{vac}(k) = E^f(N-1,k) - E^i(N) = -\epsilon_k, \tag{2.3}$$

where ϵ_k is the Hartree-Fock orbital energy. In other words, equation 2.3 assumes that the measured binding energy corresponds to the ground-state orbital energy of the electron. However, due to many body effects, like the relaxation of the system after the photoemission process and the electron correlations, equation 2.3 can result in a rough approximation for the de-

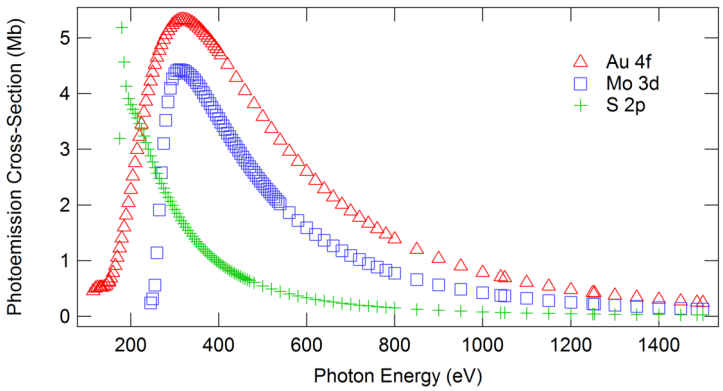

Figure 2.3: Photoemission cross-section for Au $4f$, Mo $3d$ and S $2p$ core levels as a function of the energy of the incident photons.

termination of the binding energy. Therefore, a more correct description of $E_b(k)$ is given by

$$E_b^{vac}(k) = -\epsilon_k + \delta E_{corr} - \delta E_{rel}^{intra} - \delta E_{rel}^{inter} \tag{2.4}$$

that takes into account the *intra-atomic* relaxation of the (N-1)-electrons δE_{rel}^{intra}, and the electron correlation δE_{corr}, which is excluded from the Hartree-Fock approximation. Moreover, when we consider an atom placed in a solid, the *interatomic relaxation* δE_{rel}^{inter} is added. In addition, the picture is even more complicated by considering other final state effects, such as shake-up and shake-off transitions that, together with the generation of plasmons which are a collective excitation of electrons in the valence band, generate satellite peaks with characteristic features at different BE with respect to the main peak.

Figure 2.4 schematically explains how the density of states inside the solid can be detected. Indeed, in a photoemission experiment, the photoelectron kinetic energy is measured and the binding energy is calculated by means of equation 2.1, where the Fermi level is the commonly used binding energy of reference for metals. However, the energy of the photoelectrons entering in the analyzer is changed by the difference between the work function of the analyzer $\phi_{analyzer}$ and that of the sample ϕ. This is true if the sample and the analyzer are grounded together and therefore they have a common Fermi level. In this way the equation 2.1 can be re-written as

$$E_b^F = h\nu - E_{kin}^{meas} - \phi_{analyzer}, \tag{2.5}$$

where the work function of the electron energy analyzer $\phi_{analyzer}$ is a known value.

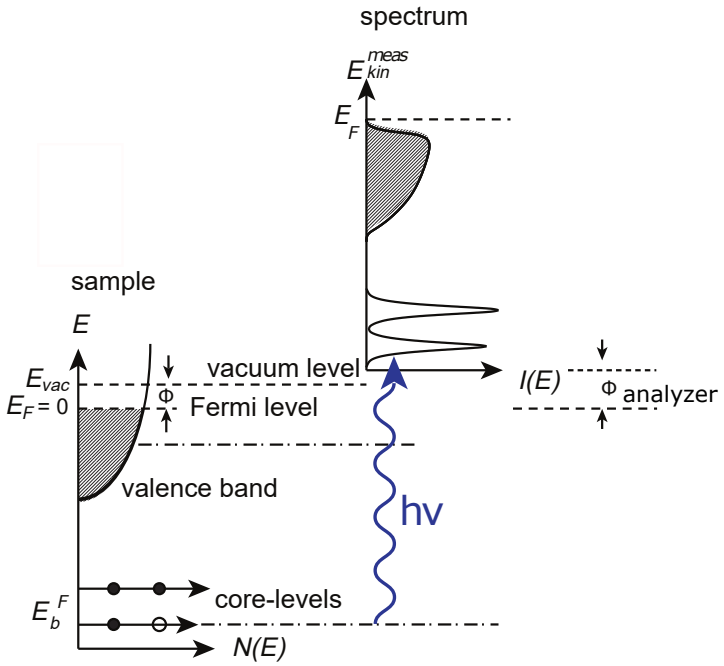

Figure 2.4: Energy level diagram in a XPS experiment.

2.1.1 Spectral features

The first spectral contribution described in this section is the *chemical shift*. XPS does not give information only about the chemical elements present in the sample, but also reflects the different structural and chemical environments. The formation of a chemical bond, in which delocalized valence electrons are directly involved, is perceived also by the localized core electrons, which binding energy changes. The chemical shift is the value that contains this information and it is defined as the binding energy difference of a given core level in two atoms of the same element with different chemical surroundings. As an example, figure 2.5 (a) reports the Mo 3d core level for metallic molybdenum deposited on Ag(111), colored in blue, and molybdenum belonging to single layer MoS_2, in pink. It is clear from the graph that the spin-orbit doublets are centered at different binding energies, reflecting the fact that the molybdenum atoms are in a different environment. A particular chemical shift is the *Surface Core Level Shift* (SCLS), which is the binding energy difference between the atoms at the surface with respect to those in the bulk of a solid sample. The presence of the SCLS is extremely useful when performing studies of the reactivity of a surface, as it permits a direct access to what is happening to the sample surface atoms, for example during a chemical reaction. The SCLS, often observed in transition metal surfaces, has a smaller extent compared to other core level shifts (500-600

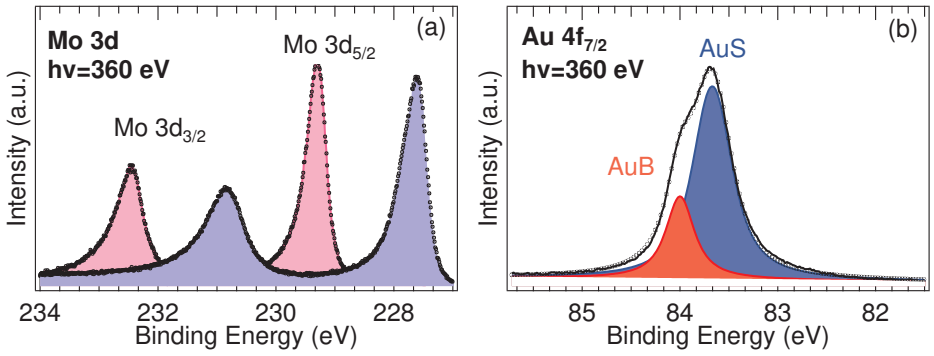

Figure 2.5: (a) spin-orbit splitted components of Mo 3d core level for metallic Mo (blue) and for MoS_2 (pink); (b) Au $4f_{7/2}$ core level spectrum.

meV and below), therefore it must be studied by means of high resolution photoelectron spectroscopy.

Another relevant spectral feature of the XPS spectra is the spin-orbit splitting which is caused by the interaction between the spin of the electron (s=1/2) and its angular momentum l. This leads to a splitting of the two degenerate states having a total angular momentum quantum number $j = l \pm 1/2$. Figure 2.5(a) shows the $3d_{3/2}$ and $3d_{5/2}$ spin-orbit split components of the Mo 3d photoemission peak. The intensities of the two spin-orbit split components are related by the equation $(2j^+ + 1)/(2j^- + 1)$ where $j^{\pm} = l \pm s$ and $s = 1/2$. In the case of a d-level such as the Mo 3d reported in figure 2.5 (a), l=2 and the ratio between the peaks is 3/2.

2.1.2 Core level photoemission line shape

In order to perform quantitative chemical analysis with XPS, a theoretical model that describes the photoemission spectrum is needed to fit the data. The Doniach-Šunjić semi-empirical formalism[6] convoluted with a Gaussian distribution is used for the fitting of many core levels. In this model, there are three contributions: the Lorentzian contribution, arising from the finite core-hole lifetime related to the decay-processes via Auger and X-ray emission; the asymmetry parameter, describing the contribution of electron-hole pairs excitation near the Fermi level; the Gaussian function, which accounts for the experimental energy resolution and the vibrational and inhomogeneous broadening. Let us now analyze these different contributions. Considering the Heisenberg's uncertainty principle $\Delta E \Delta t \geq \hbar/2$, a finite core hole lifetime implies an uncertainty in the energy. By assuming an exponential decay probability in the time domain for the core hole, the resulting spectral function, obtained by means of the Fourier transform, assumes the form of

a Lorentzian distribution

$$I_{Lor}(E_{kin}) = \frac{I_0}{\pi} \frac{\Gamma_L/2}{(E_{kin} - E_0)^2 + (\Gamma_L/2)^2}, \tag{2.6}$$

where Γ_L is the full width at half maximum (FWHM) and E_0 is the position of the peak in the spectrum for the maximum intensity I_0.

The experimental energy resolution derives from the fact that the monochromator selects a finite photon band width and the electron energy analyzer has a finite resolution. The inhomogeneous broadening derives from the superposition of lines with different chemical shifts that cannot be resolved. Finally, the vibrational broadening is due to the excitation of low energy vibrational modes. These three effects are represented by the Gaussian distribution

$$I_{Gaus} = I_0 \exp\left(-\frac{(E_{kin} - E_0)^2}{2\Gamma_G^2}\right), \tag{2.7}$$

where Γ_G is the FWHM. In order to take into account the inelastic tail of the photoemission peaks due to excitation of electron-hole pairs at the Fermi level, the Doniach-Šunjić function presents an asymmetry parameter α

$$I_{DS}(E_{kin}) = I_0 \frac{\Gamma_E(1-\alpha)}{[(E_{kin} - E_0)^2 + (\Gamma/2)^2]^{(1-\alpha)/2}} \zeta(E_{kin}), \tag{2.8}$$

where Γ_E is the gamma function

$$\Gamma_E(x) = \int_0^\infty t^{x-1} e^{-t} dt. \tag{2.9}$$

and

$$\zeta(E_{kin}) = \cos\left[\frac{\pi\alpha}{2} + (1-\alpha)\arctan\left(\frac{E_{kin} - E_0}{\Gamma/2}\right)\right]. \tag{2.10}$$

This model was used to analyze the XPS spectra presented in this thesis and a linear background was included in the fits. Finally, all the binding energies were referenced to the Fermi level, which was measured together with the corresponding core level spectra.

2.2 Photoelectron Diffraction

When a photoelectron leaves the emitting atom, it can reach the analyzer following a direct path or it can be scattered by the atoms surrounding the emitter. The interference of the direct primary wave and the scattered waves produces diffraction patterns, that are modulations of the photoemission intensity that depend on the emission direction and the electron kinetic energy. This mechanism, which is schematically shown in figure 2.6, is at the base of the X-ray Photoelectron Diffraction (XPD) technique. The XPD

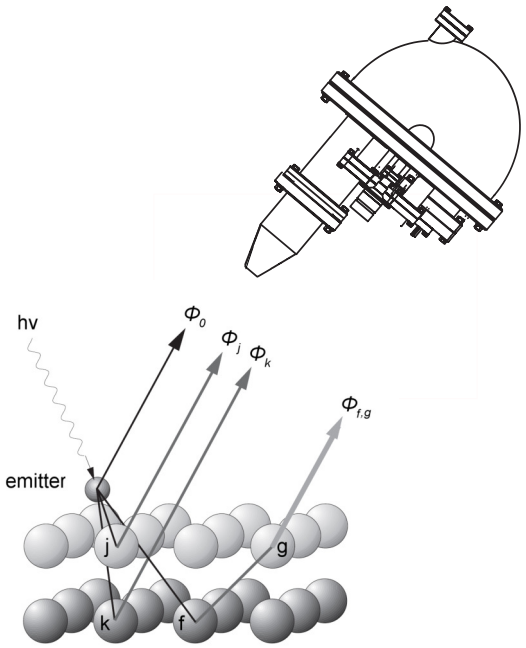

Figure 2.6: Sketch of the photoelectron diffraction process. ϕ_0 is the direct wave and ϕ_l are the scattered waves.

technique is an effective tool to study short range order, bond directions, bond distances and site symmetries with chemical specificity by selecting a given emitter through its core level peak.

The intensity I($\mathbf{k}$) of the diffraction pattern along a given $\mathbf{k}$ direction can be determined by means of the Fermi Golden Rule, where the calculation of the squared matrix element is based on the dipole approximation. This is based on the assumption that the wavelength of the incoming photon is much longer than the atomic distance, thus ignoring the spatial dependence of the electromagnetic wave ($e^{i\mathbf{kr}} \simeq 1$). This assumption is valid for photon energies lower than approximately 1 KeV and leads to a squared transition matrix element that depends on the dipole operator ($\boldsymbol{\epsilon} \cdot \mathbf{r}$). Therefore, the intensity is given by:

$$I(\mathbf{k}) \propto \sum_{emitt} | < \psi_i(\mathbf{r}, \mathbf{k}) | \boldsymbol{\epsilon} \cdot \mathbf{r} | \psi_f(\mathbf{r}, \mathbf{k}) > |^2 \tag{2.11}$$

where $\mathbf{k}$=(k, θ, ϕ), $\psi_i(\mathbf{r}, \mathbf{k})$ is the initial-state wave-function, $\boldsymbol{\epsilon}$ is the polarization vector of the incident photons, $\mathbf{r}$ is the vector connecting neighboring atoms, and $\psi_f(\mathbf{r}, \mathbf{k})$ is the final-state wave-function resulting from the scattering process. Within the single-scattering approximation, $\psi_f(\mathbf{r}, \mathbf{k})$ can be written as

$$\psi_f(\mathbf{r},\mathbf{k}) = \phi_0(\mathbf{r},\mathbf{k}) + \sum_j \phi_j(\mathbf{r},\mathbf{r}_j \rightarrow \mathbf{k}), \tag{2.12}$$

where ϕ_0 is the direct wave and ϕ_j is the generic scattered wave resulting from the scattering of ϕ_0 with a scatterer at position r_j, and emerging in the direction $\mathbf{k}$.

Since the distance between the emitter and the detector can be regarded to be infinite along $\mathbf{k}$, both the direct and scattered waves can be written as spherical waves

$$\phi_0(\mathbf{r},\mathbf{k}) \propto \frac{e^{i\mathbf{kr}}}{|\mathbf{r}|} \tag{2.13}$$

$$\phi_j(\mathbf{r}_j,\mathbf{k}_j) = \phi_0(\mathbf{r},\mathbf{k})\frac{f_j(\mathbf{k},\theta_j)e^{i\mathbf{k}|\mathbf{r}-\mathbf{r}_j|}}{|\mathbf{r}-\mathbf{r}_j|}, \tag{2.14}$$

where θ_j is the angle between $\mathbf{r}_j$ and $\mathbf{k}$ and $f_j(\mathbf{k},\theta_j)$ is the scattering factor. Usually the expression for $f_j(\mathbf{k},\theta_j)$ is calculated by assuming that the incoming wavefunction $\phi_0(\mathbf{r},\mathbf{k})$ is a plane wave and can be written as

$$f_j(\mathbf{k},\theta_j) = |f_j(\mathbf{k},\theta_j)|e^{i\chi_j(\theta_j)}, \tag{2.15}$$

where χ_j is a phase shift associated with the scattering event. By plotting the amplitude of the scattering factor as a function of the scattering angle, as shown in figure 2.7 for copper[2], interesting features emerge. The scattering factor is strongly anisotropic and has its maximum at small scattering angles. This is the so-called *forward* scattering that shows a strong enhancement of the measured intensity for scattering atoms that sit between the emitter atom and the detector, that is at θ_j=0°. Moreover, the intensity of the scattered wave is increased by increasing the kinetic energy and becomes essentially dominant at large kinetic energies. The analysis performed at large kinetic energy allows the direct interpretation of the data, that is, to determine the interatomic bond directions of the atoms close to the surface. At kinetic energies lower than approximately 100 eV, there is a large modulation at all angle, whereas at intermediate energies, ranging between ∼100 eV and ∼1000 eV, only forward and backward scattering are present. The latter is associated with photoelectrons scattered by atoms placed at an opposite orientation with respect to the ones responsible of forward scattering, that is at θ_j=180°.

For an accurate description of the photoelectron diffraction process, other effects must be taken into account. Firstly, multiple scattering calculations must be added. Moreover, one must consider the inelastic scattering of the electrons that reduces their propagation in the solid and, finally, the thermal vibrations. In order to extract detailed information about the structure around the emitting atom, the experimental diffraction patterns must be

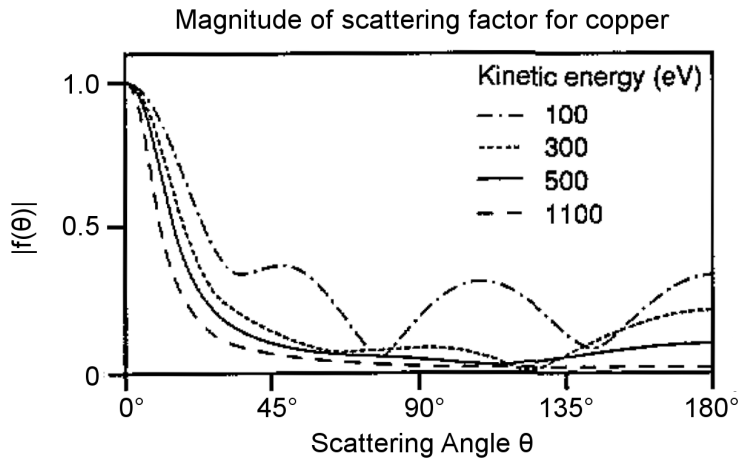

Figure 2.7: Magnitude of the scattering factor for copper as a function of the scattering angle and for different electron kinetic energies. Adapted from reference[2]

.

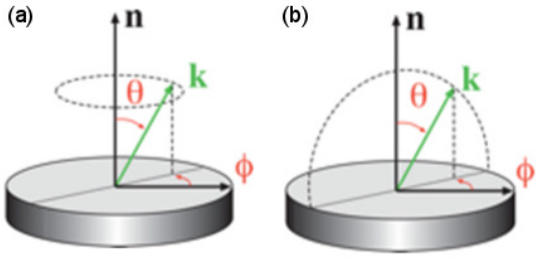

Figure 2.8: Schematic diagram of (a) an azimuthal and (b) a polar scan.

compared with theoretical calculations. Several computational approaches were developed to take into account these effects[7]. All the theoretical simulations that are present in this thesis have been performed using the Electron Diffraction in Atomic Clusters (EDAC) package[8]. The working principle of this code is based on the implementation of an atomic cluster and the use of multiple scattering theory to model the XPD pattern at a specific electron kinetic energy.[1]

The photoemission spectra were measured for different polar (θ) and azimuthal (ϕ) angles, as shown in figure 2.8, and for each of them, the peak fit analysis was performed and the intensity I(θ, ϕ) of each component resulting from the fit, i.e. the area under the photoemission line, was extracted. Each XPD pattern was measured over a wide azimuthal sector 160°, from normal

[1]For further details on the EDAC code the reader is referred to the reference manual which is available online at http://garciadeabajos-group.icfo.es/widgets/edac/manual/edac.html

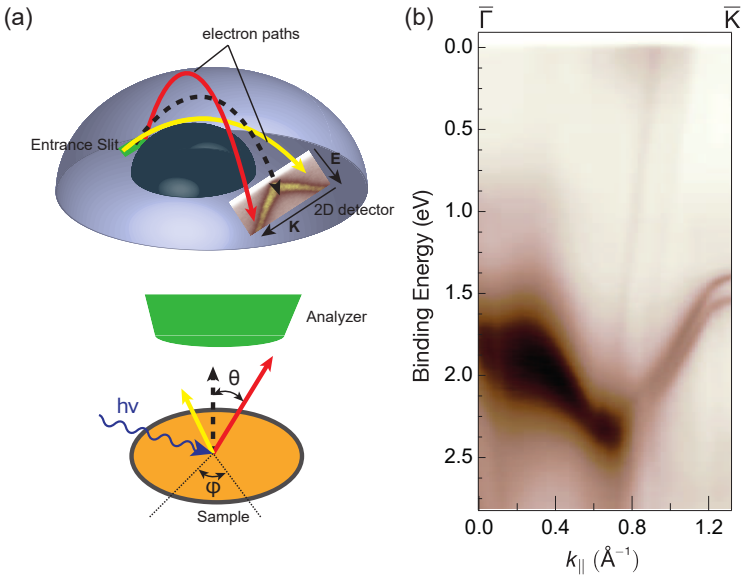

Figure 2.9: (a) Sketch of the trajectory of the electrons as they move from the entrance slit to the two dimensional detector. θ is the polar angle, φ is the azimuthal angle. (b) Angle-resolved photoemission intensity along the Γ-K direction of single layer MoS_2 Brillouin zone.

(θ=0°) to grazing emission (θ=70°). All the XPD data were displayed as a stereographic projection of the modulation function χ, which was obtained from the peak intensity for each polar emission angle as

$$\chi(\theta,\phi) = \frac{I(\theta,\phi) - I_0(\theta)}{I_0(\theta)} \tag{2.16}$$

where $I_0(\theta)$ is the average intensity for each azimuthal scan. The experimental XPD results were then compared with the simulations and the agreement between the two was quantified by the Reliability Factor (R)[9],

$$R = \frac{\sum_i (\chi_{\mathrm{exp},i} - \chi_{\mathrm{sim},i})^2}{\sum_i (\chi^2_{\mathrm{exp},i} + \chi^2_{\mathrm{sim},i})} \tag{2.17}$$

where $\chi_{\mathrm{sim},i}$ and $\chi_{\mathrm{exp},i}$ are the calculated and the experimental modulation functions for each data point i.

2.3 Angle-Resolved Photoemission Spectroscopy

Angle-resolved photoemission spectroscopy (ARPES) is widely used to investigate the valence band, and in general electronic states below the Fermi level, of crystalline solids, returning a map of the occupied electronic band structure

of the solid and therefore obtaining information about its electronic properties. This technique provides also a deep insight into many-body interactions in ordered solids and it is the main tool to study phenomena such as strongly-correlated electronic systems[10] and electron-phonon coupling[11, 12]. In ARPES, photoelectrons are emitted from the solid upon absorption of an incoming photon as much as it happens for XPS. Photoemission spectra are collected at different emission angles in order to extract information about electron binding energy and initial crystalline momentum, determining the electron energy dispersion relation $E(\mathbf{k})$ and therefore mapping the band shape, as briefly described below.

The relation between the energy of electrons and their momentum defines the electronic band structure, and can be obtained by solving the Schrödinger equation with a proper Hamiltonian. By neglecting many-body interactions between electrons, the behavior of electrons inside a crystal can be described by the one-electron Hamiltonian. Before solving the Schrödinger equation for an electron inside a crystal, we assume the simplest case of free electrons, where we can write the steady-states Schrödinger equation as

$$[-\frac{\hbar^2}{2m_e}\nabla_r^2]\psi(\mathbf{r}) = E\psi(\mathbf{r}). \tag{2.18}$$

The eigenfunctions $\psi_{\mathbf{k}}(\mathbf{r})$ and the eigenvalues $E(\mathbf{k})$ solution of the equation 2.18 are given by

$$\psi_{\mathbf{k}}(\mathbf{r}) = A\exp(i\mathbf{k}\cdot\mathbf{r}) + B\exp(-i\mathbf{k}\cdot\mathbf{r}) \tag{2.19a}$$

$$E(\mathbf{k}) = \hbar^2|\mathbf{k}|^2/2m_e \tag{2.19b}$$

where m_e is the electron rest mass and A and B are complex amplitudes. The energy dispersion relation $E(\mathbf{k})$ in this case is parabolic and it is shown in figure 2.10 (a) along a given direction in the k-space.

Let us now consider the case of an electron in a crystal for which the Hamiltonian reported in equation 2.18 must also include a potential term given by the atomic potentials of the ordered crystal lattice. This periodicity implies that the steady state solutions of the Schrödinger equation are Bloch waves $\psi_{\mathbf{k}}(\mathbf{r}) = u_{\mathbf{k}}(\mathbf{r})\exp(i\mathbf{k}\cdot\mathbf{r})$ given by the product of a plane wave and a periodic Bloch function $u_{\mathbf{k}}(\mathbf{r})$ that represents the rapid oscillations on the scale of the crystal lattice. The properties of this new $\psi_k(\mathbf{r})$ and of the corresponding eigenvalues are:

$$\psi_{\mathbf{k}}(\mathbf{r}) = \psi_{(\mathbf{k}+\mathbf{G})}(\mathbf{r}) \tag{2.20a}$$

$$E_{\mathbf{k}} = E_{\mathbf{k}+\mathbf{G}} \tag{2.20b}$$

where $\mathbf{G}$ is the reciprocal lattice vector. Consistently with a second order parabolic approximation, the dispersion relation in the proximity of a valley

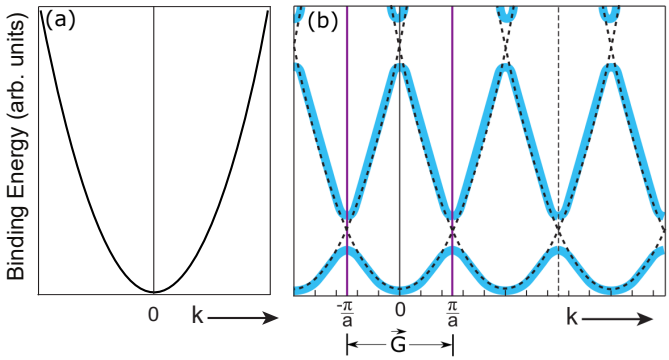

Figure 2.10: (a) Energy dispersion relation for the free-electron case. (b) Energy dispersion relation for a nearly free electron with a vanishing (dashed line) or non-vanishing (solid line) periodic potential, where the periodicity is given by G=2π/a (where a is the lattice constant).

minima/maxima (defined as minima of the conduction band or maxima of the valence band) can be written as

$$E(\mathbf{k}) = \hbar^2|\mathbf{k}|^2/2m^*. \tag{2.21}$$

Equation 2.21 is similar to that of a free electron but with m* being the effective mass experienced by electrons inside the crystal in a given valley. By means of the property reported in equation 2.20b, the energy dispersion relation in the case of a vanishing crystal potential is shown in figure 2.10 (b) (dashed line), it has the same parabolic behavior as for the case of a free electron but it is periodic of period G in the reciprocal space. In the case of a non vanishing periodic potential, the expression for the energy becomes more complicated but it is worth recalling that band gaps appear at the Brillouin zone boundaries as shown in figure 2.10 (b) (solid line).

Before proceeding to describe how ARPES measurements are performed, we recall that the aim is to derive information about the electronic structure inside the solid through photoemitted electrons. Therefore, it is of utmost importance to determine the quantities that are conserved during the photoemission process. As discussed in the previous sections, at the basis of the XPS technique there is the conservation of energy as reported by equation 2.5. Conversely, in the case of ARPES measurements one also aims at the determination of the crystal momentum through photoemitted electrons. Therefore, on the basis of the three step model for the photoemission process, we will briefly discuss about this latter aspect.

In the photoemission process, electrons gain kinetic energy but the momentum is left basically unchanged, given the small momentum amount provided by photons in the UV range ($|\mathbf{k}| = E_{ph}/\hbar c$), with respect to electron momentum itself. In the second step, electrons travel through the bulk to reach the surface. In this path they can undergo inelastic as well as elastic

scattering. In the former case, we already know from the XPS and XPD techniques that such electrons do not strongly affect the measurement because they can always be decoupled from the elastic ones. On the other hand, electrons that are subjected to elastic scattering preserve their kinetic energy but they also undergo a change in their momentum. This can in principle strongly affect the band structure determination, however, since elastically scattered electrons do not have a particular preference on the emission angle, their final k-vector will have an almost random distribution contributing to some background in the measured photoemission intensity. The last step involves the escape of the electron from the surface and requires electrons with energies larger that the work function ϕ of the material. It is evident that the translation symmetry along the surface normal direction is broken, therefore the transverse k-vector $\mathbf{k}_\perp$ will not be conserved whereas the in-plane k-vector $\mathbf{k}_\parallel$ will remain the same as before. Since the aim of this thesis is to investigate 2D materials, the only meaningful dispersion relation is that in the in-plane direction, therefore the non-conservation of $\mathbf{k}_\perp$ it is not an issue.

We reiterate that the determination of the crystal band structure requires the knowledge of the electronic momentum $\mathbf{k}$ and energy of the electrons in the crystal, and in ARPES measurements this is done by means of the photoemitted electrons.

The determination of the parallel crystalline momentum $\mathbf{k}_\parallel$ can be obtained by projecting the $\mathbf{k}$ vector of the photoelectron onto the surface plane using the expression for electrons in vacuum given by equation 2.19b resulting in

$$k_\parallel = \frac{1}{\hbar}\sqrt{2m_e E_{kin}}\sin\theta \tag{2.22}$$

where θ is the polar angle defined in figure 2.9 and E_{kin} is the measured kinetic energy of the photoelectrons.

As far as the experimental techniques are concerned, one collects different photoemission spectra by varying the photon energy, usually chosen within the UV range to maximize the cross section in the valence band and to achieve higher momentum resolution, and the azimuthal and polar emission angles. Electrons are collected by a hemispherical analyzer, analogous to the one used for XPS (that will be discussed in Section 2.7), where it is performed a scan at a fixed azimuthal angle φ (that determines the scanning direction in the Brillouin zone) and then it is varied the polar angle θ to scan the band structure along a given direction. Such a measurement is usually done with a with a two-dimensional detector capable of detecting at once a range of emission polar angles and kinetic energies, as sketched in figure 2.9 (a).

The results are displayed in a plot of binding energy versus the parallel component of the wave vector ($K_\parallel$) along a given direction, as shown in figure 2.9 (b). The knowledge of the band structure allows one to study energy

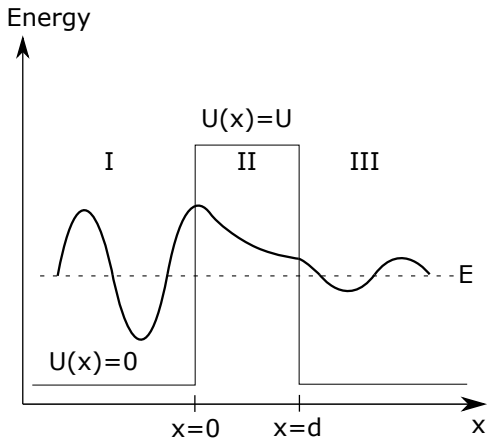

Figure 2.11: Tunnel effect in the presence of a stationary potential barrier.

bandgaps, life-times of carriers[12], as well as other aspects and from the curvature of the $E(\mathbf{k})$ it is possible to calculate the effective mass m* of the electrons inside the crystal by means of equation 2.21 by a double derivative of the energy over $\mathbf{k}$. Since $\mathbf{k}$ is a vector in a 3D space, this would lead to a 3x3 tensor of effective masses. For simplicity we report the expression for the 1D case given by

$$\frac{1}{m^*} = \frac{1}{\hbar^2}\frac{\partial^2 E_k}{\partial k^2}. \tag{2.23}$$

The effective mass of a carrier (electron or holes) is an important ingredient for the electron device modelling. In fact, together with other ingredients it allows one to determine the density of states in 3D but also quantized 2D and 1D systems, the velocity of carriers in equilibrium and out-of-equilibrium conditions, the splitting of the energy levels in quantized systems, the tunneling probability, as well as many other properties.

2.4 Scanning Tunneling Microscopy

Scanning tunneling microscopy is another technique to study surfaces. It was invented in the 80' by Gerd Binnig and Heinrich Rohrer at IBM in Zurich[13, 14] and they were awarded in 1986 with the Nobel prize in Physics.

This instrument is based on the quantum mechanical tunneling effect between a sharp metallic tip and a conductive sample and allows to resolve surfaces at atomic level as well as to obtain other useful information related to the electronic structure (i.e. the local density of states, band gaps). To describe the tunneling effect that is at the basis of the STM we report the simple case of a 1D plane wave $\Psi(x) = Ae^{-ikx}$ with energy E injected against a potential barrier as shown in figure 2.11. $U(x)$ is a stationary potential and the solution of the Schrodinger equation for regions I and III, and for

arbitrary energies, are the well known plane waves as seen in the previous section for free electrons

$$\Psi_I(x) = Ae^{-ikx} + Be^{+ikx} \qquad (2.24)$$
$$\Psi_{III}(x) = Ce^{-ikx}$$

where A and B are complex constants and where $k = (\sqrt{2mE})/\hbar$, assuming for the sake of simplicity that m_I=m_{II}=m_{III}=m. In region II, for energies E lower than the potential barrier U, the wavefunction becomes an evanescent wave, exponentially decaying without oscillations, of the type

$$\Psi_{II}(x) = De^{+\alpha x} + Ee^{-\alpha x} \qquad (2.25)$$

where $k = i(\sqrt{2m(U-E)})/\hbar = i\alpha$, with U being the potential barrier height in region II. By imposing the proper continuity conditions between the three different regions, the final solution is shown in figure 2.11. There are remarkable aspects in the solution of this problem: the most important one is that in the classical case the transition from domain I to III is forbidden for particles with energy $E < U$, whereas in the quantum case there is a finite probability that the injected wave $\Psi(x) = Ae^{-ikx}$ from domain I crosses domain II with a transmission coefficient $T \propto e^{-2\alpha d}$. This means that the transmission coefficient exponentially depends on the barrier width d and on the potential barrier height through the α term defined above. Moreover, the barrier only affects the tunneling transmission coefficient, and not the energy of the tunneling particles. Finally, the tunneling effect leads to a probability current density, proportional to the transmission coefficient T, that is the quantity directly measured by the STM. This leads to a very large sensitivity of the STM towards the vertical resolution, since the measured current exponentially depends on the distance d that, in the simple model described above, is representative of the distance between the sample and the tip.

The STM instrument consists of a probe tip, usually W or a Pt-Ir alloy, attached to three mutually perpendicular piezoelectric trasducers that control the movements in the three dimensions in the sub-Angstrom scale. The controlled positioning of the tip in the sub-Angstrom regime allows the measurement of a tunneling current usually in the range of nA. It is moreover necessary to isolate the instrument from the external vibrations to achieve atomic resolution; thus, the STM is usually suspended on a set of springs on a dumping system. STM measurements can be run in several conditions, such as ultra high vacuum, air and liquid. The temperature range in which STM measurements can be carried out range from liquid helium temperature to a few hundred degrees centigrade. In order to minimize the thermal drift and increase the image resolution, the instrument and the sample are usually stabilized at low temperature. The STM can operate in two different

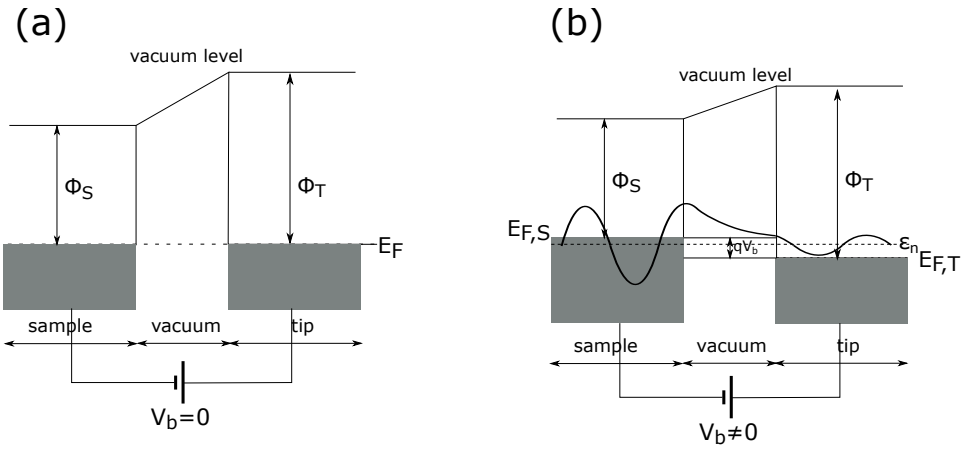

Figure 2.12: Band structure representative of an STM tip in close contact with a metal sample. ϕ_S and ϕ_T are the sample and tip workfunctions, respectively. Grey regions represent filled states. (a) Zero bias voltage, (b) bias voltage larger than zero induces a shift of the sample and tip Fermi levels, thus allowing for a tunneling current.

modes: constant current and constant height mode. In the constant current mode, the tunneling current is kept constant thanks to a feedback controller that adjusts the height of the tip while rastering the surface whereas in the constant heigh mode the heigh is kept constant and it is recorded the tunneling current. By far, the most common is the constant current mode, because it avoids tip crashes against surface asperities while scanning and allows to easily extract topographical information about the surface. In fact, at a first approximation, the constant current mode allows to map the sample topography giving information about the atoms distribution on the surface. However, as discussed below, the tunneling current is proportional to the electronic density of states at the surface. Therefore STM images are given by a convolution of topography effects and electronics effects realted to the density of states.

Figure 2.12 (a) shows the case of a metal sample and metal tip at thermodynamic equilibrium (with zero bias voltage V_b). In this case, thanks to the aligned Fermi levels E_F=$E_{F,S}$=$E_{F,T}$ there is no net current flux due to tunneling effect because the states below the common Fermi level are filled. Therefore, a bias voltage V_b is necessary to probe the sample empty or filled states (depending on the sign of V_b). This is shown in figure 2.12 (b), where a positive V_b is applied to probe the sample filled states in the energy window between $E_{F,S}$ and $E_{F,S} - eV_b$. The tunneling current for a given mode at energy ε_n is proportional to the tunneling coefficient and can be written as

$$I_n \propto |\Psi_n(0)|^2 \, e^{-2\alpha d} = |\Psi_n(0)|^2 \, e^{-2\frac{\sqrt{2mU}}{\hbar} d} \tag{2.26}$$

where d is the distance between the tip and the sample, and where the

potential term U, for small V_b values compared with Φ_S and Φ_T can be approximated by the average work function $U = (\Phi_S + \Phi_T)/2$. Under the assumption of T=0K, the total average current is given by the summation of I_n over the possible modes between $E_{F,T} = E_{F,S} - eV_b$ and $E_{F,S}$

$$I \propto \sum_{\varepsilon_n = E_{F,S} - eV_b}^{E_{F,S}} |\Psi_n(0)|^2 \, e^{-2\frac{\sqrt{2mU}}{\hbar}d}. \tag{2.27}$$

If the bias voltage is small enough such that the density of states is almost constant in the summation range, equation 2.27 can be rewritten as

$$I \propto V_b \rho_S(0, E_{F,S}) e^{-2\frac{\sqrt{2mU}}{\hbar}d} \tag{2.28}$$

where $\rho_S(x, E)$ is the local density of states (LDOS) of the sample defined as the number of electronic states of a system in the range between E and E+dE weighted by the probability $|\Psi_n(x)|^2$ of a particle to be at position x

$$\rho(x, E) = \sum_{\varepsilon_n} |\Psi_n(0)|^2 \, \delta(\varepsilon_n - E), \tag{2.29}$$

where $\delta(\cdot)$ is the Dirac delta distribution.

Equation 2.28 shows that the measured current is proportional to the local density of states of the sample. However, it contains only a proportionality between the current and the terms at the right-hand-side. For a more rigorous calculation of the current one has to resort to the Fermi's Golden rule after the proper calculation of the tunneling matrix element. This has been done by Bardeen[15] that, instead of solving the Schrödinger equation for the three domains (sample-vacuum-tip) simultaneously with appropriate boundary and continuity conditions, considered two separate subsystems (sample-vacuum and vacuum-tip) solving the Schrödinger equations separately and using time-dependent perturbation theory assuming weak coupling between the two electrodes for the calculation of the transfer rate of electrons between the sample and the tip. Finally, under these assumptions, the expression for the current becomes

$$\begin{aligned} I = & \frac{4\pi e}{\hbar} \int_{-\infty}^{+\infty} \left[f\left(E_F - eV_b + \xi\right) - f\left(E_F + \xi\right) \right] \\ & \rho_S(E_F - eV_b + \xi) \rho_T(E_F + \xi) \left| M \right|^2 d\xi \end{aligned} \tag{2.30}$$

where $f(\cdot)$ is the equilibrium Fermi-Dirac function, ρ_S and ρ_T are the density of states of the sample and tip, respectively, and $|M(\cdot)|^2$ is the squared matrix element, that in a first approximation can be replaced by the transmission coefficient T.

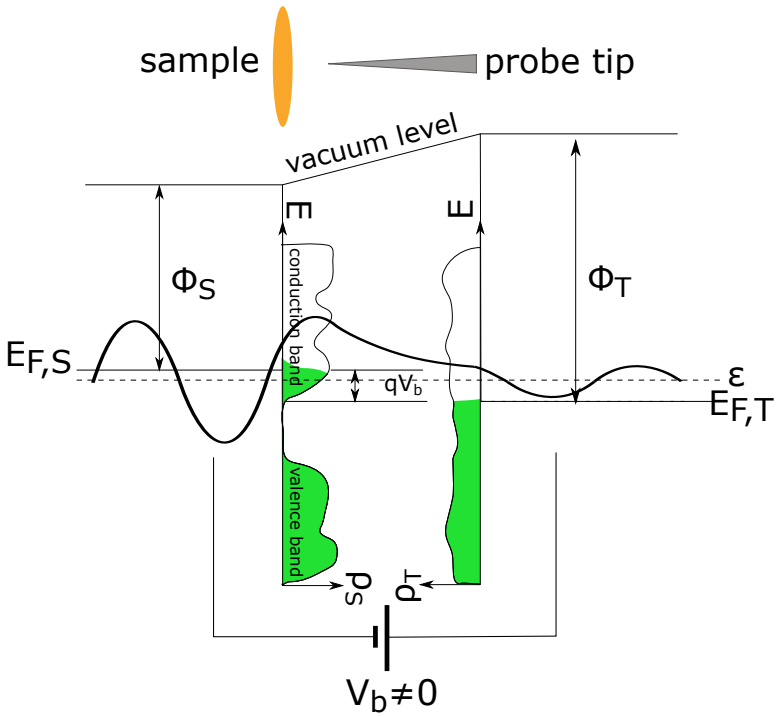

Figure 2.13: Sketch of a semiconductor sample and metal tip at different potentials to allow for the flow of a tunneling current for STM measurements. ρ_S and ρ_T represent the density of states of the sample and tip respectively, where it is clearly visible a band gap in the sample.

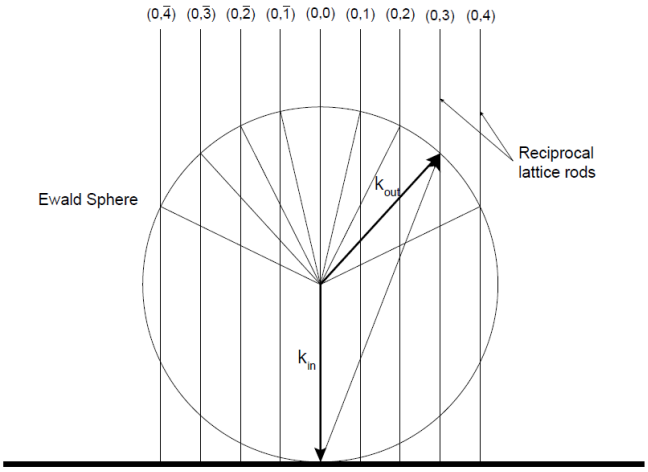

Figure 2.14: Ewald construction for solid surfaces. k_i is the incident electron wave-vector, k_f is the diffracted electron one.

$$T \propto exp\left[\frac{-2d}{\hbar}\sqrt{2m\left(\frac{\Phi_T + \Phi_S}{2} + \frac{eV_b}{2} - \xi\right)}\right] \tag{2.31}$$

Moreover, at T=0K, the Fermi-Dirac function reduces to a step function and the complexity of equation 2.30 decreases to the evaluation an integral over the energy window defined by the bias voltage V_b

$$I = \frac{4\pi e}{\hbar}\int_0^{eV_b} \rho_S(E_F - eV_b + \xi)\rho_T(E_F + \xi)\,|M|^2\,d\xi \tag{2.32}$$

Finally, figure 2.13 shows the more interesting case for this thesis of a semiconductor probed by the STM tip. Differently from the previous metal-metal case studies, the density of states of the sample presents a gap, thus, depending on the width of the sample energy band gap the bias voltage V_b must be properly tuned in order to probe the sample filled or empty states.

2.5 Low Energy Electron Diffraction

Low Energy Electron Diffraction (LEED) is an experimental technique useful for the analysis of long-range order of surfaces in crystalline solids. It was discovered in 1927 by Davisson and Germer while investigating diffraction by a nickel crystal[16]. In the single scattering approximation, electrons impinging on the sample are elastically scattered following the Bragg's Law: $a\sin\varphi = n\lambda$, where a is the surface lattice parameter, φ is the diffraction angle, n is an integer value and λ is the de Broglie wave length. The use of low

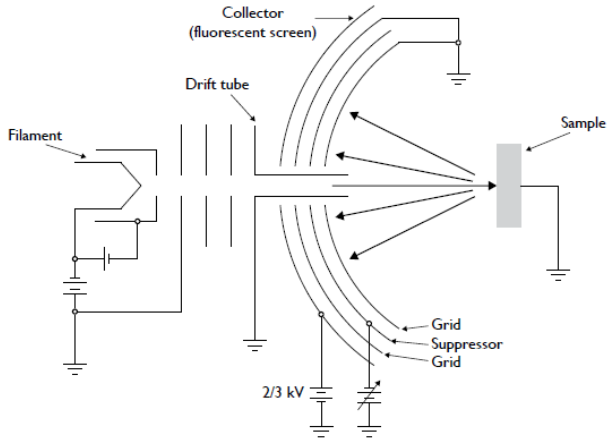

Figure 2.15: Schematic drawing of a LEED instrument.

energy electrons in the range 20-400 eV guarantees the surface sensitivity, as already shown in figure 2.2. In order to interpret diffraction in the reciprocal space, two laws must be taken into account: the energy conservation $|k_f|^2 = |k_i|^2$ (requirement for the elastic scattering) and the conservation of the parallel component of the momentum for a two-dimensional lattice, given by the Laue condition $k_f^{\parallel} - k_i^{\parallel} = \Delta k^{\parallel} = g$, where g is the surface reciprocal lattice vector, $k_f^{\parallel}$ and $k_i^{\parallel}$ are the components of the incoming and final scattered electron wave vectors. This last condition is graphically interpreted through the Ewald sphere, reported in figure 2.14. In a bidimensional reciprocal space, reciprocal lattice points are distributed along rods perpendicular to the crystal surface in correspondence to the points of the 2D reciprocal lattice. This can be explained by considering the periodicity of the third dimension infinite in the real space; as a consequence, in the reciprocal space, the lattice points are infinitely close to each other, forming the lines. The interception between these rods and the Ewald sphere, which radius depends on the kinetic energy of the electrons, are the solutions of the Bragg's law.

The LEED is an instrument that can be easily found in surface science laboratories, as it is relatively inexpensive and needs only a UHV chamber. A schematic drawing is provided in figure 2.15. An electron gun produces electrons that are subsequently collimated and accelerated to the desired energy. The electrons hit the sample, they are backscattered and collected by a florescent screen.

2.6 Elettra synchrotron radiation facility

Elettra is a third generation synchrotron radiation facility located in Basovizza (Trieste - Italy) that covers a spectral range spanning from infrared to

hard X rays. When we talk about synchrotron radiation, we mean the light produced by bunches of relativistic electrons accelerated in a storage ring. According to the theory developed by Iwanenko[17] and five years later by Schwinger[18], charges accelerated close to the speed of light on a curved trajectory emit a highly collimated photon beam in the tangential direction. In a synchrotron facility, electrons are forced to follow a curvilinear orbit by magnetic fields: *bending magnets* are the simplest devices to keep electrons in a curvilinear path and they produce a very broad band spectrum. Other magnetic devices such as quadrupoles and sextupoles control the path and radio-frequency cavities reintegrate the energy lost by the electrons while emitting light. On the straight sections of the ring, insertion devices can be hosted: undulators and wigglers are periodic arrays of magnets that force the incoming electrons to follow a wiggling trajectory and emit bright X-rays. The great benefit of exploiting a synchrotron radiation is the high brilliance, defined as the photon flux per unit solid angle and unit solid area at a given frequency: it is 10 billion times higher that the one of other X-rays conventional sources. Another fundamental advantage is the energy tunability: in conventional sources, the energy of the photons is fixed, and depends on the material of the anode. Elettra can operate at two different electron energies: 2.0 GeV and $\sim$ 310 mA, which is particularly suitable for the low energy beamlines, and 2.4 GeV and $\sim$ 160 mA, convenient for high energy photons. The facility works in a top-up mode, in which current is kept constant during operation thanks to the booster that provides electrons without affecting the run of the machine. 28 beamlines utilize the light for different purposes, such as spectroscopy, microscopy, diffraction, scattering and lithography.

2.7 The SuperESCA beamline at Elettra

SuperESCA was the first beamline of Elettra, operating since 1993[19] and it is optimized for photoelectron spectroscopy measurements with soft X-rays. The radiation source is a two-sections 46 mm-period undulator with 98 periods, capable to produce horizontally polarized light, with high flux and high resolution. The photon energy range spans from 90 eV up to 1800 eV (depending also on the energy of the electrons in the ring); the energy can be varied by setting the undulator gap value from a minimum of 13.5 mm to a maximum of 40 mm. The light produced by the undulator is pre-focused in the sagittal plane into the entrance slit, then monochromatized and finally re-focused into the centre of the experimental chamber by an ellipsoidal mirror. Ultra-high vacuum (UHV), with a base pressure of 10^{-10} - 10^{-11} mbar, is required to perform photoelectron spectroscopy. This condition is related to the IMFP of the electrons in the residual gas pressure, that must be large enough to allow them to reach the analyzer avoiding scattering effects with residual gas molecules. Moreover, UHV is needed to keep the surface of the

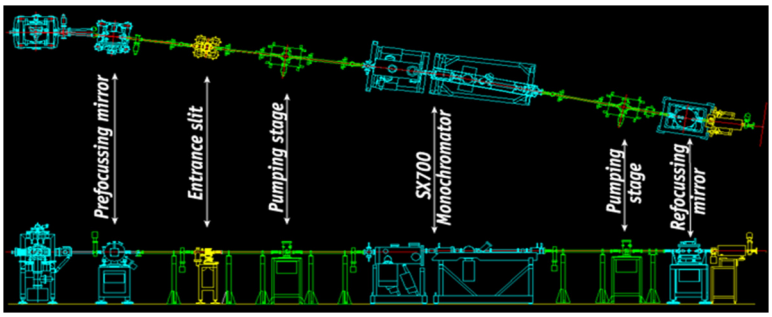

Figure 2.16: Schematic drawing of the SuperESCA beamline at Elettra

sample free from contaminants, preserving the accuracy of the measurements. The time rate of change of the concentration of molecules is expressed by the Hertz-Knudsen formula[20]

$$\Phi = \frac{P}{\sqrt{2mk_BT}} \tag{2.33}$$

where P is the gas pressure, m is the molecular mass, k_B is the Boltzmann constant and T is the sample temperature. Assuming that the sticking probability of the contaminants is 1, the surface would be covered in just few seconds with a partial pressure of $\sim 10^{-6}$ mbar. For this reason, a good pumping system and a bake out procedure are needed to obtain UHV conditions. The experimental station consists of two UHV chambers placed one on top of the other, separated by a gate valve, as shown in figure 2.17. The stainless steel top chamber is dedicated to the preparation of the samples and it is equipped with a sputter gun for sample cleaning, a plasma source and several feedthroughs for evaporators. This chamber is also connected with a fast entry lock that allows to change the sample without breaking the UHV conditions, and with a gas line. Two different manipulators are available and they allow to move the sample from the preparation to the main chamber. The first is a modified CTPO manipulator from VG Instruments with 5 degrees of freedom: 3 translational (x, y, z) and 2 rotational (θ, ϕ) axes. Thanks to its fully motorized rotational movements, this manipulator is specifically designed for XPD investigations where the photoemission intensity is measured as a function of the emission angle. The other manipulator is a liquid He cryostat with four degrees of freedom (x, y, z, θ) and an allowed sample temperature in the range of 20-1500 K. This manipulator allows to perform photoemission experiments where very low temperatures are needed. The experimental chamber is entirely made of μ-metal, a particular Ni-Fe alloy with a high magnetic permeability, that screens the chamber from external magnetic field which can deflect the electrons trajectory. The experimental chamber is equipped with a Low Energy Electron Diffraction (LEED) apparatus, a monochromatized electron gun, a mass spectrometer, a gas inlet

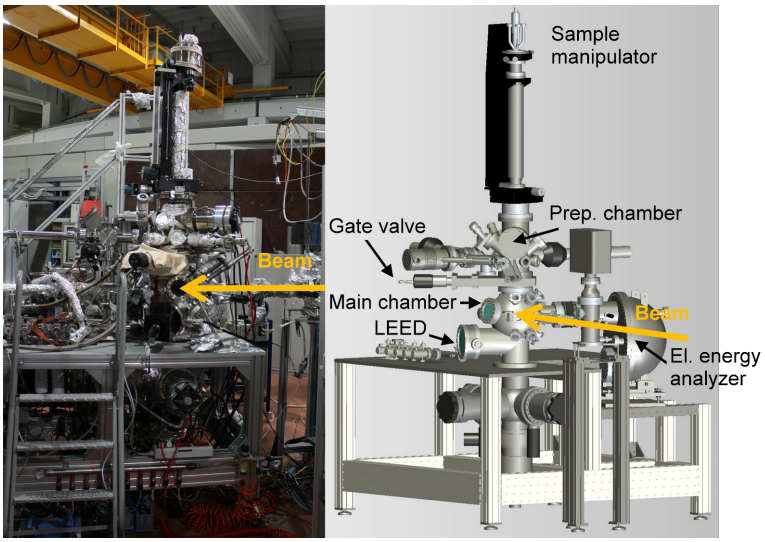

Figure 2.17: Experimental station at the SuperESCA beamline at Elettra.

system, evaporators and a partial yeald detector. The photoelectrons are collected with SPECS Phoibos electron energy analyzer with a mean radius of 150 mm. This electron energy analyzer has a hemispherical geometry: two concentric electrodes of different radii are held at a proper voltage, as shown in figure 2.18. Thanks to this geometry, the incoming electrons are linearly dispersed depending on their kinetic energy along the exit slit. The potential difference that has to be satisfied in order for the photoelecton with a given kinetic energy E_0 to reach the exit slit, follows this relation:

$$V_2 - V_1 = V_0 \left(\frac{R_2}{R_1} - \frac{R_1}{R_2} \right). \tag{2.34}$$

E_0 is also known as *pass energy*, where $E_0 = eV_0$. Only electrons with kinetic energy E_0 will follow an orbit with radius $R_0 = (R_1 + R_2)/2$, that will allow them to reach the exit slit and be revealed. The total energy resolution of the instrument depends on the divergence of the electron beam (represented by an angular offset α), on the selected pass energy and on the geometrical parameters of the analyzer:

$$\Delta E = E_0 \left(\frac{w_{en} + w_{ex}}{4R_0} + \frac{\alpha^2}{4} \right), \tag{2.35}$$

where w_{en} and w_{ex} are the respective widths of the entrance and exit slits. From eq. 2.35, it is clear that the energy resolution can be improved either by increasing R_0 or by decreasing E_0.

The analyzer is equipped with a home-made detector, developed at Elettra-Sincrotrone Trieste[21]. The photoelectrons are collected by two microchannel plates, which function is to amplify the impinging signal. Two working

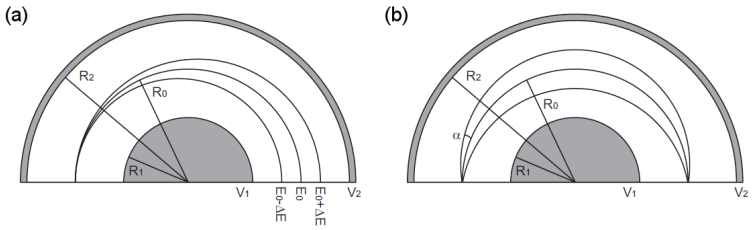

Figure 2.18: Schematical drawing of the (a) energy dispersion and (b) focusing properties of a hemispherical electron energy analyzer.

configurations are possible: *scanning* (*sweep*) mode or *fixed* (*snapshot*) mode. In the scanning mode, the pass energy is fixed and the voltages applied to the electrostatic lenses are swept, so that each channel of the detector counts electrons with the selected kinetic energy for an interval equal to the selected time window. In the fixed mode. The acquisition time can be drastically reduced: this procedure exploits the relation between the energy of the electron and its position on the detector. If the energy range covered by the detector is wide enough and if the number of available channels is sufficiently high to clearly resolve the photoemission features, it is possible to acquire a detector image and obtain the photoemission spectrum in one single shot, reducing the acquisition time down to 100 ms per spectrum. This makes SuperESCA a state-of-art beamline where to monitor in real-time chemical reactions occuring at surfaces by means of fast-XPS, but also to prevent sample contamination due to residual gas during time-consuming measurements that require the acquisition of thousands spectra, as in the case of the XPD investigations. These two techniques have been largely used to carry out the studies reported in this thesis.

At SuperESCA, an STM 150 Aarhus by SPECS is also available on CoSMoS, a separate UHV chamber.

2.8 The APE beamline at Elettra

The APE facility[22] consists of two end stations connected to two distinct beamlines: the low energy beamline (APE-LE) that operates within the 8-120 eV photon energy range and it is devoted to high resolution ARPES, and the high energy beamline (APE-HE) that exploits a 150-1600 eV photon energy range for XAS, XMCD, XMLD, XPS measurements. APE-LE hosts VG-Scienta DA30 electron energy analyzer that operates in deflection mode and allows for detailed k-space mapping at fixed sample geometry (fixed angle). The total measured energy resolution (analyzer, temperature, photons) is $\sim$6 meV, while the angular resolution is $<0.2°$. The high energy end station hosts complementary spectrometers allowing for soft-X-ray absorp-

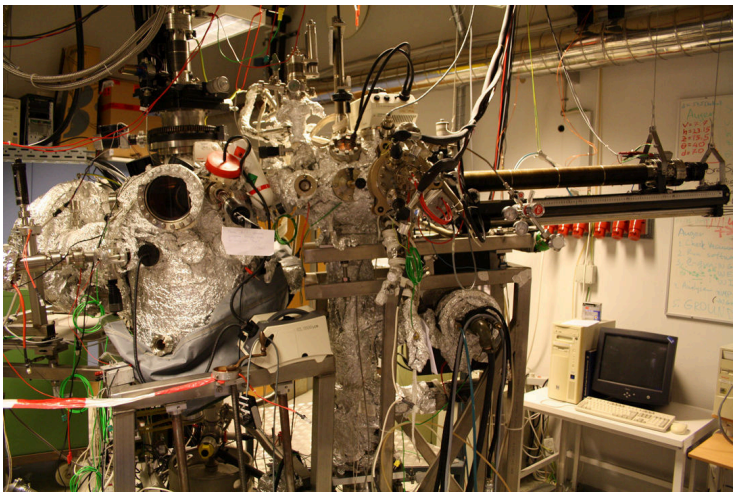

Figure 2.19: The experimental chamber of the SGM3 beamline at Astrid.

tion (XAS), magnetic dichroism (XMCD, XMLD) and X-ray photoelectron spectroscopy (XPS). Samples can be loaded into the APE system via two differentially pumped load-locks and then transferred in UHV to any of the preparation chambers, to STM and to both end stations. APE also allows the integration of users' specialized sample growth chambers, which can be connected to the main sample distribution chamber and have full access to the off-beam and on-beam facilities. Also two VLEED-based scattering chambers for the determination of spin direction of the photo-emitted electrons are available. Photons with chosen polarization are emitted by two non-collinear Apple II type insertion devices. Both end stations are equipped with liquid He cryostats. The interconnected set of UHV chambers includes state-of-the-art surface preparation and survey such as Ar ion sputtering, annealing, controlled evaporation and LEED/Auger characterization.

2.9 The SGM-3 beamline at Astrid

The SGM-3 beamline is located in the synchrotron radiation source ASTRID2 in Aarhus Denmark[23] and it is optimized for valence band photoemission measurements. The radiation entering the beamline is produced by an undulator inserted in the ASTRID storage ring and it is focused on the entrance slit by a horizontal and a vertical spherical focusing mirrors. The selection of the photon in the 12-130 eV energy range is performed by a spherical grating monochromator consisting of three interchangeable gratings that use the first and third harmonic of the undulator. Finally, the beam passes through a movable exit slit and it is focused on the sample by a toroidal mirror.

The end station (see figure 2.19) consists of two different UHV chambers:

a first preparation chamber, where samples can be treated with Ne^+ ion sputtering and annealing up to 1573 K via electron bombardment using a tungsten filament on high voltage, and the main chamber, where measurements are performed in a typical base pressure of 2×10^{-10} mbar. The two chambers are separated by a valve, and are placed side-by-side. In order to insert a sample without venting the larger chambers, a fast entry load lock chamber with a wobble stick is present. Every chamber has its own manipulator: the first one, in the preparation chamber, is placed horizontally and allows the transfer of the sample to the main chamber, where the manipulator is vertical. This manipulator has four degrees of freedom (x, y, z and θ) and allows sample cooling to 30 K using liquid helium. The electron detection system placed in the main chamber consists of a SPECS Phoibos 150 mm analyzer, mounted at an angle of 50° with respect to the beamline, and equipped with a 2D-CCD detector with energy resolution better than 30 meV. The chamber is also furnished with a LEED spectrometer.

2.10 General experimental details

In this section, we report the experimental details and parameters common to the measurements described in the following chapters, if not elsewhere specified. The growth of all the samples was performed at the SuperESCA beamline of Elettra[19]. The substrates were prepared by repeated cycles of Ar^+ sputtering and annealing. The sample quality was checked with LEED and XPS.

In order to grow MoS_2 and WS_2, Mo and W were deposited from a homemade evaporator mounted in the main chamber on the side of the analyzer, consisting of a Mo/W filament annealed through direct current heating, and H_2S with a nominal purity of 99.8% was dosed through a controllable leak valve. During the growth, fast-XPS was performed to follow the layer growth in real-time. The Mo/W deposition rate was measured by means of a quartz microbalance and the monolayer (ML) for the dose rate is defined as the surface atomic density of the Au(111) surface, corresponding to 1.39×10^{15} atoms/cm^2.

The high resolution spectra were measured at room temperature with an overall energy resolution below 50 meV. The core level spectra were decomposed using a Doniach-Šunjić line shape[6] that accounts for the electron-hole pair creation near the Fermi level during the photoemission process, convoluted with a Gaussian broadening. A linear background was used. All the binding energies presented in this work are referenced to the Fermi level, measured in the same experimental conditions of each experiment.

The XPD patterns were acquired with different photon energies ($h\nu$) in order to change the corresponding electron kinetic energy (E_k) to enhance forward and backscattering conditions. The angular resolution was set at

$\sim \pm 2°$.

STM measurements were carried out on the CoSMoS facility at Elettra. The images were acquired at room temperature with a SPECS STM 150 Aarhus instrument equipped with a W tip. The samples were transferred through air from the chamber of SuperESCA to the STM chamber, where they were subsequently annealed up to ca. 800 K for 30 minutes.

ARPES data were taken at the SGM-3 beamline of the synchrotron radiation facility ASTRID2 in Aarhus [23]. The energy and angular resolution were better than 30 meV and 0.2°, respectively. The sample temperature was ∼30 K. The sample was transferred to Aarhus in air, then annealed in UHV at 770 K for 30 minutes to remove contaminants.

Spin-resolved ARPES measurements were taken at the APE beamline of Elettra[24], equipped with a VG-Scienta DA30 analyser and two very low energy electron diffraction (VLEED) spin polarimeters. The energy and angular resolution were better than 50 meV and 0.75°, respectively. Samples were transferred into the chamber in air and subsequently annealed up to ≈ 800 K. Measurements were taken at ≈ 80 K.

References

[1] Hertz, H. Ueber einen Einfluss des ultravioletten Lichtes auf die electrische Entladung. *Annalen der Physik* **1887**, *267*, 983–1000.

[2] Woodruff, D. P.; Bradshaw, A. M. Adsorbate structure determination on surfaces using photoelectron diffraction. *Reports on Progress in Physics* **1994**, *57*, 1029.

[3] Chen, C. J. *Introduction to Scanneling Tunneling Microscopy*; Oxford University Press, 1993.

[4] Yeh, J.; Lindau, I. Atomic subshell photoionization cross sections and asymmetry parameters: 1≤Z≤103. *Atomic Data and Nuclear Data Tables* **1985**, *32*, 1–155.

[5] Koopmans, T. Über die Zuordnung von Wellenfunktionen und Eigenwerten zu den Einzelnen Elektronen Eines Atoms. *Physica* **1934**, *1*, 104–113.

[6] Doniach, M., S.; Sunjic Many-Electron Singularity in X-ray Photoemission and X-ray Line Spectra from Metals. *Journal of Physics C* **1970**, *3*, 285–291.

[7] Rehr, J. J.; Albers, R. C. Scattering-matrix formulation of curved-wave multiple-scattering theory: Application to x-ray-absorption fine structure. *Physical Review B* **1990**, *41*, 8139–8149.

[8] García de Abajo, F. J.; Van Hove, M. A.; Fadley, C. S. Multiple scattering of electrons in solids and molecules: A cluster-model approach. *Physical Review B* **2001**, *63*, 075404.

[9] Woodruff, D. Adsorbate structure determination using photoelectron diffraction: Methods and applications. *Surface Science Reports* **2007**, *62*, 1–38.

[10] Dagotto, E. Complexity in Strongly Correlated Electronic Systems. *Science* **2005**, *309*, 257–262.

[11] Yan, J.; Zhang, Y.; Kim, P.; Pinczuk, A. Electric Field Effect Tuning of Electron-Phonon Coupling in Graphene. *Physical Review Letters* **2007**, *98*, 166802.

[12] Hinsche, N. F. et al. Spin-dependent electron-phonon coupling in the valence band of single-layer WS_2. *Physical Review B* **2017**, *96*, 121402.

[13] Binnig, G.; Rohrer, H.; Gerber, C.; Weibel, E. Surface Studies by Scanning Tunneling Microscopy. *Physical Review Letters* **1982**, *49*, 57–61.

[14] Binnig, G.; Rohrer, H. Scanning tunneling microscopy. *Surface Science* **1983**, *126*, 236–244.

[15] Bardeen, J. Tunnelling from a Many-Particle Point of View. *Physical Review Letters* **1961**, *6*, 57–59.

[16] Davisson, C.; Germer, L. H. Diffraction of Electrons by a Crystal of Nickel. *Physical Review* **1927**, *30*, 705–740.

[17] Iwanenko, D.; Pomeranchuk, I. On the Maximal Energy Attainable in a Betatron. *Physical Review* **1944**, *65*, 343–343.

[18] Schwinger, J. On the Classical Radiation of Accelerated Electrons. *Physical Review* **1949**, *75*, 1912–1925.

[19] Abrami, A. et al. Super ESCA: First beamline operating at ELETTRA. *Review of Scientific Instruments* **1995**, *66*, 1618–1620.

[20] Pizzini, S.; Sacchi, M. Modern techniques of surface science, 2nd edition. By D. P. Woodruff and T. A. Delchar, Cambridge University Press, Cambridge 1994, ISBN 0-521-42498-4. *Chemical Vapor Deposition* **1995**, *1*, 32–33.

[21] Cautero, G.; Sergo, R.; Stebel, L.; Lacovig, P.; Pittana, P.; Predonzani, M.; Carrato, S. A two-dimensional detector for pump-and-probe and time resolved experiments. *Nuclear Instruments and Methods in Physics Research, Section A: Accelerators, Spectrometers, Detectors and Associated Equipment* **2008**, *595*, 447–459.

[22] Panaccione, G. et al. Advanced photoelectric effect experiment beamline at Elettra: A surface science laboratory coupled with Synchrotron Radiation. *Review of Scientific Instruments* **2009**, *80*, 043105.

[23] Hoffmann, S.; Søndergaard, C.; Schultz, C.; Li, Z.; Hofmann, P. An undulator-based spherical grating monochromator beamline for angle-resolved photoemission spectroscopy. *Nuclear Instruments and Methods in Physics Research Section A: Accelerators, Spectrometers, Detectors and Associated Equipment* **2004**, *523*, 441–453.

[24] Bigi, C.; Fujii, J.; Vobornik, I.; Das, P. K.; Benedetti, D.; Salvador, F.; Panaccione, G.; Rossi, G. Very Efficient Spin Polarization Analysis (VESPA): New Exchange Scattering-based Setup for Spin-resolved ARPES at APE-NFFA Beamline at Elettra. *ArXiv e-prints* **2016**,

Chapter 3

Growth and characterization of single-layer MoS_2 on Au(111)

3.1 Introduction

As already discussed in the first chapter, graphene with its outstanding electronic[1], optical[2], thermal[3], and mechanical properties[4], has boosted the research on other 2D materials such as the transition metal dichalcogeniges (TMDCs)[5] which have extraordinary properties especially for applications in the fields of electronics and optoelectronics[6–10]. The most investigated member of this family is molybdenum disulphide (MoS_2), which shows noteworthy properties in its monolayer form. In order to fully exploit its potential in real devices, such as in field effect transistors, large area and high quality single layers of MoS_2 are demanded. The quality of the layer is reduced by the presence of defects; in particular grain boundaries, formed by the coalescence of islands, leading to poor electrical and mechanical performance of the layer[11–14]. However, the density of grain boundaries is largely suppressed if randomly oriented or twin, i.e oppositely oriented, domains are not present and the layer has one single orientation.

Moreover, the presence of singly oriented domains would be highly desirable to exploit the spin and valley degrees of freedom, as described in chapter 1. In fact, for such applications, the presence of the mirror domain is no more acceptable. This is illustrated in figure 3.1 which shows the unit cell together with a schematic electronic structure of single layer molybdenum disulfide domains. It clearly appears that the one domain has opposite spin orientation in K and K' points of the 2D hexagonal Brillouin zone (in the figure, the blue and red colors of the split valence band maximum refer to the different spin orientation of these states) with respect to its mirror domain. Because of the different Berry curvatures in the two K valleys[16–18],

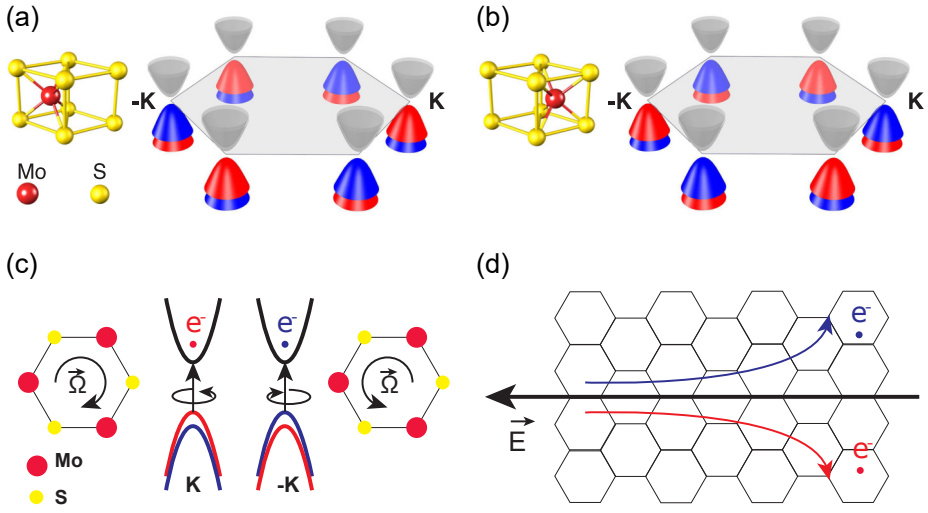

Figure 3.1: Structure, Brillouin zone and schematic band structure for two mirror domain orientations of SL MoS_2. The colors of the split valence band maximum (blue/red) refer to the different spin orientation of these states. (c) Schematic representation of the valley-dependent Berry curvatures $\vec{\Omega}$, representing the clockwise and counterclockwise hopping motions of the electrons in the K and K' valleys. Adapted from reference[15]. (d) Schematic of a valley Hall effect (VHE), where electrons belonging to the different valley are separated and move in the opposite directions, under the effect of an applied electric field $\vec{E}$.

electrons experience effective magnetic fields with equal magnitude but opposite signs[15]. This difference in interaction with the magnetic field allows to optically pump electrons selectively from a valley by means of circularly polarized light[19–22] and it allows electrons to drift in the presence of an in-plane longitudinal electric field giving rise to an Hall voltage (valley Hall effect)[15, 17, 23]. However, when both domains are present simultaneously, the spin and the valley polarization is lost on average and the valley Hall effect cannot take place.

Unfortunately, the growth of singly oriented domains is a challenge: van der Waals epitaxy of single layer TMDCs on weakly interacting substrates such as graphene[24], h-BN[25] and sapphire[26], produces an angular distribution of domains with preference for mirror domains, while, on the other hand, if a stronger interacting substrate is chosen, twin domains grow aligned with the substrate lattice[27]. Nevertheless, recently Fu et al. demonstrated that by adopting a high growth temperature and a slow dose rate of the precursors, the formation of antialigned grains is largely suppressed[27, 28].

In order to find a growth strategy to completely suppress the formation of twin domains, we deeply studied an already published growth procedure of single-layer MoS_2 on Au(111)[29] by physical vapour deposition (PVD) consisting in repeated cycles of Mo evaporation in a H_2S environment on the Au(111) surface at room temperature followed by high temperature annealing[27, 30]. We started our investigation by focusing on the mechanisms that lead to the formation of the MoS_2 layer to gain new insight into the processes involved in the transition from the sulfided Mo clusters on Au(111) to single layer MoS_2. HR-XPS was used to explore the interactions between the Au surface and the dichalcogenide ad-layer by inspecting the core level shifts in Au $4f_{7/2}$ and S 2p. We detected the growth of an additional component in the Au 4f core level owing to the adsorbate-substrate interactions. Such interactions were also observed in the S 2p spectra that showed a component related to bottommost sulfur in 'S-Mo-S' sandwich structure at higher binding energy with respect to that of top layer sulfur.

Having obtained important information from this study, we successfully developed a new PVD growth procedure suitable for the formation of singly oriented domains of MoS_2 on the Au(111) substrate by keeping yhe sample at high temperature during dose. We demonstrated the single orientation character of the MoS_2 layer by photoelectron diffraction and measured the complete spin polarization of the states near K and -K by spin- and angle-resolved photoemission.

3.2 Experimental details

The Au(111) substrate was prepared by repeated cycles of Ar^+ sputtering, and annealing at 920 K for 10 minutes, with 1 K s^{-1} heating and cooling

rate. The sample quality was checked with XPS which did not detect any trace of contaminants within the detection limit of 0.1% of a monolayer. The Au $4f_{7/2}$ the surface core level shift typical of the clean surface[31]. The long-range order was verified by acquiring LEED patterns on the freshly prepared sample, showing a hexagonal (1x1) pattern together with the extra spots of the herringbone reconstruction. Two different procedures were followed for the growth of MoS_2 on Au(111). The first was performed by dosing atomic Mo at the rate of 0.02 ML (see below for the definition of ML) per minute at room temperature in a backfilled chamber with H_2S pressure ($2\,x\,10^{-6}$ mbar) and post annealing at 0.5 K s^{-1} up to 823 K in H_2S atmosphere ($2\,x\,10^{-6}$ mbar), following an already established procedure[29], that is called temperature-programmed growth (TPG). The second method consisted in dosing atomic Mo at the rate of 0.005 ML per minute in a background pressure of $2\,x\,10^{-6}$ mbar of H_2S onto the clean Au(111) substrate kept at 873 K (high temperature growth (HTG)). During the growth, fast-XPS was performed looking simultaneously the Mo 3d and S 2p core levels with 360 eV photon energy[32]. The S 2p, Mo 3d, and Au 4f high resolution spectra were measured using photon energies of 260, 360 and 136 eV, respectively. The XPD patterns for the S 2p were acquired at $h\nu = 270$ eV (E_k ~108 eV) for the top S layer, and at $h\nu = 560$ eV (E_k ~397 eV) for the bottom S layer. The XPD measurements for Mo 3d were performed with photon energy $h\nu$=360 eV corresponding to electron kinetic energies of 130 eV.

For a more complete description of the experimental parameters, see chapter 2.10

3.3 Results and discussion

3.3.1 MoS_2 temperature programmed growth (TPG)

Figure 3.2 reports the temporal evolution of the Mo 3d and S 2p core level spectra during Mo evaporation on the Au(111) substrate at room temperature in H_2S atmosphere. H_2S pressure was kept at $2\,x\,10^{-6}$ mbar during the evaporation and during the whole synthesis in order to provide sulfur to Mo and prevent the formation of an alloy with Au[29]. The Mo $3d_{5/2}$ and S $2p_{3/2}$ peaks grow at 228.05 eV and 161.41 eV and are ascribable to the formation of presulfided Mo species. Baker et al. showed that, depending on the degree of sulfidation of Mo, namely the stoichiometry of the MoS_x species, the binding energy of Mo 3d and S 2p components changes linearly [33]. By extrapolating from the plot reported in their paper, it is possible to conclude that the as-dosed sample has x~1. The dose shown here resulted in a MoS_2 coverage after annealing of 0.2 ML, where 1 ML is defined as one complete layer of MoS_2. From here on, we will use this definition of ML, unless otherwise stated. The way the coverage is estimated will be explained in section 3.3.3.

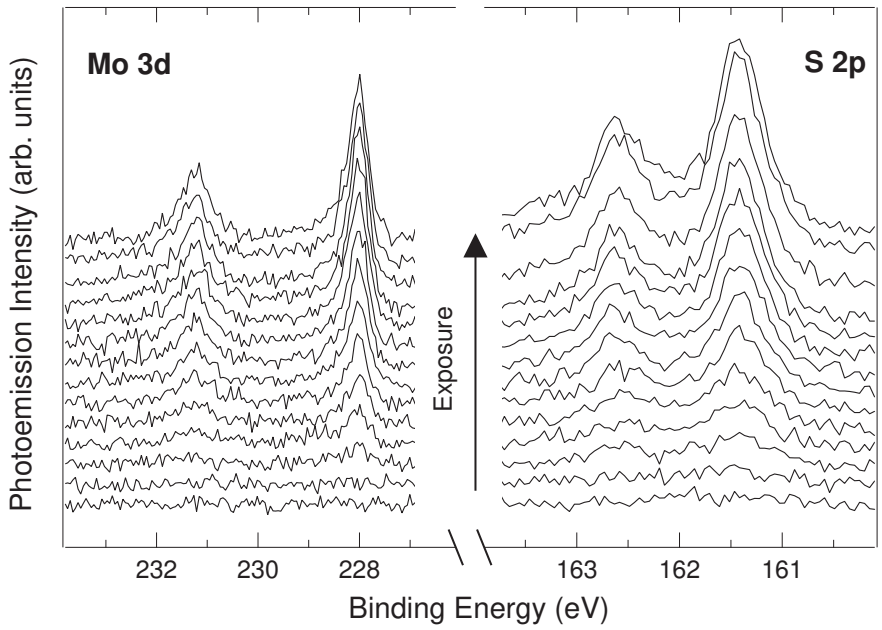

Figure 3.2: Mo 3d and S 2p core level spectra measured at $h\nu = 360$ eV during Mo evaporation in H_2S atmosphere. Total exposure time = 5 minutes.

In order to convert the pre-sulfided clusters into MoS_2, we performed an annealing in H_2S at a pressure of 2×10^{-6} mbar at the rate of 0.5 K/s while looking at real-time Mo 3d and S 2p XPS spectra acquired simultaneously at 360 eV photon energy, as shown in figure 3.3. Both intensity plots of Mo 3d in (a) and S 2p in (c) evolve accordingly. Upon annealing above 550 K, the peaks move gradually to higher binding energy. The final binding energy position is reached above 823 K and the temperature was kept at that value until no changes in the spectra were visible. A further annealing at 873 K did not affect the spectra. The temperature was not further increased to avoid S desorption with the eventual formation of Mo-Au alloy[29]. The fast XPS spectra series was fitted and figure 3.3 (b) and (d) show some selected spectra collected during the annealing. The fitting parameters for these spectra were chosen based on the fittings of the high resolution spectra measured at room temperature, taken before (not reported here) and after the annealing (that will be discussed later). When fitting the spectra measured at high temperature, higher values for the gaussian parameters have been used with respect to the room temperature HR spectra because of the peaks thermal broadening. The related components in Mo 3d and S 2p spectra have been marked with the same colors. Figures 3.3 (e) and (f) show the evolution of the different components of Mo $3d_{5/2}$ and S $2p_{3/2}$ spectra, respectively.

As the temperature increases, the intensity of the grey components (M1,

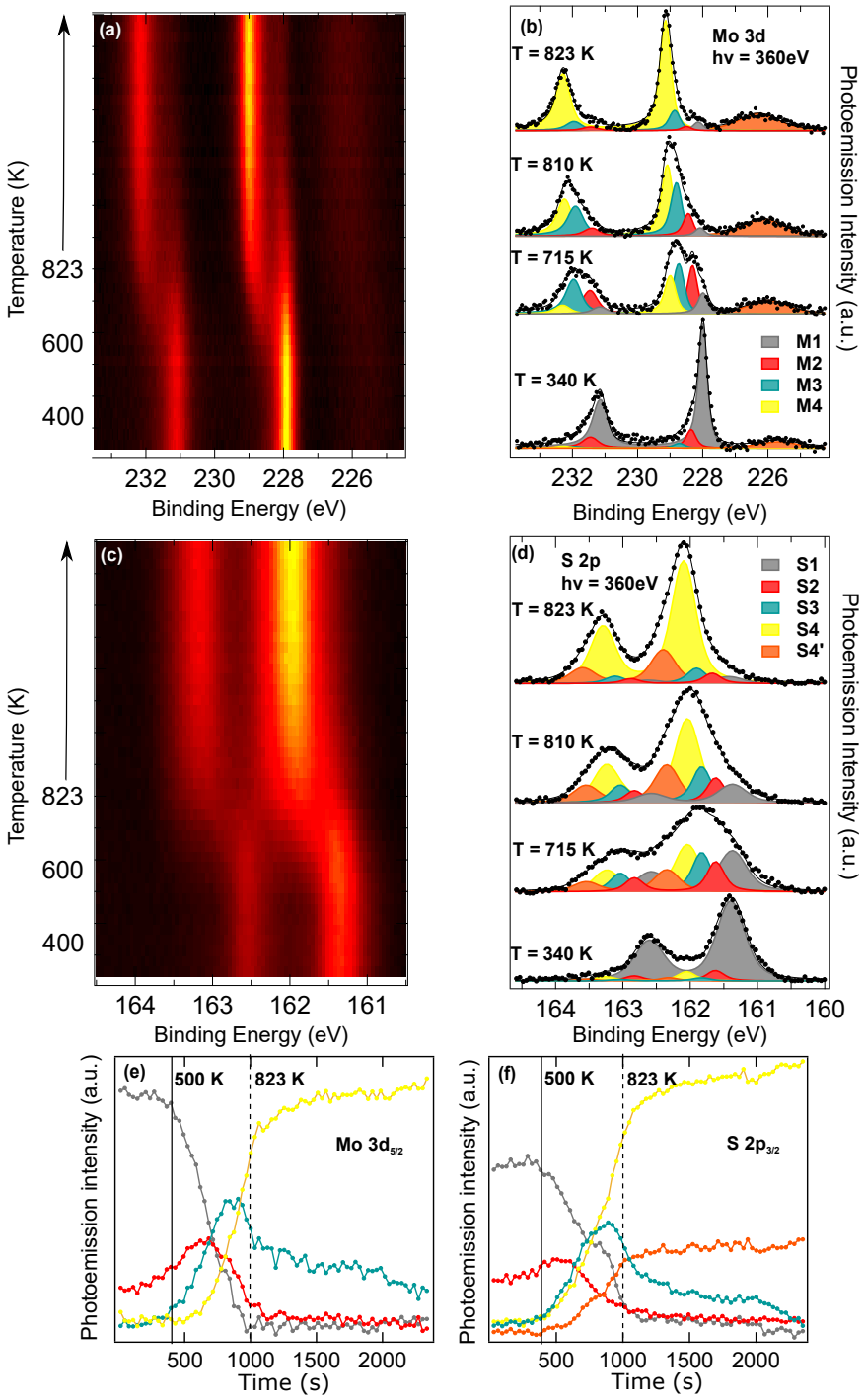

Figure 3.3: (a) Mo 3d and (c) S 2p fast-XPS intensity plot while annealing. The annealing rate is 0.5 K s^{-1} up to 823 K; then the temperature is kept constant. (b) Mo 3d and (d) S 2p fast-XPS spectra obtained at 360 eV photon energy, showing the evolution of different components together with the spectral contributions resulting from peak fit analysis, while annealing after the dose at room temperature. Intensity profile of the different components of the (e) Mo 3d and (f) S 2p fast XPS spectra. The vertical lines denote the temperature of 500 K (solid line) and 823 K (dashed line).

S1) gradually decreases, aiding the transformation towards components at higher binding energy, that are related to non stoichiometric MoS species (red and blue, (M2,S2) and (M3,S3), respectively) and the final MoS_2 layer (yellow (M4,S4) and orange S4'). The M2 component is centered at 228.35 eV for Mo 3d whereas the S 2p core level of S2 is at 161.64 eV. These components are present from the beginning of the annealing process; as the annealing proceeds, initially they grow as a result of sulfidation of Mo already available on the surface, then they lessen, thus revealing that these M2 and S2 components act as transitional compounds towards the formation of single layer MoS_2 nano-islands. The blue component, centered at 228.74 eV (M3) in Mo 3d and 161.87 eV (S3) in S 2p spectrum is not present before the annealing and it raises when the temperature reaches 550 K (marked with a solid line in the intensity profiles). While proceeding with the annealing, these components have a maximum at 750 K, then they decrease. We attribute these components to the presence of undercoordinated and incompletely sulfided clusters with a $MoS_{1.5-1.6}$ stoichiometry[33]. However, looking at the intensity profile (figure 3.3 (e) and (f)), M3 has a different behavior than S3, growing faster in the initial part of the annealing. This behavior can be explained by considering that at the beginning of the MoS_2 synthesis, at very low MoS_2 coverage, small nano-island preferentially Mo-terminated are formed. This statement is consistent with DFT calculations on triangular MoS_2 nanoparticles on Au (111) that predict a Mo 3d peak for edge Mo with a BE of 228.8 eV[34], in very close agreement with our value of 228.74 eV. Therefore, we conclude that the M3 component includes the contribution of partially sulfided species as well as that of the edges of the small islands. With the increase of the temperature, as islands grow bigger, the intensity of M3 decreases because the ratio between the number of Mo atoms at the edges with respect to those in the basal plane of MoS_2 islands decreases. On the other hand, we were not able to identify a component in the S 2p spectrum related to the S present at the edges of the islands because, according to DFT calculations[34], it is predicted to be centered at 162.85 eV BE, higher than the BE position of S4.

Finally, it can be noted that during the annealing at 823 K (marked with a dashed line in the intensity profiles of figure 3.3 (e) and (f)), M1, M2 and M3 for the Mo 3d spectrum and S1, S2 and S3 for the S 2p spectrum components convert into M4, centered at 229.19 eV and into S4 at 162.15 eV and S4' at 162.41 eV, related to the top and bottom S of the MoS_2, as will be shown in the following paragraphs. These components are characteristic of the single layer MoS_2 grown on Au(111)[29, 34]. However, the conversion is not complete, since the final spectra still present components related to incompletely sulfided MoS_2 clusters. Further information can be gained by considering the total intensity of the Mo 3d and S 2p peaks at the beginning and in the end of the annealing. While the Mo 3d signal is basically constant, the total intensity of the S 2p core level strongly increases. This can be

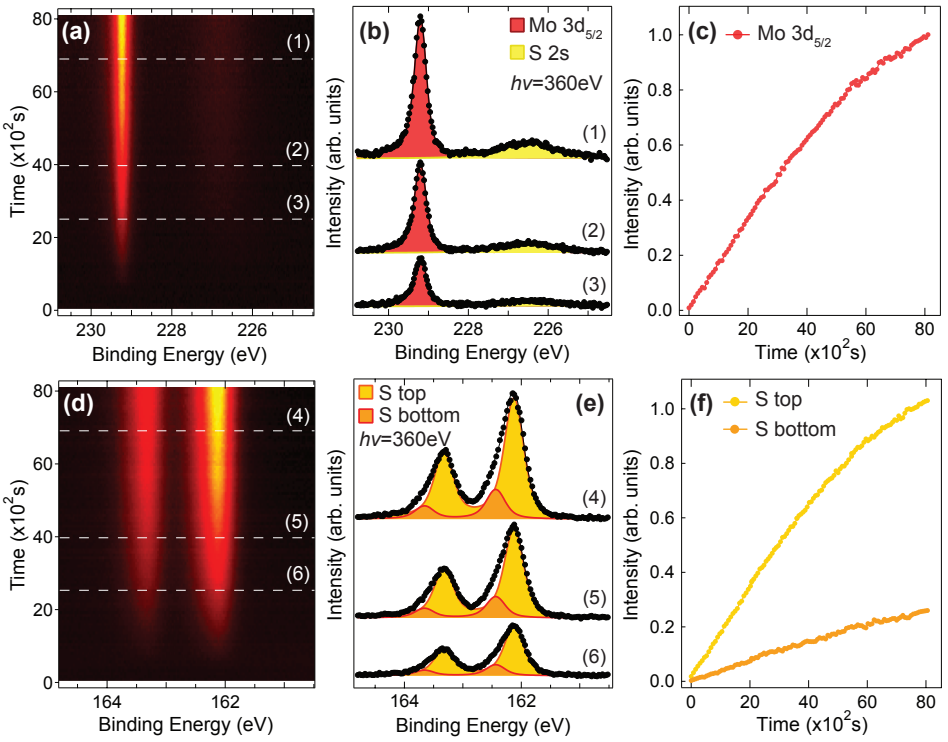

Figure 3.4: Intensity plot of the sequence of fast-XPS spectra of Mo 3d (a) and S 2p (d) core levels acquired at 360 eV photon energy while growing MoS_2. Mo 3d (b) and S 2p (e) core level spectra together with the spectral contributions resulting from the peak fit analysis, at different stages of the growth, as represented by the dashed lines in (a) and (d), respectively. Photoemission intensities obtained from the fit of the fast-XPS spectra, showing the evolution of the Mo $3d_{5/2}$ (c) and S $2p_{3/2}$ (f) for the two components of the S $2p_{3/2}$ core levels that belong to the top and bottom sulfur, as explained in the following. The final MoS_2 coverage is 0.65 ML.

explained by taking into account that the sulfur amount on the sample during Mo evaporation is not sufficient to complete the two layers of sulfur of MoS_2. The lacking sulfur is provided by H_2S during the annealing, leading to a higher intensity of the components in the end.

3.3.2 MoS_2 high temperature growth (HTG)

From the study of the TPG growth method, and in particular from the fast-XPS spectra acquired during the annealing, we could verify that the temperature at which MoS_2 forms is around 820 K. Considering that at higher temperature the mobility of the atoms on the surface is enhanced, Mo was dosed in H_2S pressure keeping the substrate at 873 K, with the aim of promoting a better order of the layer. The Mo evaporation was 0.005

ML/minute (where ML now refers to the Au(111) surface atomic density). Figure 3.4 (a) and (d) report the intensity plots of the sequence of fast-XPS spectra of Mo 3d and S 2p core levels, respectively, acquired simultaneously at 360 eV photon energy during the growth. Unlike the case of TPG reported in section 3.3.1, from the very beginning, both the Mo $3d_{5/2}$ and the S $2p_{3/2}$ binding energy positions of 229.19 eV and 162.15 eV, respectively, are those of MoS_2 monolayer[29, 34].

Figure 3.4 (b) and (e) present the XPS spectra taken during the growth, specifically after 40 minutes, 65 minutes and 115 minutes from the beginning. Also in this case, the line shapes to fit the series of spectra were extracted from the high resolution measurements at room temperature after the growth, letting the Gaussian parameter enlarging. From the spectral contributions resulting from the peak fit analysis, no shift in binding energy or appearance of new components are detected for both Mo and S; the only parameter that changes is the peak intensity which increases almost linearly, except when approaching saturation, as shown in figure 3.4 (c) and (f). It is worth noting that this growth mechanism notably differs from the TPG. Indeed, in the latter case a transition takes place during the annealing, leading to the formation of MoS_2. Moreover, the presence of side products with the TPG method is inevitable and therefore it leads to a poorer quality of the system. Also for the HTG method, as already pointed out in the literature for the TPG method[27], the formation of side products and bilayers beyond 0.8 ML may be possible. Therefore, the growth was stopped at a coverage of 0.65 ML. Another important issue to emphasize is the different Mo evaporation rate in the two methods: in the TPG the Mo evaporation rate was four times higher than in the present case. This can be explained as follows: in the TPG method, Mo is evaporated onto the Au(111) substrate at room temperature and the formation of MoS_2 takes place only during the annealing of the system. In order to obtain a high MoS_2 coverage, this cycle of evaporation-annealing must be repeated several times to achieve the desired coverage because a single Mo evaporation would result in the formation of pre-sulfided species or Mo clusters that cannot be completely converted during the annealing to form MoS_2[27]. In the HTG approach, instead, it is fundamental that each Mo atom approaching the surface reacts immediately with S to form MoS_2. Therefore, provided that it is not technically possible for our setup a higher H_2S background pressure, the evaporation rate must be slower. It is important to stress that the possibility to follow in real-time the growth process is essential to reproduce these results. Indeed, fast-XPS allowed us to carefully tune and adjust the parameters, such as H_2S pressure and Mo evaporation rate. In this way we avoided undesired Mo clusters and partially sulfided species, which appear at lower binding energy, and have been discussed in the previous section. The appearence of these byproducts compromises the quality of the layer, as it is not possible to convert them into MoS_2 even after prolonged annealing in H_2S atmosphere without dosing

Mo.

3.3.3 High resolution photoemission spectra

Figure 3.5 shows the high resolution spectra of Au $4f_{7/2}$, Mo 3d and S 2p core levels for the TPG and HTG grown samples and table 3.1 summarizes the line shape parameters that were used to fit the Mo 3d and S 2p components relative to the MoS_2 layer.

Table 3.1: Doniach-Šunjić line shape parameters for the different components of the Au $4f_{7/2}$, Mo 3d and S 2p core levels acquired at room temperature with 136 eV, 360 eV and 260 eV photon energy, respectively. L is the Lorentzian width, α is the asymmetry parameter and G is the Gaussian width (see section 2.1.2 for detailed information). BE is the binding energy of the components.

Au 4f $_{7/2}$ ($h\nu$=136eV)	L(eV)	α	G(eV)	BE(eV)
Bulk (B)	0.31	0.02	0.09	84.00
Surface (S)	0.37	0.02	0.23	83.67
MoS_2 (M)	0.37	0.02	0.23	83.89
Mo 3d ($h\nu$=360eV)	L(eV)	α	G(eV)	BE(eV)
$3d_{5/2}$	0.20	0.05	0.14	229.19
$3d_{3/2}$	0.43	0.05	0.14	232.34
S 2p ($h\nu$=260eV)	L(eV)	α	G(eV)	BE(eV)
$2p_{3/2}$ S4	0.18	0.03	0.16	162.15
$2p_{1/2}$ S4	0.18	0.03	0.16	163.35
$2p_{3/2}$ S4'	0.23	0.02	0.21	162.44
$2p_{1/2}$ S4'	0.23	0.02	0.21	163.64

The Au $4f_{7/2}$ core level spectra for the clean Au(111) surface and for 0.7 ML MoS_2 coverage are shown in figure 3.5 (a). The Au spectra here reported are relative only to the TPG growth, as we did not observe any significant difference between the Au $4f_{7/2}$ spectra in the two growth methods. The spectrum for the clean surface presents two components due to the bulk (B) at 84.0 eV and surface atoms (S) at 83.67 eV resulting in a surface core level shift of 330 meV, in close agreement with previous studies[35, 36]. The Au surface spontaneously undergoes a reconstruction and it densifies along the $<\bar{1}10>$ directions, resulting in a rectangular ($22x\sqrt{3}$) unit cell[37, 38]. Therefore, the S component is ascribable to the herringbone reconstruction. However, Au atoms forming the elbows of this structure are less coordinated and they might have a lower binding energy with respect to the others. For this reason, the spectrum of the clean Au cannot be fitted properly (see the blue circle in figure 3.5 (a)) in the lower binding energy region. Previous

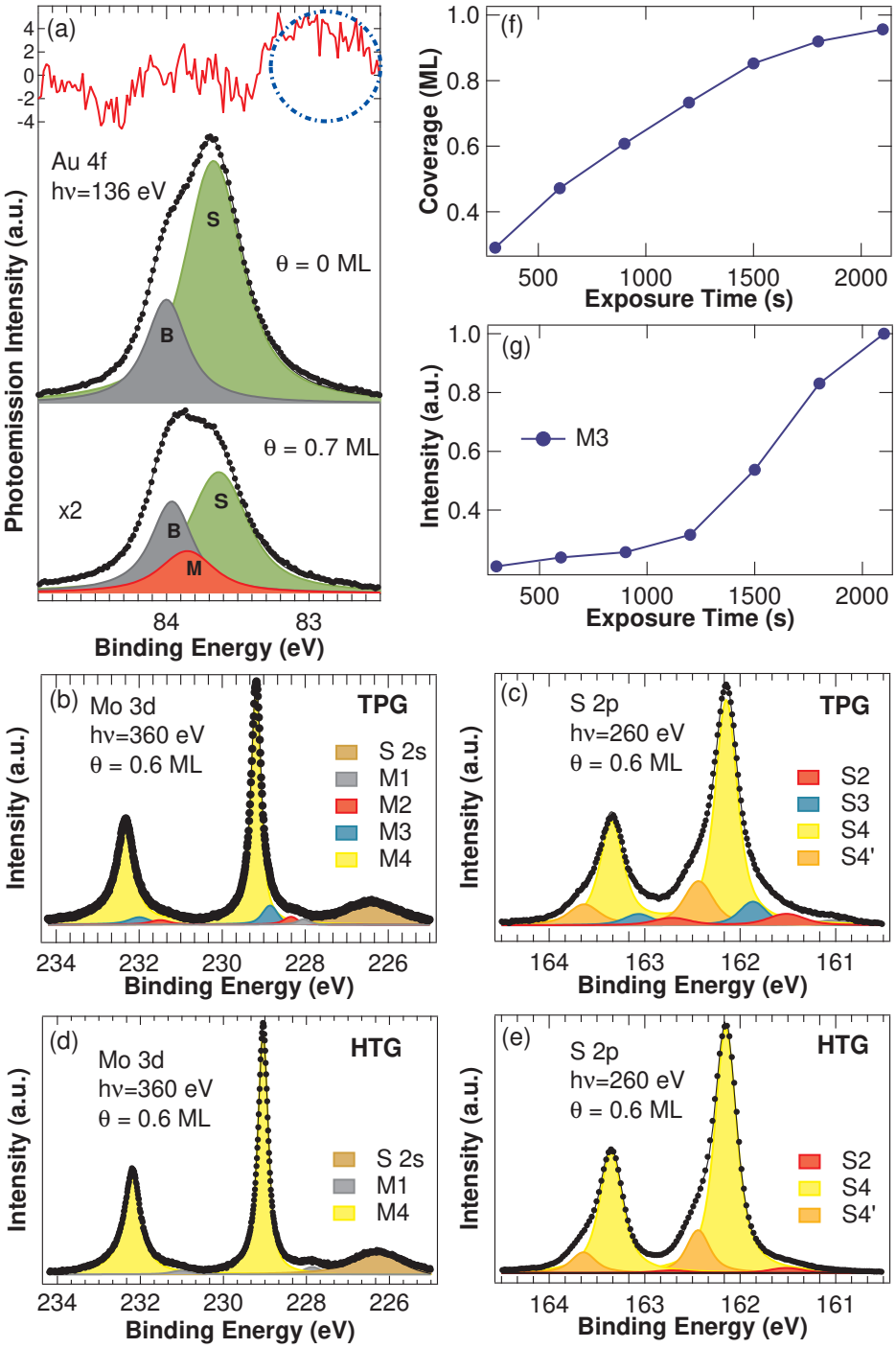

Figure 3.5: (a) Au $4f_{7/2}$ core level XPS spectra of clean Au(111) surface (top) and after MoS_2 growth with coverage of 0.7 ML (bottom) at 136 eV photon energy, together with the fitting residuals (red = 0 ML, black = 0.7 ML). Mo 3d (b) and S 2p (c) core level spectra taken at 360 eV and 260 eV photon energy, respectively, for MoS_2 TPG grown ($\theta \sim 0.6$ ML) sample. Mo 3d (d) and S 2p (e) spectra for MoS_2 HTG grown ($\theta \sim 0.6$ ML) sample. For subsequent TPG doses of 5 minutes each, (f) total coverage of MoS_2 layer calculated from the decrement of the Au $4f_{7/2}$ surface peak and (g) evolution of M3 in the Mo 3d spectra.

studies demonstrate that the MoS_2 growth lifts the native herringbone reconstruction of Au(111)[27], and indeed, when MoS_2 starts to grow on top, the S component decreases; moreover, a new component (M) appears at 83.89 eV. We attribute this extra component to the interaction between unreconstructed Au surface atoms and MoS_2 over layer. Indeed, previous DFT studies demonstrate the existence of an interaction between the two[39, 40].

The Au spectra were used to estimate the coverage. The intensity of the S component is maximum for the clean surface while it goes to zero with 1 ML of MoS_2 on top because of the complete removal of the herringbone reconstruction. Considering that the growth of MoS_2 proceeds via islands formation, enlargement and coalescence[27], the MoS_2 coverage θ_{MoS_2} can be calculated from the intensity of the S component normalized to one for the clean surface, as: θ_{MoS_2}=1-I_S. Figure 3.5 (f) reports the coverage after every cycle of 5 minutes Mo dose in H_2S atmosphere and subsequent annealing.

The Mo 3d spectra in figure 3.5 (b) and (d) after the TPG growth of $\theta \sim 0.6$ ML and HTG growth of $\theta \sim 0.6$ ML MoS_2, shows the 3d spin-orbit splitting of 3.15 eV, consistent with the previous known value[41] and centered at the same BE reported in the literature[29]. From the comparison of the two spectra, one can appreciate the better quality of the MoS_2 layer. As a matter of fact, while in the TPG spectrum the main peak of the MoS_2 basal plane at 229.19 eV is accompanied by different small components at lower BE due to incompletely sulfided species, the HTG spectrum displays only a tiny amount of undesired species. The component at lower binding energy growing at 226.43 eV is the 2s core level of sulfur, colored in brown.

Figure 3.5 (g) reports the intensity of the Mo $3d_{5/2}$ blue component (M3) of the TPG sample as a function of the exposure time. Up to 1200 s, which corresponds to a coverage of ∼0.75 ML, the intensity of this component is low and almost constant, while at higher coverage it starts increasing significantly. This trend is in agreement with what seen by Grønborg et al. through STM measurements: when a coverage higher than 0.8 ML is achieved, not only bilayers, but also amorphous Mo clusters deposited on top of the MoS_2 layer start forming[27].

The S 2p core level spectra for the TPG and HTG grown MoS_2 are reported in figure 3.5 (c) and (e). They show the 2p spin orbit doublet separated by 1.2 eV, in close agreement with values found in literature[42]. Also by the comparison of these two spectra, it is clear that a better result in terms of quality of the sample is achieved by means of the HTG method. However, in both cases the main peak contains two components, S4 and S4'. The latter component can be ascribed to the sulfur that experiences a different environment in the S-Mo-S structure. Indeed, the basal plane S atoms of MoS_2 islands in contact with the Au substrate display a shift of 0.29 eV at higher BE with respect to the topmost S atoms, due to the formation of S-Au bonds[34]. Therefore, we attribute S4 peak centered at 162.15 eV to the topmost S layer and S4' at 162.44 eV to the bottommost S layer.

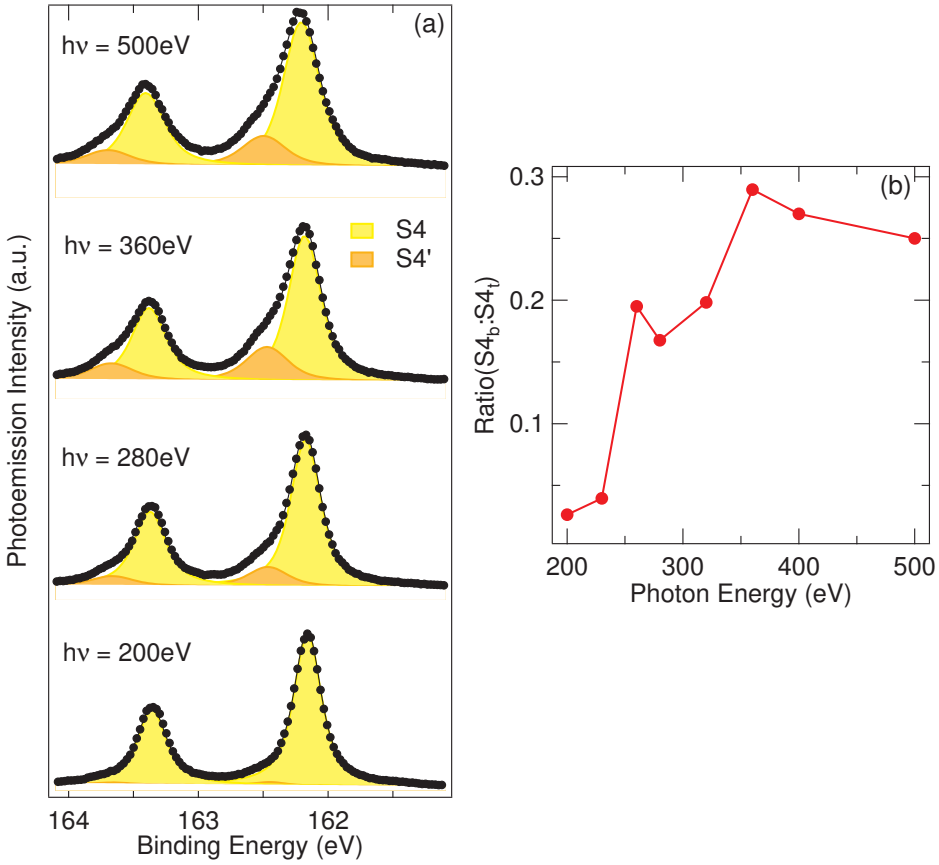

Figure 3.6: (a) Energy scans spectra taken at 0° polar angle (normal emission) on S 2p core level for a HTG MoS_2 dosed sample. (b) Modulation of the ratio between the intensity of S4' and S4 components at different photon energy.

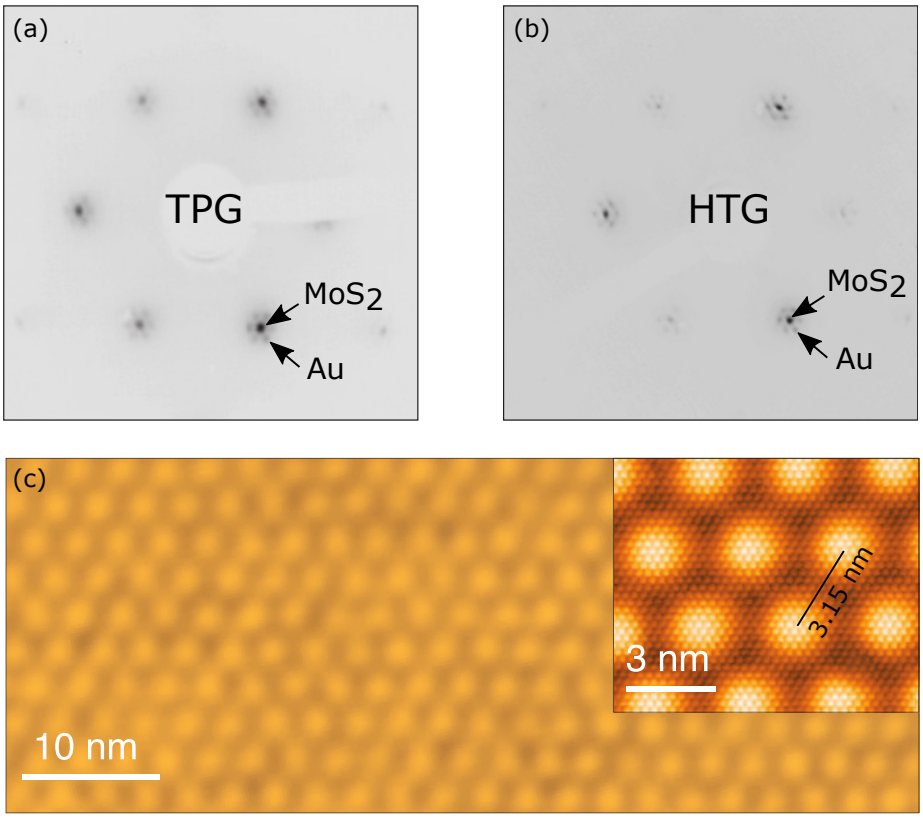

Figure 3.7: LEED patterns (electron kinetic energy E_p =117 eV) for (a) the TPG grown sample (coverage∼0.6 ML) and (b) HTG grown sample (coverage∼0.6 ML). (c) STM topography (tunnelling parameters: $V_B = 0.525$ V, $I_T = 0.54$ nA for the main image. $V_B = 0.525$ V, $I_T = 0.89$ nA for the inset image) showing the large scale moiré structure and the local atomic structure.

In order to experimentally prove this assignment, a photon energy scan was performed on the HTG sample measuring the S 2p core level at normal emission varying the photon energy from 200 eV to 500 eV. The spectra are reported in figure 3.6 (a). When the photon energy increases, the surface sensitivity diminishes because of the larger IMFP of the electrons; as a consequence, also the lower layers are probed. Figure 3.6 (b) shows that, even though the trend is not monotonic because of diffraction effects, the ratio between the two components increase from low to high photon energies, proving the correctness of the assignment.

3.3.4 Study of the structural properties

Figure 3.7 shows the LEED patterns from the TPG and HTG grown MoS_2 samples. The principal spots corresponding to the MoS_2 lattice are sur-

rounded by six sharp satellites arranged in a hexagonal pattern, indicating the formation of a long-range ordered MoS_2 layer. The satellite spots are due to the moiré pattern, because of the lattice mismatch between Au (lattice constant $\alpha_{Au} \sim 0.288\,nm$) and MoS_2 ($\alpha_{MoS_2} \sim 0.315\,nm$). The presence of the moiré satellites spots have been already reported for this system[27] as well as for other 2D systems such as graphene and h-BN on Ir(111)[43, 44] or Ru(0001)[45] or other transition metal surfaces. As the coverage is quite high in both TPG and HTG samples, the spots originated by the Au substrate, marked with an arrow, are faint. From the analysis of the pattern, the comparison between the Au and MoS_2 reciprocal lattice vectors gives the moiré periodicity of 3.2±0.1 nm, in close agreement with the value previously reported in the literature[27]. The absence of additional diffraction features rotated with respect to the Au spots indicates that the MoS_2 unit cell is aligned parallel to the unit cell of the substrate, in agreement with the findings of Sørensen et al., who observed from the 2D fast Fourier transform (FFT) of an STM image a misalignment of 0.45°[29]. By comparing the two LEED patterns, taken after the TPG growth in figure 3.7 (a) and the HTG growth in figure 3.7 (b), it is clear that the two growth procedures lead to two structurally different MoS_2 layers: a careful observation of the LEED spots intensity reveals that the pattern from the TPG grown MoS_2 layer exhibits hexagonally arranged spots with near 6-fold symmetry. On the other hand, the LEED pattern for the HTG grown layer shows a more pronounced three-fold symmetry. As the structure of MoS_2 belongs to the D3h symmetry, and thus has a three-fold symmetry, as clear from figure 1.2 in the first chapter, the LEED pattern of single-layer MoS_2 should have a three-fold symmetry. This is the case of the HTG grown sample pattern, which suggests the presence of only one rotational domain. Differently, the nearly six-fold symmetry of the LEED pattern for the TPG grown sample aims to the coexistence of twin domains on the surface[27].

STM measurements were performed on the HTG grown sample. The STM image reported in figure 3.7 (c) shows an array of bright protrusions, which is the signature of the moiré superstructure, as also reported in other STM measurements[46, 47]. By measuring the distance between the top of two protrusions, we estimated a moiré periodicity of 3.15±0.3 Å, consistent with previous measurements[29] and the LEED analysis. The linescan along the same direction, upon calibration on the Au(111) step, reveals an out-of-plane corrugation of 0.4-0.6 Å, slightly smaller than what seen by Sørensen et al.[29]. However, the values of the out-of-plane corrugation must be in general evaluated with caution, as the STM does not measure the real topography but the local density of states and therefore contributions from electronic and topographic effects are mixed.

The inset in figure 3.7 (c) presents an atomically resolved image of the ad-layer that proves the excellent order of the layer. In this figure, the bright protrusions, induced by the S atoms in the topmost layer, are arranged in

a hexagonal pattern, with a distance of 3.15 Å among them, in agreement with previous findings[29].

One further consideration has to be done: the STM images have been taken in a separate chamber with respect to the one in which the sample was grown, after an annealing at 820 K in UHV. This means that the sample was exposed to air for some time. Nevertheless, the quality of the layer is not compromised, indicating that single layer MoS_2 is chemically inert. Grønborg et al. showed the STM images, essentially identical, of the layer before and after air exposure, proving that this inert character of these samples is a great advantage for their transfer from one experimental setup to another[27].

In order to verify the structural properties of the MoS_2, XPD analyses were performed on both HTG and TPG grown systems. For the experimental data acquisition, in order to enhance the forward scattering from the bottom S atoms, a high photon energy was set to increase the kinetic energy of the photoelectrons, whereas we chose a low photon energy for the Mo and top S to enhance the backward scattering. Specifically, we chose 560 eV (E_k ∼397 eV), 360 eV (E_k ∼130 eV), 270 eV (E_k ∼108 eV) photon energy for bottom S, Mo and top S, respectively. For the analysis, simulated diffraction patterns were calculated using the program EDAC[48]. For these simulations, the underlying Au surface was totally neglected, namely we simulated a freestanding MoS_2, given the lack of a specific local adsorption configuration of MoS_2 on the substrate due to the lattice mismatch with Au(111).

Here we start describing the results on the sample grown through the HTG method. Figure 3.8 (a), (b) and (c) show the stereographic projections of the modulation function χ for the upper (yellow component in the XPS spectrum in figure 3.5 (e)) and lower (orange component in figure 3.5 (e)) S atoms and Mo (yellow component in figure 3.5 (d)), respectively. The experimental data are the colored sector, while the grey scale part is the simulation. In order to quantify the agreement between experiment and simulation, we evaluated the Reliability R-factor, as explained in chapter 2.2. A minimum R-factor of 0.18 for the XPD pattern of Mo 3d was obtained for an Mo-S interplanar distance of 1.62 Å (figure 3.8 (e)) and a lattice parameter of 3.17±0.04 Å (figure 3.8 (f)), in very good agreement with the values reported in literature for MoS_2[49, 50]. These optimized distances were also used to compute the diffraction patterns for S 2p, yielding R-factors of 0.25 and 0.15 for the upper and lower S atoms, respectively. The excellent agreement between experimental data and simulations for the upper and lower S further supports our interpretation for which in the S 2p XPS spectrum, the component at higher binding energy belongs to the bottom S and the component at lower BE to the top S.

However, the higher R-factor for the S4 XPD pattern suggests that also other elements must be taken into account. Indeed, if a contribution from the bottom S layer is added, the R-factor value decreases. In order to analyze quantitatively the contribution from the bottom S layer in the S4 peak, we

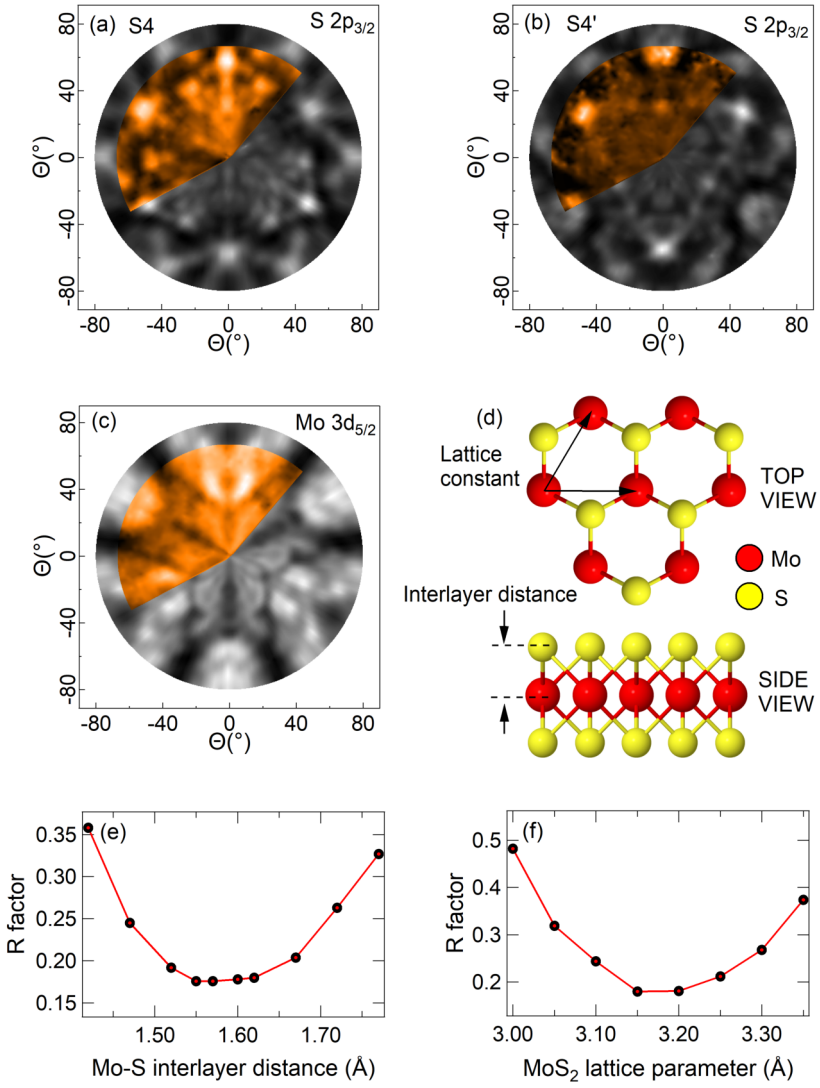

Figure 3.8: Stereographic projections of the integrated photoemission intensity modulation I(θ, ϕ) as a function of emission angle for (a) S4 component 2p (hν = 270 eV; E_k ~108 eV) S4' component 2p (hν = 560 eV; E_k ~397 eV) and (c) Mo 3d (hν = 360 eV; E_k ~130 eV) core levels for the HTG grown sample. The colored sectors are the experimental data, while simulations are shown in grey. (d) MoS_2 geometric structure used to simulate these patterns (Mo: red, S: yellow). (e) R-factor as a function of the Mo-S interlayer distance. (f) R-factor as a function of the MoS_2 lattice parameter.

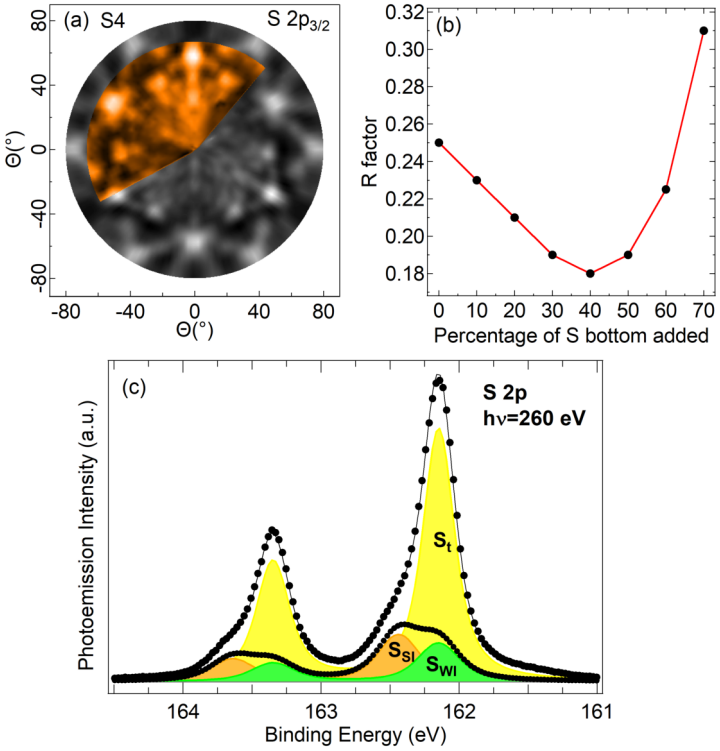

Figure 3.9: (a) Stereographic projection of the integrated photoemission intensity modulation I(θ, ϕ) as a function of emission angle for the S4 component in S 2p core level measured at high kinetic energy (hν=270 eV; E_k ~108 eV), compared with a simulation with 40 percent of emission from the bottom S is added to the simulation. (b) R-factor behavior for the diffraction pattern in (a), as a function of the percentage of S bottom added. (c) S 2p core level spectrum taken at 260 eV photon energy, for MoS_2 HTG grown ($\theta \sim 0.6$ ML) sample, together with the spectral contributions coming from the peak fit analysis and consideration drawn from XPD analysis. S_t is the component relative to the top S layer, S_{SI} is the strongly interacting component of the bottom S layer, corresponding to the S4' component. S_{SI} is the weakly interacting component of the bottom S layer.

added to the top S layer simulations an increasing contribution from the bottom S layer and we evaluated the R-factor. Its trend as a function of the percentage of S atoms of the bottom layer contribution is reported in figure 3.9 (b). From this graph, we obtain the minimum of the R-factor when the experiment is compared with a simulation where 40% of S bottom is added.

From this result we obtain the deconvolution of the S 2p spectrum shown in figure 3.9 (c). The main, more intense peak is the sum of the S_t component, due to the top sulfure atoms and S_{WI}, due to 40% of the bottom S atoms, while the remaining 60% of bottom S generates the component S_{SI}. The splitting of the S 2p of bottom S can be understood considering a similar effect taking place for graphene. Indeed, also the C 1s core level of graphene grown on different transition metal substrates shows peaks centered at different BE depending upon the strength of the interactions between the substrate and the adlayer[51–53]. Therefore, the S_{SI} peak can be assigned to the bottom S atoms strongly interacting with the Au substrate while S_{WI} to the atoms weakly interacting with Au, thus having the same BE of the S_t peak belonging to the topmost S layer.

Coming back to the experimental diffraction patterns reported in figure 3.8, it is clear that they have a three-fold symmetry. Assuming a negligible influence of the underlying Au surface on the symmetry of the pattern, this already excludes the presence of equal areas of twin domains, since these would give rise to a six-fold pattern. In order to clarify this point, figure 3.10 reports the simulated XPD patterns for Mo 3d core level at 130 eV kinetic energy in the case of the domain orientation sketched in figure (a), its mirror orientation (b) and the sum of an equal amount of the two (c). The first two three-fold patterns, once they are summed, result in a six-fold symmetry.

In order to verify quantitatively the presence of one singly oriented domain for the HTG grown sample, we performed multiple scattering simulations of the Mo 3d core level mixing different percentages of the mirror orientation of figure 3.10 (b) to the domain orientation reported in figure 3.10 (a) and we calculated the corresponding R-factor. The behavior of the R-factor in this system is reported in figure 3.11 (b): it shows a minimum when one single orientation is considered and increases monotonically with the increasing percentage of the anti-parallel domain.

The same investigation was done on the TPG grown MoS_2. The XPD measurement of the Mo 3d core level on this system is reported in figure 3.11 (c) together with the evaluation of the R-factor, in figure 3.11 (d). From this last graph, we can state that the TPG method leads to the formation of a ratio ∼3:1 of the orientation obtained with HTG and its mirror orientation. This finding was expected, as it was clear already from the LEED pattern in figure 3.7 (a) that the TPG grown layer is a mixture of two opposite-oriented domains.

To investigate the mutual orientation of the MoS_2 overlayer with respect to the substrate, we measured the Au 4f XPD patterns of the clean sample

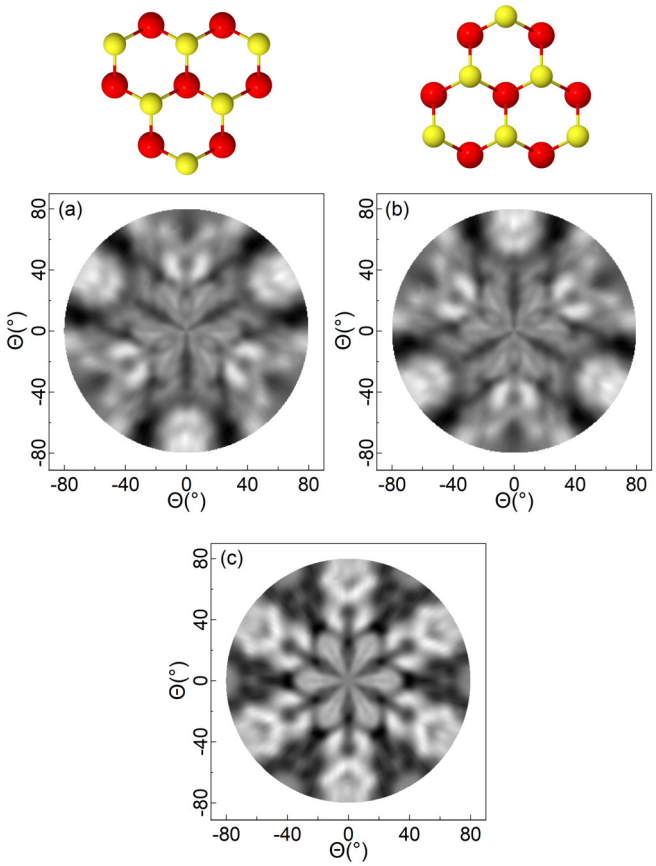

Figure 3.10: Simulated XPD patterns for Mo 3d core level at 130 eV kinetic energy for (a) one domain (oriented as the sketch on top), (b) for the mirror domain and (c) for an equal amount of the two domains.

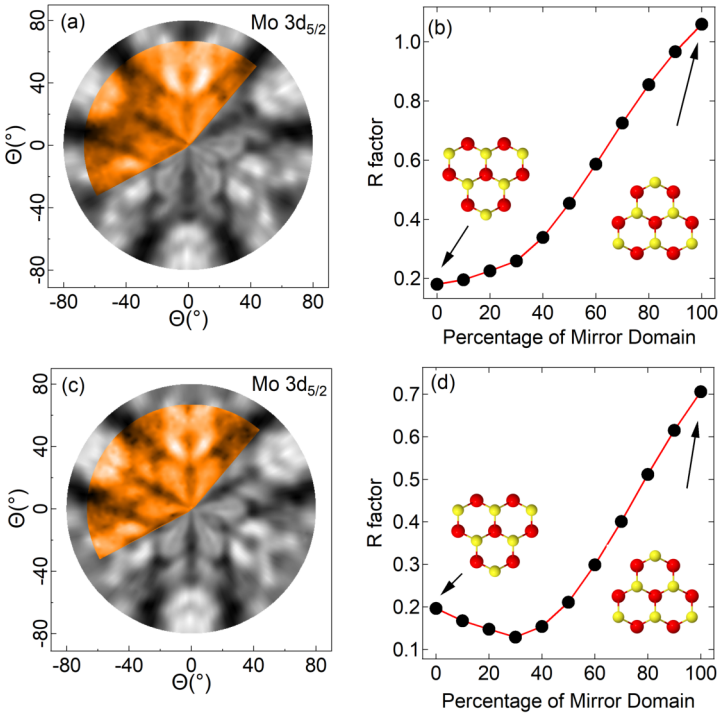

Figure 3.11: Stereographic projections of the integrated photoemission intensity modulation I(θ, ϕ) as a function of emission angle for the Mo 3d core level for the (a) HTG and (c) TPG grown MoS_2 (hν=360 eV; E_k ~130 eV). R-factor behavior for the Mo $3d_{5/2}$ diffraction patters, as a function of the relative concentration of twin domains. (b) The minimum R-factor which defines the correct structure for the HTG grown sample is obtained when one single MoS_2 domain orientation is present, which is the one depicted on the left. (d) In the case of the TPG grown MoS_2, the minimum R-factor is found at 75/25 percent of one orientation and its mirror orientation.

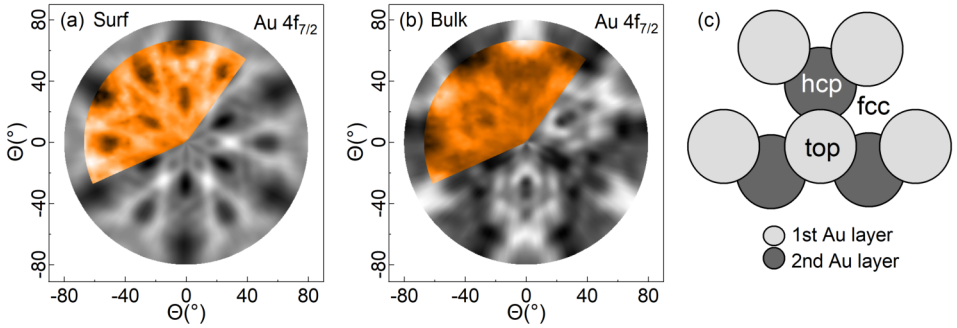

Figure 3.12: Stereographic projections of the integrated photoemission intensity modulation I(θ, ϕ) as a function of emission angle for Au $4f_{7/2}$ (hν=200 eV; E_k ~115 eV) for the surface (a) and bulk (b). The colored sectors are the experimental data, while simulations are shown in grey. (c) Geometric structure used to simulate these patterns.

for surface (figure 3.12 (a)) and bulk (figure 3.12 (b)) components at photon energy of 200 eV (E_k ~115 eV). The surface component shows an almost 6-fold symmetric pattern. The bulk pattern, instead, is 3-fold symmetric. The herringbone reconstruction was simulated as three 60° rotated domains of compressed hexagons, while the gold bulk was simulated with three layers of gold. The very good agreement between the experiments and the simulations, in particular for the bulk peak, allows to define the orientation of the crystal as the one shown in figure 3.12 (c). Theoretical calculations by Bruix et al.[54] showed that the most favorable adsorption site of S of the MoS_2 layer on Au(111) is the top site. Therefore, considering the local arrangement highlighted in figure 3.13, Mo can be present in either the fcc (a) or hcp (b) sites. From the comparison of the XPD patterns of Au and of the MoS_2 above layer, we can state that the mutual orientation of MoS_2/Au(111) in case of the HTG growth is the one in which Mo adsorbs at fcc site, as depicted in figure 3.13 (a).

3.3.5 Study of the electronic structure

The band structure of MoS_2 has already been studied by Miwa et al. on a TPG grown sample[30]. In this section we investigate the electronic structure of the singly orientated MoS_2 monolayer. Figure 3.14(a) shows the dispersion of the MoS_2 valence bands along the Γ-K direction of the Brillouin zone, shown in the inset. Two maxima of the valence band are observed at Γ and K points: the one in Γ is broad, while the second has sharp features. This difference was ascribed to the different interaction with the Au substrate[30] the states near Γ derive from out-of-plane orbitals and therefore an adlayer-substrate interaction can be expected to affect the broadening of the band. On the other hand the states near K derive from in-plane orbitals and as

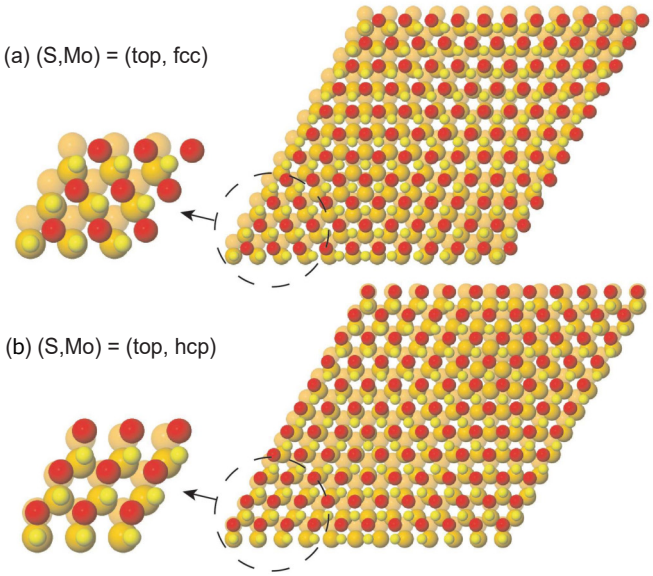

Figure 3.13: Possible 10 x 10/11 x 11 MoS_2/Au(111) configurations with S in on-top position. Insets on the left show the adsorption configuration of bonding regions (a) Mo in fcc and (b) Mo in hcp sites. Ball model color code: yellow: S, orange: Au, red: Mo.

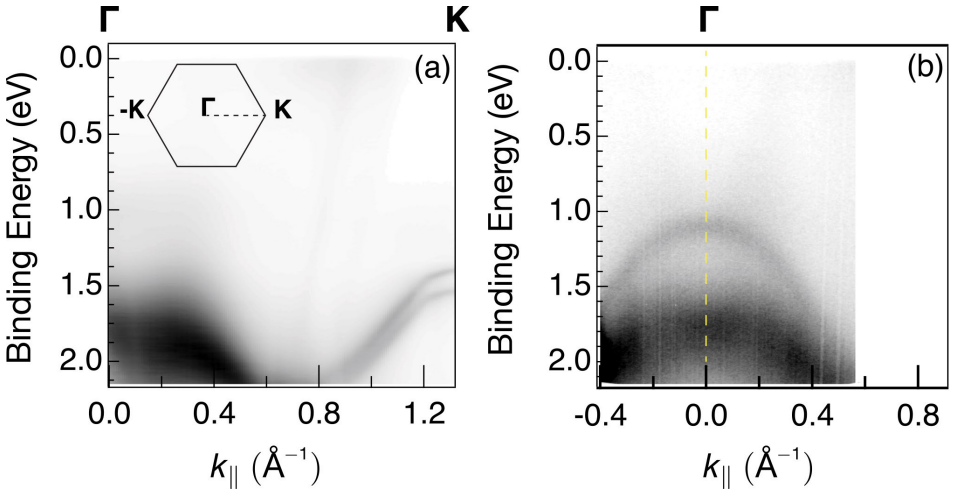

Figure 3.14: (a) Band dispersion along the $\Gamma - K$ direction of MoS_2 Brillouin zone for the HTG grown sample. (b) Band dispersion at Γ for a MoS_2/Au(111) sample with bilayer patches.

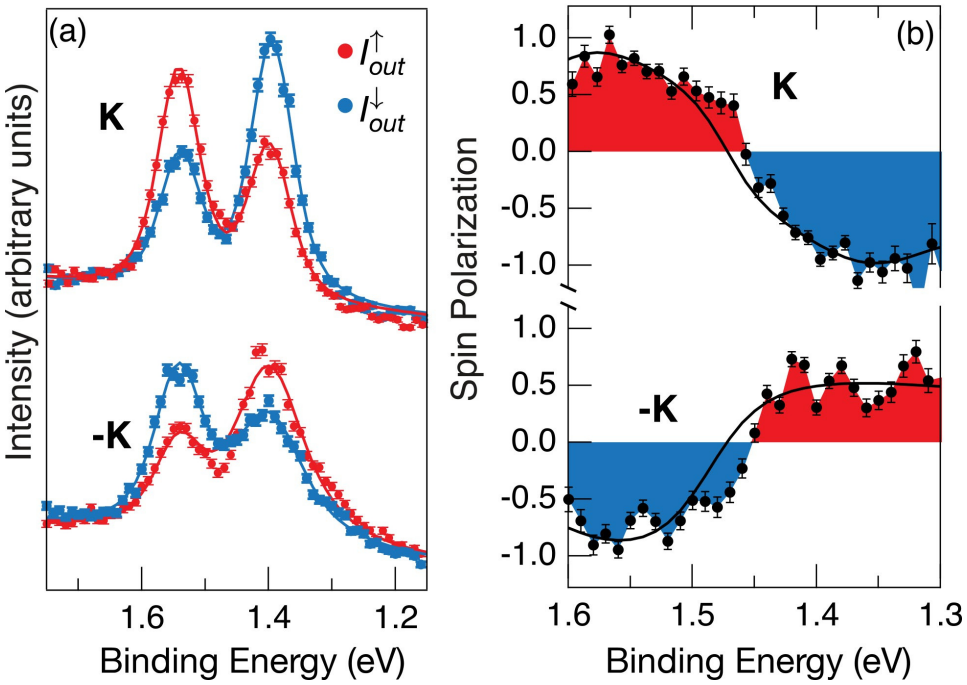

Figure 3.15: (a) Out-of plane spin-resolved energy distribution curves at K and $-K$ points. Red and blue colors mark spin-up and -down signals, respectively. Raw data is shown without a correction for the spin-sensitivity (Sherman function) of the detector. Solid lines are Voight fittings to the experimental data marked with circles. (b) Background-subtracted out-of-plane spin polarization at K and $-K$ points. Solid lines mark the spin polarization calculated from the fits, taking the Sherman function into account. These measurements were performed on the HTG grown sample.

a consequence the interactions between the substrate and the adlayer are predicted to be weak[55]. It is worth noting an interesting feature in figure 3.14 (a) given by the spin-splitting of the states at K, which value (ΔE=145 meV) is in agreement with the theoretical predictions[55]. This splitting has been observed for other TMDCs, like $MoSe_2$ on graphene[56] and WS_2 on Au(111)[35], where a larger larger spin orbit splitting was observed given by the heavy W atoms. Looking at 3.14 (a), together with figure 3.7, one would expect to see the effect of the moiré in the electronic structure, as in the case of the Dirac cones of the epitaxial graphene on Ir(111), where replica bands and minigaps are clearly visible[57]. In this system, instead, such features are absent, suggesting that the moiré does not affect the MoS_2 electronic structure. All these features were already reported in the literature[30, 54] and they do not differ from the data we obtained on the HTG sample, reported in figure 3.14(a). However, the linewidth of the states near K is considerably smaller (51 and 70 meV for the upper and lower band than that measured on the TPG grown samples[30]), indicating a higher quality of the layer. These data also confirm the absence of a second layer, that would result in a second band near Γ at lower BE than the top of the valence band at the k-point, as reported in figure 3.14 (b), that reports the dispersion band at Γ point for a MoS_2/Au(111) sample, where bilayer patches are present[30, 56].

Up to this point, the single orientation character of the layer cannot be appreciated, as all the features described are not affected by the spin-texture of the material. The substantial difference is observed in the spin resolved photoemission measurements[58]. Indeed, singly oriented domains can give rise to a complete spin polarization of the bands near K and $-K$[15, 17]. Figure 3.15(a) reports the data of the out-of-plane spin-resolved energy distribution curves at K and -K points, not yet corrected for the Sherman function, that takes into account the spin-sensitivity of the detector. The spin-up and spin-down signals are colored in red and blue, respectively. Once the Sherman function is taken into account, from the normalized data we find an out-of-plane spin polarization of 86($\pm$14)%, opposite for K and $-K$, shown in figure 3.15 (b). If the sample had been a mixture of two domains, we would have expected to obtain a lower value of spin polarization, because of the mixed contributions from oppositely spin-polarized K and $-K$ valleys, as observed for SL $MoSe_2$ grown on bilayer graphene [59]. Here, on the contrary, we observe a high magnitude of spin polarization which confirms the single-domain structure of MoS_2. Moreover we could state that the weak interaction between MoS_2 and the Au substrate does not affect appreciably the spin polarization.

3.4 Conclusions

In this chapter, using fast-XPS, we studied the dynamics of the growth of MoS_2 layers and showed that pre-sulfided clusters of Mo on Au surface go through various transformations when annealed in H_2S, such as the growth of differently sulfided species visible in both Mo 3d and S 2p spectra. It is evident from the intensity profile that these species are inter-related, acting as precursor to one another and ultimately leading to the growth of 'S-Mo-S' single layer nano-islands when the adequate temperature is reached. We exploited all the information acquired on the formation of MoS_2 to develop a new growth method, called HTG, consisting in dosing molybdenum in H_2S environment directly at high temperature. This allows to have very high quality samples in terms of crystalline order and size of the islands. Nevertheless, the most remarkable advantage of this approach is that it leads to the formation of only one single orientation of MoS_2 domains.

The two growth methods were then studied and compared. By means of XPS on the grown layer, we were able to evaluate the presence of undesired incompletely sulfided species on the sample. Moreover, our results showed evidence of the interaction between the Au surface and the MoS_2 overlayer that leads to the growth of extra component in the Au 4f spectra. We could also differentiate between topmost S and bottommost S components in the S 2p spectra. The unambiguous prove of the assignment of these components was done through XPD analyses, which allowed us also to study the orientation of the MoS_2 domains. These measurements revealed that the HTG method leads to the formation of singly oriented domains. Such feature of the MoS_2 layer is a state-of-the-art achievement and therefore, the HTG grown MoS_2 sample was also studied by means of STM and angular- and spin-ARPES. This last set of measurements proved the complete spin polarization of the states near K and -K of the MoS_2 Brillouin zone, which further demonstrates the presence of singly oriented MoS_2 domains.

References

[1] Mayorov, A. S.; Gorbachev, R. V.; Morozov, S. V.; Britnell, L.; Jalil, R.; Ponomarenko, L. A.; Blake, P.; Novoselov, K. S.; Watanabe, K.; Taniguchi, T.; Geim, A. K. Micrometer-Scale Ballistic Transport in Encapsulated Graphene at Room Temperature. *Nano Letters* **2011**, *11*, 2396–2399.

[2] Nair, R. R.; Blake, P.; Grigorenko, A. N.; Novoselov, K. S.; Booth, T. J.; Stauber, T.; Peres, N. M. R.; Geim, A. K. Fine Structure Constant Defines Visual Transparency of Graphene. *Science* **2008**, *320*, 1308–1308.

[3] Balandin, A. A. Thermal properties of graphene and nanostructured carbon materials. *Nature Materials* **2011**, *10*, 569–581.

[4] Lee, C.; Wei, X.; Kysar, J. W.; Hone, J. Measurement of the Elastic Properties and Intrinsic Strength of Monolayer Graphene. *Science* **2008**, *321*, 385–388.

[5] Chhowalla, M.; Shin, H. S.; Eda, G.; Li, L.-J.; Loh, K. P.; Zhang, H. The chemistry of two-dimensional layered transition metal dichalcogenide nanosheets. *Nature Chemistry* **2013**, *5*, 263–275.

[6] Jena, D. Tunneling Transistors Based on Graphene and 2-D Crystals. *Proceedings of the IEEE* **2013**, *101*, 1585–1602.

[7] Li, M. O.; Esseni, D.; Snider, G.; Jena, D.; Xing, H. G. Single particle transport in two-dimensional heterojunction interlayer tunneling field effect transistor. *Journal of Applied Physics* **2014**, *115*, 074508.

[8] Mak, K. F.; Lee, C.; Hone, J.; Shan, J.; Heinz, T. F. Atomically Thin MoS_2: A New Direct-Gap Semiconductor. *Physical Review Letters* **2010**, *105*, 136805.

[9] Splendiani, A.; Sun, L.; Zhang, Y.; Li, T.; Kim, J.; Chim, C.-Y.; Galli, G.; Wang, F. Emerging Photoluminescence in Monolayer MoS_2. *Nano Letters* **2010**, *10*, 1271–1275.

[10] Wang, Q. H.; Kalantar-Zadeh, K.; Kis, A.; Coleman, J. N.; Strano, M. S. Electronics and optoelectronics of two-dimensional transition metal dichalcogenides. *Nature Nanotechnology* **2012**, *7*, 699–712.

[11] Gibb, A. L.; Alem, N.; Chen, J.-H.; Erickson, K. J.; Ciston, J.; Gautam, A.; Linck, M.; Zettl, A. Atomic Resolution Imaging of Grain Boundary Defects in Monolayer Chemical Vapor Deposition-Grown Hexagonal Boron Nitride. *Journal of the American Chemical Society* **2013**, *135*, 6758–6761.

[12] van der Zande, A. M.; Huang, P. Y.; Chenet, D. A.; Berkelbach, T. C.; You, Y.; Lee, G.-H.; Heinz, T. F.; Reichman, D. R.; Muller, D. A.; Hone, J. C. Grains and grain boundaries in highly crystalline monolayer molybdenum disulphide. *Nature Materials* **2013**, *12*, 554–561.

[13] Najmaei, S.; Liu, Z.; Zhou, W.; Zou, X.; Shi, G.; Lei, S.; Yakobson, B. I.; Idrobo, J.-C.; Ajayan, P. M.; Lou, J. Vapour phase growth and grain boundary structure of molybdenum disulphide atomic layers. *Nature Materials* **2013**, *12*, 754–759.

[14] Yu, Q. et al. Control and characterization of individual grains and grain boundaries in graphene grown by chemical vapour deposition. *Nature Materials* **2011**, *10*, 443–449.

[15] Mak, K. F.; McGill, K. L.; Park, J.; McEuen, P. L. The valley Hall effect in MoS_2 transistors. *Science* **2014**, *344*, 1489–1492.

[16] Xiao, D.; Yao, W.; Niu, Q. Valley-Contrasting Physics in Graphene: Magnetic Moment and Topological Transport. *Physical Review Letters* **2007**, *99*, 236809.

[17] Xiao, D.; Liu, G.-B.; Feng, W.; Xu, X.; Yao, W. Coupled Spin and Valley Physics in Monolayers of MoS_2 and Other Group-VI Dichalcogenides. *Physical Review Letters* **2012**, *108*, 196802.

[18] Gunawan, O.; Shkolnikov, Y. P.; Vakili, K.; Gokmen, T.; De Poortere, E. P.; Shayegan, M. Valley Susceptibility of an Interacting Two-Dimensional Electron System. *Physical Review Letters* **2006**, *97*, 186404.

[19] Cao, T.; Wang, G.; Han, W.; Ye, H.; Zhu, C.; Shi, J.; Niu, Q.; Tan, P.; Wang, E.; Liu, B.; Feng, J. Valley-selective circular dichroism of monolayer molybdenum disulphide. *Nature Communications* **2012**, *3*, 887.

[20] Mak, K. F.; He, K.; Shan, J.; Heinz, T. F. Control of valley polarization in monolayer MoS_2 by optical helicity. *Nature Nanotechnology* **2012**, *7*, 494–498.

[21] Sallen, G.; Bouet, L.; Marie, X.; Wang, G.; Zhu, C. R.; Han, W. P.; Lu, Y.; Tan, P. H.; Amand, T.; Liu, B. L.; Urbaszek, B. Robust optical emission polarization in MoS_2 monolayers through selective valley excitation. *Physical Review B* **2012**, *86*, 081301.

[22] Zeng, H.; Dai, J.; Yao, W.; Xiao, D.; Cui, X. Valley polarization in MoS_2 monolayers by optical pumping. *Nature Nanotechnology* **2012**, *7*, 490–493.

[23] Lee, J.; Mak, K. F.; Shan, J. Electrical control of the valley Hall effect in bilayer MoS_2 transistors. *Nature Nanotechnology* **2016**, *11*, 421–425.

[24] Shi, Y.; Zhou, W.; Lu, A.-Y.; Fang, W.; Lee, Y.-H.; Hsu, A. L.; Kim, S. M.; Kim, K. K.; Yang, H. Y.; Li, L.-J.; Idrobo, J.-C.; Kong, J. van der Waals Epitaxy of MoS_2 Layers Using Graphene As Growth Templates. *Nano Letters* **2012**, *12*, 2784–2791.

[25] Yu, H. et al. Precisely Aligned Monolayer MoS2 Epitaxially Grown on h-BN basal Plane. *Small* **2017**, *13*, 1603005.

[26] Dumcenco, D.; Ovchinnikov, D.; Marinov, K.; Lazić, P.; Gibertini, M.; Marzari, N.; Sanchez, O. L.; Kung, Y.-C.; Krasnozhon, D.; Chen, M.-W.; Bertolazzi, S.; Gillet, P.; i Morral, A. F.; Radenovic, A.; Kis, A. Large-Area Epitaxial Monolayer MoS_2. *ACS Nano* **2015**, *9*, 4611–4620.

[27] Grønborg, S. S.; Ulstrup, S.; Bianchi, M.; Dendzik, M.; Sanders, C. E.; Lauritsen, J. V.; Hofmann, P.; Miwa, J. A. Synthesis of Epitaxial Single-Layer MoS_2 on Au(111). *Langmuir* **2015**, *31*, 9700–9706.

[28] Fu, D. et al. Molecular Beam Epitaxy of Highly Crystalline Monolayer Molybdenum Disulfide on Hexagonal Boron Nitride. *Journal of the American Chemical Society* **2017**, *139*, 9392–9400.

[29] Sørensen, S. G.; Füchtbauer, H. G.; Tuxen, A. K.; Walton, A. S.; Lauritsen, J. V. Structure and Electronic Properties of In Situ Synthesized Single-Layer MoS_2 on a Gold Surface. *ACS Nano* **2014**, *8*, 6788–6796.

[30] Miwa, J. A.; Ulstrup, S.; Sørensen, S. G.; Dendzik, M.; Čabo, A. G. c. v. a. c.; Bianchi, M.; Lauritsen, J. V.; Hofmann, P. Electronic Structure of Epitaxial Single-Layer MoS_2. *Physical Review Letters* **2015**, *114*, 046802.

[31] Jia, J.; Bendounan, A.; Kotresh, H. M. N.; Chaouchi, K.; Sirotti, F.; Sampath, S.; Esaulov, V. A. Selenium Adsorption on Au(111) and Ag(111) Surfaces: Adsorbed Selenium and Selenide Films. *The Journal of Physical Chemistry C* **2013**, *117*, 9835–9842.

[32] Abrami, A. et al. Super ESCA: First beamline operating at ELETTRA. *Review of Scientific Instruments* **1995**, *66*, 1618–1620.

[33] Baker, M.; Gilmore, R.; Lenardi, C.; Gissler, W. {XPS} investigation of preferential sputtering of S from MoS_2 and determination of MoS_x stoichiometry from Mo and S peak positions. *Applied Surface Science* **1999**, *150*, 255–262.

[34] Bruix, A.; Füchtbauer, H. G.; Tuxen, A. K.; Walton, A. S.; Andersen, M.; Porsgaard, S.; Besenbacher, F.; Hammer, B.; Lauritsen, J. V. In Situ Detection of Active Edge Sites in Single-Layer MoS_2 Catalysts. *ACS Nano* **2015**, *9*, 9322–9330.

[35] Dendzik, M.; Michiardi, M.; Sanders, C.; Bianchi, M.; Miwa, J. A.; Grønborg, S. S.; Lauritsen, J. V.; Bruix, A.; Hammer, B.; Hofmann, P. Growth and electronic structure of epitaxial single-layer WS_2 on Au(111). *Physical Review B* **2015**, *92*, 245442.

[36] Klyushin, A. Y.; Rocha, T. C. R.; Havecker, M.; Knop-Gericke, A.; Schlogl, R. A near ambient pressure XPS study of Au oxidation. *Physical Chemistry Chemical Physics* **2014**, *16*, 7881–7886.

[37] Barth, J. V.; Brune, H.; Ertl, G.; Behm, R. J. Scanning tunneling microscopy observations on the reconstructed Au(111) surface: Atomic structure, long-range superstructure, rotational domains, and surface defects. *Physical Review B* **1990**, *42*, 9307–9318.

[38] Narasimhan, S.; Vanderbilt, D. Elastic stress domains and the herringbone reconstruction on Au(111). *Physical Review Letters* **1992**, *69*, 1564–1567.

[39] Bollinger, M. V.; Jacobsen, K. W.; Nørskov, J. K. Atomic and electronic structure of MoS_2 nanoparticles. *Physical Review B* **2003**, *67*, 085410.

[40] Tsai, C.; Abild-Pedersen, F.; Nørskov, J. K. Tuning the MoS_2 Edge-Site Activity for Hydrogen Evolution via Support Interactions. *Nano Letters* **2014**, *14*, 1381–1387.

[41] Castañeda, S. I.; Montero, I.; Ripalda, J. M.; Díaz, N.; Galán, L.; Rueda, F. X-ray photoelectron spectroscopy study of low-temperature molybdenum oxidation process. *Journal of Applied Physics* **1999**, *85*, 8415–8418.

[42] Cavalleri, O.; Gonella, G.; Terreni, S.; Vignolo, M.; Pelori, P.; Floreano, L.; Morgante, A.; Canepa, M.; Rolandi, R. High resolution XPS of the S 2p core level region of the L-cysteine/gold interface. *Journal of Physics: Condensed Matter* **2004**, *16*, S2477.

[43] N'Diaye, A. T.; Coraux, J.; Plasa, T. N.; Busse, C.; Michely, T. Structure of epitaxial graphene on Ir(111). *New Journal of Physics* **2008**, *10*, 043033.

[44] Orlando, F.; Lacovig, P.; Omiciuolo, L.; Apostol, N. G.; Larciprete, R.; Baraldi, A.; Lizzit, S. Epitaxial Growth of a Single-Domain Hexagonal Boron Nitride Monolayer. *ACS Nano* **2014**, *8*, 12063–12070.

[45] Marchini, S.; Günther, S.; Wintterlin, J. Scanning tunneling microscopy of graphene on Ru(0001). *Physical Review B* **2007**, *76*, 075429.

[46] N'Diaye, A. T.; Bleikamp, S.; Feibelman, P. J.; Michely, T. Two-Dimensional Ir Cluster Lattice on a Graphene Moiré on Ir(111). *Physical Review Letters* **2006**, *97*, 215501.

[47] Farwick zum Hagen, F. H. et al. Structure and Growth of Hexagonal Boron Nitride on Ir(111). *ACS Nano* **2016**, *10*, 11012–11026.

[48] García de Abajo, F. J.; Van Hove, M. A.; Fadley, C. S. Multiple scattering of electrons in solids and molecules: A cluster-model approach. *Physical Review B* **2001**, *63*, 075404.

[49] Winer, W. Molybdenum disulfide as a lubricant: A review of the fundamental knowledge. *Wear* **1967**, *10*, 422–452.

[50] Holinski, R.; Gänsheimer, J. A study of the lubricating mechanism of molybdenum disulfide. *Wear* **1972**, *19*, 329–342.

[51] Alfè, D.; Pozzo, M.; Miniussi, E.; Günther, S.; Lacovig, P.; Lizzit, S.; Larciprete, R.; Burgos, B. S.; Menteş, T. O.; Locatelli, A.; Baraldi, A. Fine tuning of graphene-metal adhesion by surface alloying. *Scientific Reports* **2013**, *3*, 2430–2436.

[52] Miniussi, E.; Pozzo, M.; Baraldi, A.; Vesselli, E.; Zhan, R. R.; Comelli, G.; Menteş, T. O.; Niño, M. A.; Locatelli, A.; Lizzit, S.; Alfè, D. Thermal stability of corrugated epitaxial graphene grown on Re(0001). *Physical Review Letters* **2011**, *106*, 216101.

[53] Preobrajenski, A. B.; Ng, M. L.; Vinogradov, A. S.; Mårtensson, N. Controlling graphene corrugation on lattice-mismatched substrates. *Physical Review B* **2008**, *78*, 073401.

[54] Bruix, A.; Miwa, J. A.; Hauptmann, N.; Wegner, D.; Ulstrup, S.; Grønborg, S. S.; Sanders, C. E.; Dendzik, M.; Grubišić Čabo, A.; Bianchi, M.; Lauritsen, J. V.; Khajetoorians, A. A.; Hammer, B.; Hofmann, P. Single-layer MoS_2 on Au(111): band gap renormalization and substrate interaction. *ArXiv e-prints* **2016**,

[55] Zhu, Z. Y.; Cheng, Y. C.; Schwingenschlögl, U. Giant spin-orbit-induced spin splitting in two-dimensional transition-metal dichalcogenide semiconductors. *Physical Review B* **2011**, *84*, 153402.

[56] Zhang, Y. et al. Direct observation of the transition from indirect to direct bandgap in atomically thin epitaxial $MoSe_2$. *Nature Nanotechnology* **2014**, *9*, 111.

[57] Pletikosić, I.; Kralj, M.; Pervan, P.; Brako, R.; Coraux, J.; N'Diaye, A. T.; Busse, C.; Michely, T. Dirac Cones and Minigaps for Graphene on Ir(111). *Physical Review Letters* **2009**, *102*, 056808.

[58] Bigi, C.; Fujii, J.; Vobornik, I.; Das, P. K.; Benedetti, D.; Salvador, F.; Panaccione, G.; Rossi, G. Very Efficient Spin Polarization Analysis (VESPA): New Exchange Scattering-based Setup for Spin-resolved ARPES at APE-NFFA Beamline at Elettra. *ArXiv e-prints* **2016**,

[59] Mo, S.-K.; Hwang, C.; Zhang, Y.; Fanciulli, M.; Muff, S.; Hugo Dil, J.; Shen, Z.-X.; Hussain, Z. Spin-resolved photoemission study of epitaxially grown $MoSe_2$ and WSe_2 thin films. *Journal of Physics Condensed Matter* **2016**, *28*.

Chapter 4

Growth and characterization of single-layer MoS_2 on Ag(111) and Ag(110)

4.1 Introduction

As already mentioned in previous chapters (see chapter 1 and 3), TMDCs, and in particular MoS_2, are attractive for various applications and among them one of the most promising is related to future generation of electronic devices based on such materials. Regardless of the working principle (traditional field effect transistors (FETs), tunnel FETs, opto-electronic FETs), one important aspect for the real application is related to the intrinsic contact resistance of such devices, meaning the resistance between the active part of the transistor and the contacts that interface it with external components. In fact, the geometrical scaling of FETs up to the nanoscale regime demands a reduction of the supply voltage due to constraints on the dissipated power while keeping the on-state-current as high as possible for performance purposes. In this framework, it becomes clear that the contact resistance acts as a performance-limiting factor and many studies have been performed to tackle this issue[1–4]. In this context, among the different solutions to reduce the contact resistance in MoS_2 based devices, one is to induce a local change of the MoS_2 crystal structure, promoting the transition from semiconductor (trigonal prismatic, 1H, phase) to metal (octhaedral, 1T, phase)[5–7]. Another way to obtain the reduction of contact resistance between the metal contacts and the MoS_2 is to reduce the Schottky barrier height (SBH)[8–10], which depends on the metal work function and the number of MoS_2 layers[11]. Finally, it is worth highlighting that theoretical calculations predict a MoS_2 semiconductor-to-metal transition by a simple interaction with the substrate[1, 10, 12]. In the first section of the chapter, we investigate the growth of MoS_2 on Ag(111) substrate, which was chosen based upon

theoretical calculations and experimental evidences. In fact, Zhong et al. predict a Schottky barrier of 0.212 eV for the MoS_2/Ag(111) system, much smaller than the value of 0.763 for MoS_2 on Au(111)[11], and Dendzik et al. demonstrate that a semiconductor-to-metal transition occurs to WS_2 grown on Ag(111)[13]. Moreover, for the structural point of view, theoretical calculations predict a weak interaction between the Ag substrate and the MoS_2 layer, slightly stronger than for Au(111), which should allow to produce extended ordered nearly free-standing MoS_2 layers[11, 12].

In the second part of the chapter, instead, we study the growth of MoS_2 on Ag(110), a substrate with unequal lattice parameters along the different crystallographic directions. The aim of this choice was to investigate whether the rectangular lattice as opposed to the hexagonal lattice of MoS_2 modifies the structural properties of the layer. Moreover, it is possible that the moiré superstructure, due to the lattice mismatch between MoS_2 and the substrate, introducing an additional periodic potential, affects the electronic properties of MoS_2, as it was demonstrated for 2D h-BN and graphene grown on anisotropic substrates[14–16]. This last aspect is among the most critical in order to include this material in already existing technology and to develop future applications.

We here demonstrate that highly ordered MoS_2 monolayer can be grown on both Ag(111) and Ag(110) using the HTG method already described in chapter 3 for the MoS_2 on Au(111), providing new insight into the strategies for producing high quality MoS_2 monolayer.

4.2 Experimental details

The Ag(111) and Ag(110) substrates were prepared by repeated cycles of Ar^+ sputtering, and annealing to 1060 K and 800 K, respectively, for 10 minutes at 1 Ks^{-1} heating and cooling rate. The sample quality was checked with XPS for Ag $3d_{5/2}$ core level and with LEED measurements, showing an hexagonal (1x1) pattern for Ag(111) and a (1x1) pattern reflecting the rectangular cell of the Ag(110) substrate. The growth of MoS_2 on Ag(111) was performed by dosing atomic Mo at a rate of 0.0095 monolayer per minute in a background pressure of 2 x 10^{-6} mbar of H_2S onto a clean substrate kept at 823 K. The growth of MoS_2 on Ag(110) was performed using the TPG method up to the coverage of 0.07 ML of MoS_2, dosing Mo on the clean Ag(110) surface at RT and subsequently annealing the sample at 800 K, both in H_2S background pressure of 5 x 10^{-7} mbar. The growth was continued by means of the HTG method, dosing atomic Mo at a rate of 0.0047 ML/minute in a background pressure of 5 x 10^{-7} mbar of H_2S onto the substrate kept at 800 K. During the growth, fast-XPS was performed, looking simultaneously at the changes of Mo 3d and S 2p core levels with 260 eV photon energy[17]. After the growth, the S 2p, Mo 3d and Ag 3d core

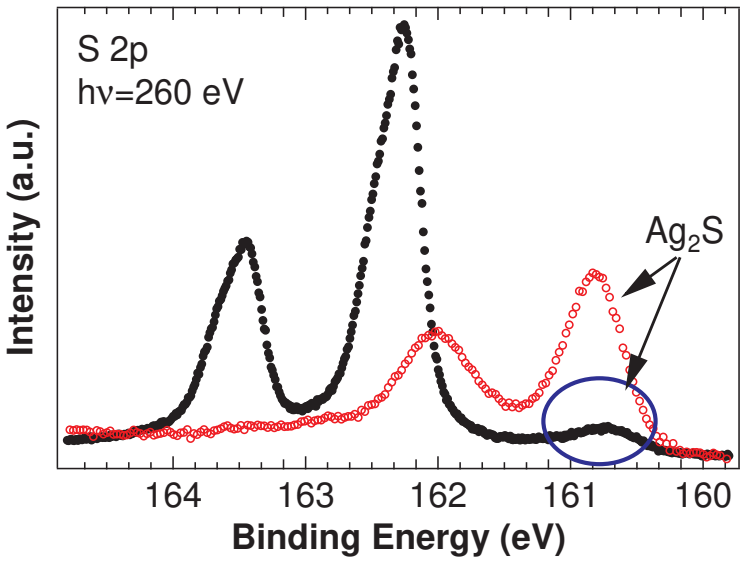

Figure 4.1: S 2p core level spectra measured at hν=260 eV. Red curve: MoS_2 on Ag(111) with the presence of an extra peak due to the presence of Ag_2S. Black curve: H_2S dose on Ag(111).

level spectra were measured using photon energies of 260, 360 and 480 eV respectively. The XPD patterns for the S 2p were acquired at $h\nu = 270$ eV (E_k ~108 eV) for the top S layer, and at $h\nu = 560$ eV (E_k ~397 eV) for the bottom S layer. The XPD measurements for Mo 3d were performed with photon energy $h\nu$=360 eV corresponding to electron kinetic energies of 130 eV.

For a more complete description of the experimental parameters, see chapter 2.10

4.3 Results and discussion

4.3.1 Growth and characterization of MoS_2 on Ag(111)

According to the synthesis of MoS_2 on Au(111) reported in chapter 3, it has been found that the high temperature growth (HTG) allows to obtain better quality layers. For this reason, the same approach has been used for the MoS_2 synthesis on Ag(111). In this case, however, one detail must be stressed: unlike the Au surface, which is quite inert towards the reaction with H_2S, the Ag(111) surface can dissociate H_2S and it is known that S can react with silver to give Ag_2S[18], with a characteristic S 2p peak at 160.7 eV BE[19]. In this regard, figure 4.1 aims at showing the formation of such compound when H_2S is dosed at a pressure of $1x10^{-6}$ mbar on the Ag

substrate at 773K (red line), where a peak at 160.7 eV BE is clearly visible. Moreover, the same image shows also the spectrum of a MoS_2 growth using a too high H_2S pressure (black line); aside from the two main peaks that will be discussed later, a peak at 160.7 eV BE appears. This latter component decreases if the H_2S pressure is lowered while dosing Mo to form MoS_2 (not shown), and therefore Ag_2S acts as a reversible sulfur reservoir. Since we carefully avoided the formation of Ag_2S, in order not to load and saturate the surface with species that would have demoted the formation of MoS_2, the growth was monitored and the H_2S pressure was decreased if the Ag_2S component raised.

Molybdenum was evaporated on the Ag(111) substrate at 823 K in a background H_2S pressure of $2x10^{-6}$ mbar. This substrate temperature, 50 K lower than on Au(111), after several trials, was found to be the most appropriate for the formation of MoS_2 on this substrate. The growth was followed by fast-XPS, checking simultaneously the Mo 3d and S 2p core levels. The spectra were fitted with the parameters similar to the ones used for the HR spectra, that will be shortly described.

Figure 4.2 (a) reports the photoemission intensity of the Mo 3d component of the MoS_2 basal plane as a function of the dose time. The curve shows a linear trend up to about 30 minutes from the start of the growth, then the growth rate starts to decline. The dose was stopped after 105 minutes, as the components at lower BE than that of the basal plane of MoS_2 started to increase significantly.

After the growth, we measured the HR-XPS spectra of Ag 3d, Mo 3d and S 2p core levels at room temperature. The fitting parameters for Mo 3d and S 2p and the binding energies referred to the Fermi level of the Ag substrate are reported in table 4.1.

Table 4.1: Doniach-Šunjić line shape parameters for the different components of the Au $4f_{7/2}$, Mo 3d and S 2p core levels acquired at room temperature at 360 eV and 260 eV photon energy, respectively. L is the Lorentzian width, α is the asymmetry parameter and G is the Gaussian width (see section 2.1.2 for detailed information). BE is the binding energy.

Mo 3d (hv=360eV)	L(eV)	α	G(eV)	BE(eV)
$3d_{5/2}$	0.18	0.10	0.25	229.33
$3d_{3/2}$	0.40	0.10	0.25	232.48
S 2p (hv=260eV)	L(eV)	α	G(eV)	BE(eV)
$2p_{3/2}$ top	0.16	0.05	0.19	162.25
$2p_{1/2}$ top	0.17	0.05	0.19	163.45
$2p_{3/2}$ bottom	0.16	0.05	0.19	162.49
$2p_{1/2}$ bottom	0.17	0.05	0.19	163.69

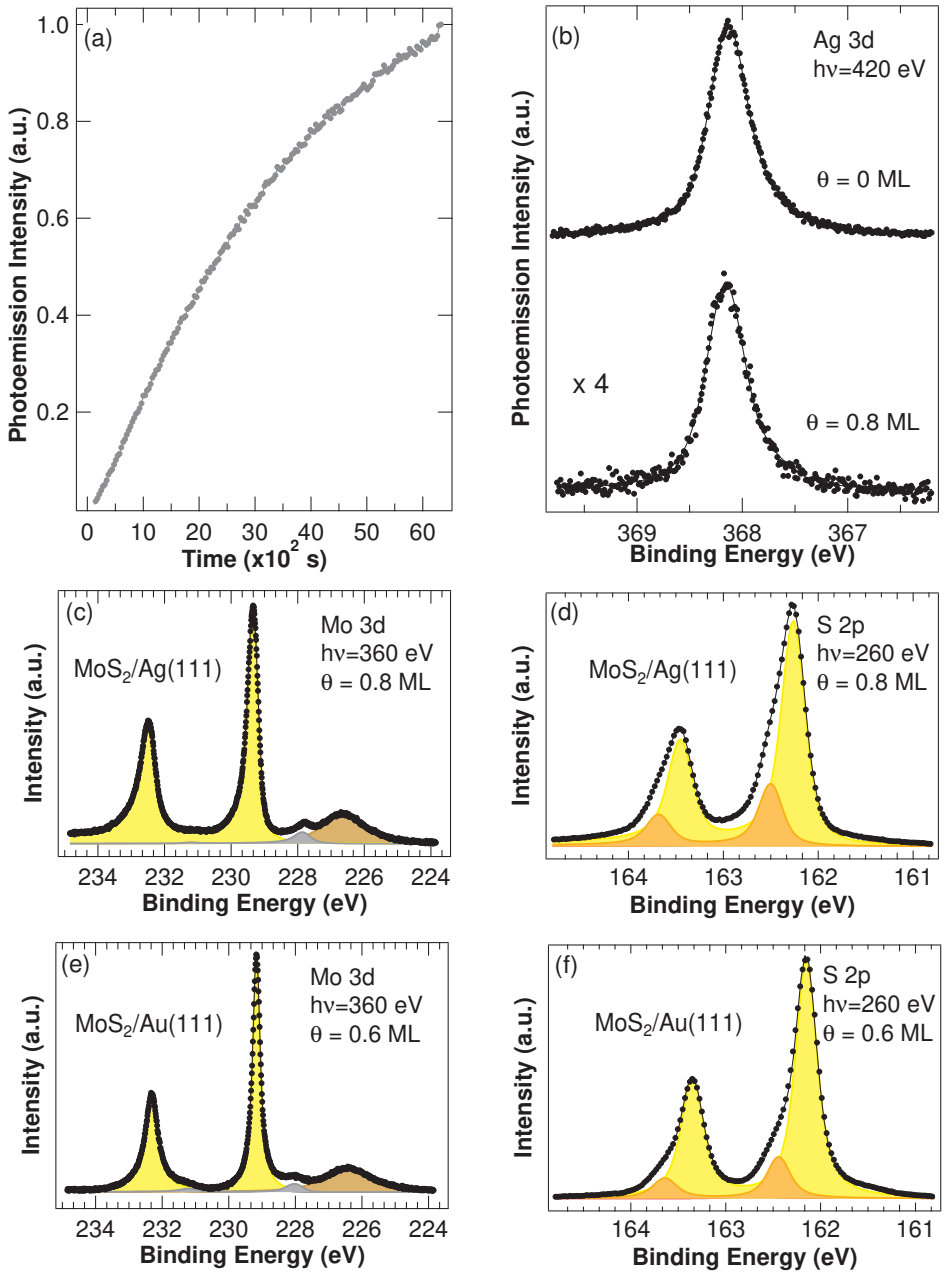

Figure 4.2: (a) Photoemission intensity of the MoS_2 basal plane Mo 3d component as a function of the dose time. (b) Ag $3d_{5/2}$ core level XPS spectra of clean Ag(111) surface (top) and after MoS_2 growth with coverage of θ ~0.8 ML (bottom) at hν=420 eV photon energy. Mo 3d (c) and S 2p (d) core level spectra taken at hν=360 eV and hν=260 eV photon energy respectively, for MoS_2 grown on Ag(111)($\theta \sim 0.8$ ML). Mo 3d (e) and S 2p (f) core level spectra taken at hν=360 eV and hν=260 eV photon energy respectively, for MoS_2 grown on Au(111) ($\theta \sim 0.6$ ML), described in Chapter 3. All the experimental spectra (data points) are presented with the resulting fit (line) and together with the spectral contributions resulting from peak fit analysis (solid areas).

Figure 4.2 (b) reports the Ag $3d_{5/2}$ spectra for the clean Ag(111) surface and for MoS_2 coverage of θ ∼0.8 ML, magnified four times. With increasing coverage, the intensity of the peak decreases by effect of the MoS_2 screening, but the shape of the peak is unchanged. In previous studies, it was proved that, differently from Au, in which the SCLS is appreciable, the SCLS of Ag(111) is less than 100 meV, a too small value to distinguish between the bulk and surface components in the Ag spectrum[20]. Therefore, unlike the MoS_2 on Au(111) system, we do not find any fingerprint of the interaction between MoS_2 and the silver substrate, i.e. any new component related to the Ag atoms that feel the presence of the adlayer can be revealed. However, despite these difficulties, the Ag 3d spectra have been used to estimate the coverage in a slightly different way if compared with the MoS_2 on Au(111) case discussed in chapter 3. In particular, we compare the overall intensity of the Au 4f and Ag 3d peaks to infer about the MoS_2 coverage of the MoS_2 on Ag(111) system. In order to do so, the Ag 3d spectra were measured at 420 eV photon energy to have the same photoelectron kinetic energy, ∼52 eV, of the Au 4f spectra measured at 136 eV photon energy for the MoS_2/Au(111) system. This allows us to assume that the IMFP of the photoelectrons and the attenuation of the signal given by the MoS_2 overlayer are the same for the two systems. Therefore, it seems reasonable to assume that the peak intensity of Ag 3d decreases as the one of Au 4f with the MoS_2 coverage. As the coverage of MoS_2 on Au(111) was accurately estimated (see chapter 3 on MoS_2/Au(111) system), by measuring the reduction of the Au surface component, we evaluated the decrease of the overall Au 4f peak intensity, we correlated this to the estimated coverage, and finally to the decrease of the Ag 3d peak. From this calculation, the coverage of MoS_2 on Ag(111) is assessed at θ ∼0.8 ML, where a monolayer, from here on, is defined as one complete layer of MoS_2.

The Mo 3d spectrum in figure 4.2 (c) after the growth of $\theta \sim 0.8$ ML shows a 3d spin-orbit splitting of 3.15 eV, consistent with the previous known value[21]. This spectrum is fitted with only one component for the main peak, i.e. the one centered at 229.33 eV binding energy, position similar to the one observed for the basal plane component for MoS_2 monolayer on Au(111) at 229.19 eV BE[22, 23]. Therefore, we attribute this component to the basal plane of MoS_2. One extra component, colored in grey, is added at 227.9 eV. This one cannot be related to metallic Mo species, as from preliminary experiments (not shown) we see that the Mo $3d_{5/2}$ of metallic Mo species on Ag(111) is centered at 227.6 eV BE. However, we can tentatively attribute the grey component to not completely sulfided species. Indeed, though there are no studies about non-stoichiometric MoS_{2-x} ($0 \leq x \leq 1$) species on Ag(111), it is known that these species on Au(111) have core level peaks centered at lower BE than the MoS_2 basal plane component[24]. Finally, the brown component at lower binding energy growing at 226.65 eV is the S 2s core level.

The S 2p spectrum for the same sample is reported in figure 4.2 (d). It shows a spin orbit doublet separated by 1.19 eV in close agreement with values found in literature[25]. The spin orbit doublet is fitted with two components, similarly to the case of MoS_2 on Au(111): an intense peak colored in yellow centered at 162.25 eV and a smaller orange component with a shift of 239 meV to higher BE with respect to the previous one. In chapter 3, we demonstrated that, because of the different interaction with the substrate, the bottom S layer results in two spectral components, one weakly interacting centered at the same BE of the top S layer, and one belonging to the strongly interacting S at higher BE. Therefore, we attribute the component at higher BE (orange) to the strongly interacting bottom S atoms, while the component at lower BE (yellow) to the weakly interacting bottom S atoms plus the S atoms of the top layer.

Figure 4.2 (e) and (f) report the HR-spectra of Mo 3d and S 2p for the MoS_2 grown on Au(111) (see chapter 3) in order to make a comparison with MoS_2 on Ag(111). A common feature for both core level spectra is a shift of all the components towards higher BE in the case of MoS_2 on Ag(111) with respect to that on Au(111). In particular, the Mo 3d peaks are shifted by 140 meV, while those of S 2p by 100 meV. A similar behavior has been seen by Dendzik et al. while comparing WS_2 grown on Ag(111) and on Au(111)[13]. They observed a shift of 207 meV towards higher BE of the W 4f components on Ag(111) with respect to the WS_2 grown on Au(111), explaining this fact by taking into account the different work functions of Au(111) and Ag(111). This leads to a different Fermi level pinning, hence a shift of the valence states which is reflected also in the core levels[13]. As WS_2 and MoS_2 show similar features, i.e. they have similar structural parameters, they are both semiconductors with a comparable bandgap and a similar electronic structure[26], we believe that these considerations can be applied also for MoS_2/Ag(111).

In reference [27], Dendzik et al., by means of ARPES measurements, demonstrate that WS_2 grown on Ag(111) shows a metallic behavior, as metallic states are present near the Fermi level because of the hybridization of WS_2 with the Ag states. On the same system, W 4f core level measurements were performed and the spectra were fitted using a Doniach-Šunjić line shape with an asymmetry parameter of 0.1, in order to properly fit the tail of the W 4f component at higher BE. This value further proves the metallic behavior of WS_2, indeed, in general metallic systems show an asymmetric behavior, due to electron-hole pair excitations at the Fermi level, that must be fitted with a non-zero asymmetry parameter[28]. By looking carefully at the Mo 3d spectra of our system MoS_2/Ag(111), one notices that the main component has also a high binding energy tail. As this tail cannot be fitted with an additional peak, the only feasible way is to increase the asymmetry parameter in the fit to 0.1, while in the case of MoS_2 on Au(111) this value is close to 0. Therefore, though ARPES measurements on our system have not been

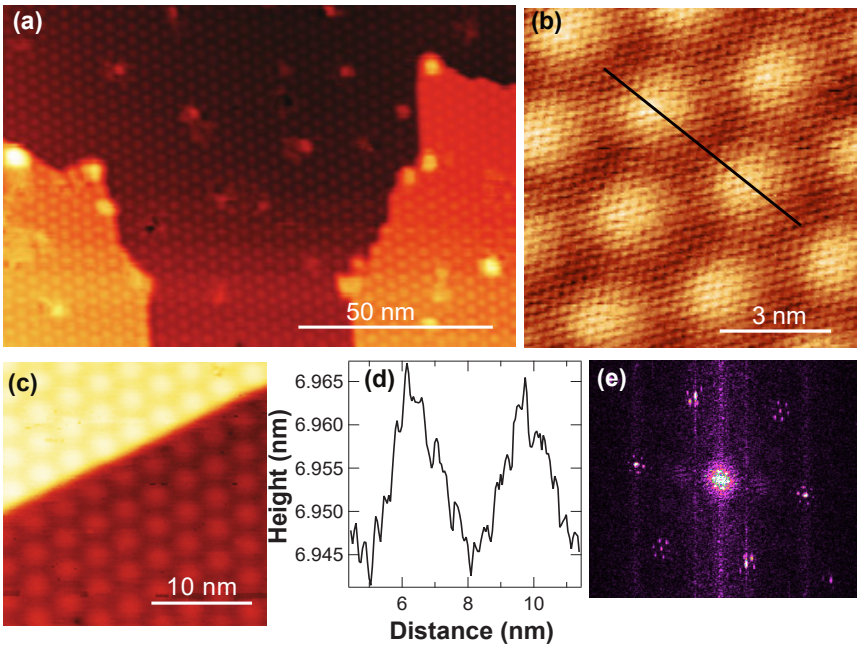

Figure 4.3: STM images showing MoS_2 extended layer at coverage $\theta \sim 0.8$ ML. (a) 130 x 80 nm large scale image shows a continuous MoS_2 carpet on different terraces(V_B=1.051 V, I_t=0.88 nA). (b) 7 x 7 nm atomically resolved STM image of the MoS_2 lattice and moiré superstructure of MoS_2/Ag(111) (V_B=39 mV, I_t=2.44 nA). (c) 20 x 20 nm size image shows the MoS_2 carpet climbing over an Ag terrace (V_B=221 mV, I_t=1.27 nA). (d) Line profile along the black line drawn in figure (a). (e) FFT of the STM image reported in figure (a).

performed yet, in analogy with the findings reported in reference [27], we believe that MoS_2 on Ag(111) has a metallic behavior.

The evidence of a stronger interaction between adlayer and substrate emerges from the S 2p core levels spectra. Indeed, the bottom S component (the orange component at higher BE) in the case of MoS_2 on Ag(111) in figure 4.2 (d) is more intense than that of MoS_2 on Au(111). This feature is ascribed to the larger number of S atoms belonging to the bottom layer interacting with the Ag substrate.

In figure 4.3 three STM images taken on the $\theta \sim$0.8 ML MoS_2/Ag(111) sample are reported. The presence of arrays of bright protrusions, visible in figure 4.3 (a) and (c), and magnified in figure 4.3 (b), is attributed to the presence of the moiré superstructure, as discussed in the previous chapters for MoS_2/Au(111) and in the following for WS_2/Au(111) systems. By measuring

the in-plane distance between two protrusions, along the black line reported in figure 4.3 (b), we obtain a periodicity of 3.48±0.03 nm, as reported in figure 4.3 (d), in agreement with the LEED findings. Moreover, from the line profile along the same cut, we find an out-of-plane corrugation of 0.2 Å.

Figure 4.3 (a) presents a large scale (130x80 nm) STM image that proves the long range order of the MoS_2 carpet grown on the silver substrate. Here, one can notice one dark and two bright regions, which are due to the different terraces of the silver substrate and not to the presence of MoS_2 bilayer, because the height of the step of 2.3 Å is in agreement with the one of the calculated interlayer distance between two planes of Ag(111) of 2.35 Å. As one cannot appreciate the presence of single MoS_2 islands but a continuous layer due to their coalescence, this image confirms the high coverage calculated from the XPS spectra. In figure 4.3 (b), reporting an atomically resolved STM image, in addition to the large bright protrusions of the moiré superstructure, one can clearly distinguish other arrays of spots. These are induced by the S atoms in the topmost layer that are arranged in a hexagonal pattern, with a measured distance of 3.14±0.4 Å among them. This value is consistent with the lattice parameter of a free MoS_2(0001) plane[29, 30]. By zooming on a step edge of a Ag substrate (figure 4.3 (c)), it is possible to see that the MoS_2 carpet is continuous while crossing the terraces, as the moiré protrusions do not disappear but they continue on the other side, from the dark to the bright region of the image, though they do not proceed alligned but they suffer a shift. We can affirm that is not the case of two islands that merged forming a grain boundary, but the crossing layer, because this behavior was already observed on the graphene/Ir(111) system by Coreaux et al. Indeed, through an atomically resolved STM image on an edge of Ir, they demonstrate the structural coherency of the graphene while crossing the step[31].

Finally, figure 4.3 (e) reports the Fast Fourier Transform (FFT) of the image shown in figure 4.3 (a). The bright spots in the reciprocal space are well defined and arranged in an hexagonal pattern, as expected from the hexagonal arrangement of the sulfur atoms in the top layer of MoS_2. Each main spot is surrounded by six satellites, due to the moiré superstructure. This pattern shows identical features to the ones present in LEED that are shown here below. It is worth noting that the LEED pattern accounts for a much larger region, while the FFT of the STM image is relative to a small region, therefore this equivalence in the patterns suggests that all the sample shows a morphology similar to that reported in figure 4.3 (b).

One further consideration has to be done: the STM images have been taken in a separate chamber with respect to the one in which the sample was grown, after an annealing in UHV. This means that the layer was exposed to air at room temperature for some time. Even though figure 4.3 (b) shows disordered spots that are ascribable to contaminants that adsorbed on the surface during air exposure and that were not removed by the thermal annealing, from the STM images the quality of the layer is not compromised,

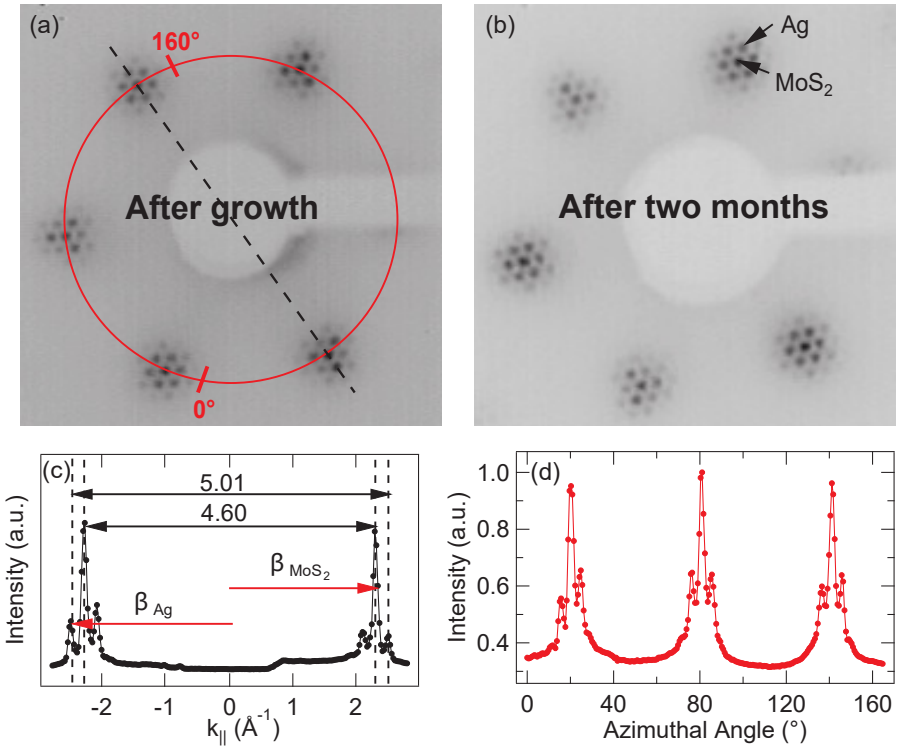

Figure 4.4: LEED patterns of θ ~0.8 ML MoS_2 grown on Ag(111) at E_k=189 eV electron energy taken (a) immediately after the growth and (b) after two months, during which the sample was exposed to air. (c) Cut of the line profile along the dashed line shown in figure (a). (d) line profile analysis along the red ring containing the MoS_2 spots in figure (d) Line profile analysis along the red ring drawn in figure (a), containing the MoS_2 spots.

indicating that single layer MoS_2 grown on Ag(111) is chemically inert. This is also proved by LEED measurements taken at 189 eV electron energy at room temperature, immediately after the growth and after two months in which the sample was kept in air (reported in figure 4.4 (a) and (b)). By comparing them, it is clear that the sharpness of the spots is the same and therefore the sample was not damaged by its stay in air. This stability was already observed by Grønborg et al. for MoS_2 grown on Au(111)[32], but we can state that also MoS_2 on Ag(111) is chemically inert, though we expect this system to be metallic.

The principal spots of the LEED patterns corresponding to the MoS_2 lattice are surrounded by sharp first and second order satellites arranged in a hexagonal pattern, indicating the formation of long-range ordered MoS_2 layer. We speculate that these features in the LEED pattern are due to

the better ordering of the moiré superstructure than the one on Au(111) substrate, for which system the LEED measurements show only the first order satellites. The satellite spots are due to the moiré pattern, deriving from the lattice mismatch between Ag (lattice constant $\alpha_{Ag} \sim 0.288\,nm$) and MoS_2 ($\alpha_{MoS_2} \sim 0.315\,nm$). The pattern is in agreement with the 11 x 11/12 x 12 MoS_2/Ag(111) unit cell moiré superstructure. The spots originated by the substrate, marked with an arrow, coincide with one satellite. From the analysis of the line profile, shown in figure 4.4 (c), along the dashed line drawn in figure 4.4 (a), it is possible to calculate the β_{Ag} and β_{MoS_2} reciprocal vectors by evaluating the distance between the spots, obtaining a moiré reciprocal vector $\beta_{moiré}$ of 0.19 and, thus, a real space vector of 3.51±0.1 nm, in close agreement with the STM measurements and with the value for MoS_2 on Au(111). The absence of additional diffraction features rotated with respect to the Ag spots indicates that the MoS_2 unit cell is aligned parallel with the unit cell of the substrate, congruent with the disposition of MoS_2 on Au(111) reported in chapter 3. The LEED spots intensity analysis reveals that the pattern exhibits a 6-fold symmetry, as it is clearly visible in figure 4.4 (d) from the line profile analysis of the spots along the red ring in figure 4.4 (a) from 0° to 160° containing the MoS_2 spots. As the MoS_2 structure is three-fold symmetric, a six-fold LEED pattern is indicative of an equal distribution of the two oppositely oriented domains, rotated by 180°.

We now focus our analysis on the structural features of the MoS_2 layer and to better evaluate the amount of the mirror domain on the sample, we performed XPD measurements.

Firstly, the Ag 3d core level was measured for the bare Ag(111) to determine the orientation of the crystal. Figure 4.5 (a) shows the measured diffraction pattern (orange) from the Ag 3d core level with a photon energy of 480 eV, corresponding to a photoelectron kinetic energy of ∼112 eV. The pattern is three-fold symmetric, as expected for the Ag(111) substrate and this is also confirmed by XPD simulations (see 4.5 (a), grey region) performed using four layer close-packed Ag atoms, with a bulk truncated surface, oriented as sketched in figure 4.5 (b), and the same kinetic energy of the photoelectrons in the experiment, i.e. 112 eV.

The bottom and top S 2p and Mo 3d diffraction patterns, shown in figure 4.5 (c), (d) and (e), respectively, were simulated for a freestanding MoS_2 layer, as it was done in the case of MoS_2/Au(111). By properly tuning the photon energy, the kinetic energy of the photoemitted electrons has been chosen to enhance either the forward or the backward scattering. In particular, the electron kinetic energy for the scatterers was set high for the bottom S atoms, favoring forward scattering processes from the Mo and top S, and low for the Mo and top S atoms, favoring backscattering processes. In detail, we chose hν=560 eV, hν=360 eV and hν=270 eV (corresponding to ∼397 eV, ∼130 eV and ∼108 eV photoelectron kinetic energy) for bottom S, Mo and top S, respectively. The stereographic projections of Mo 3d and

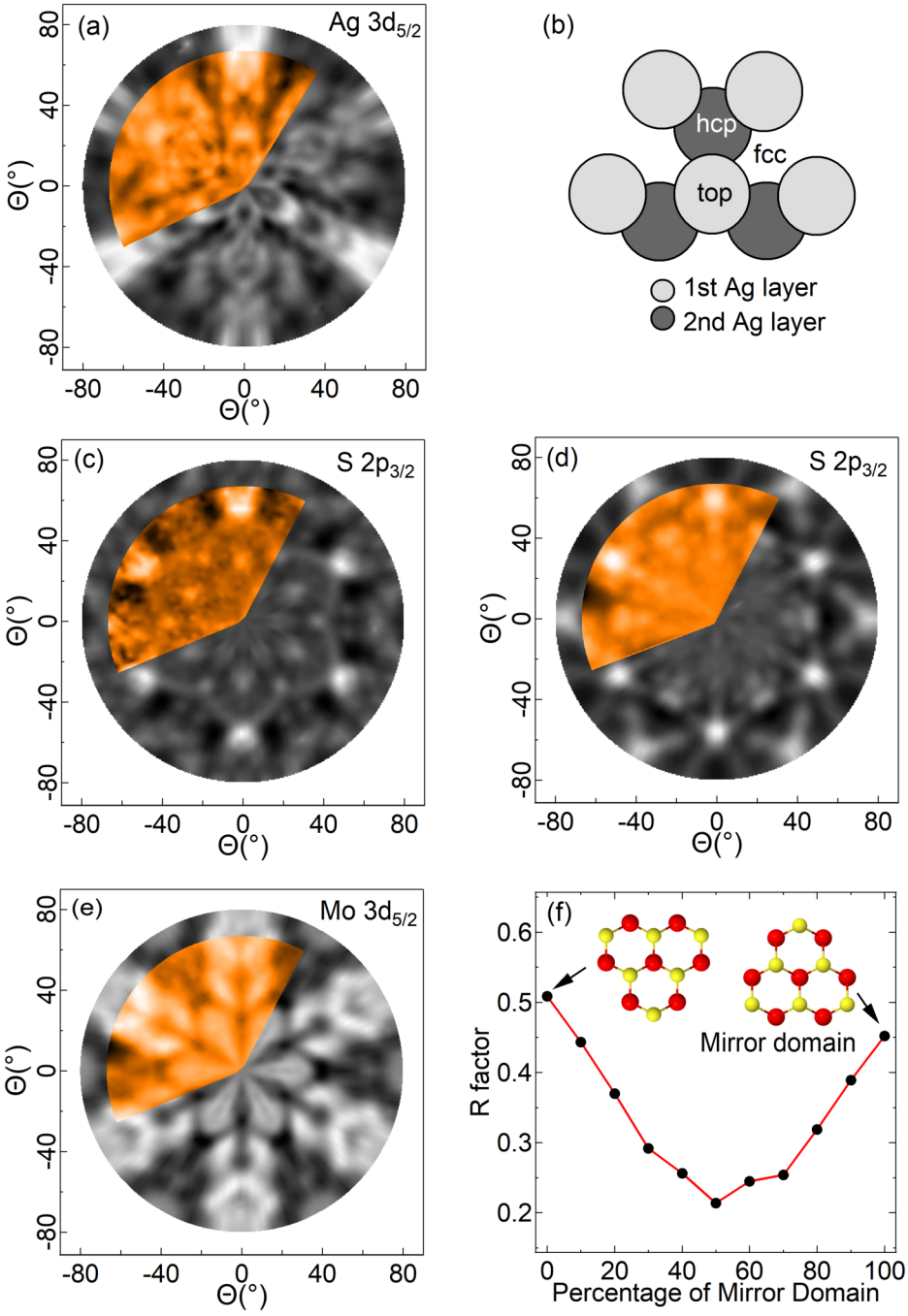

Figure 4.5: Stereographic projections of the integrated photoemission intensity modulation I(θ, ϕ) as a function of emission angle for (a) Ag $3d_{5/2}$ (hν=480 eV; E_k ~112 eV) (c) bottom S 2p (hν=560 eV; E_k ~397 eV), (d) top S 2p (hν=270 eV ;E_k ~108 eV) and (e) Mo 3d (hν=360 eV; E_k ~130 eV) core levels. The colored sectors are the experimental data, while simulations are shown in grey. (b) Geometric structure used to simulate the Ag(111) substrate. (f) R-factor behavior for the Mo $3d_{5/2}$ diffraction patters, as a function of the relative concentration of twin domains.

S 2p core levels show a clear six-fold symmetry, which is consistent with the presence of two MoS_2 domains with antiparallel orientations, as discussed for the LEED measurements. A good agreement between experimental and simulated patterns for S and Mo atomic layers at different energies confirm that we obtained a high quality non-distorted MoS_2. A minimum R-factor of 0.21 for the XPD pattern of Mo 3d was obtained for a lattice parameter of 3.2±0.07 Å, in very good agreement with the values reported in literature for MoS_2[29, 30]. These optimized distances were also used to compute the diffraction patterns for S 2p, yielding R-factors of 0.29 and 0.27 for the upper and lower S atoms, respectively. The excellent agreement between experimental data and simulations for the upper and lower S is the proof that in the S 2p XPS spectrum, the component at higher binding energy belongs to the bottom S and the component at lower BE to the top S.

In order to quantify the percentage of the two oppositely oriented MoS_2 domains, we calculated the R-factor between experimental diffraction pattern and simulation including weighted percentage of the two domains. Figure 4.5 (f) reports the graphical representation of R-factor variations for the percentage the two domains in the simulation with mixed orientations. The minimum of R-factor corresponds to 50% of both orientations, meaning that the two orientations aligned with the crystallographic axes of Ag(111) are equally probable, differently from what found for MoS_2 on Au(111), where using the same growth procedure, it is possible to grow singly oriented MoS_2 domains.

4.3.2 Structural characterization of MoS_2 on Ag(110)

Differently from the growth of MoS_2 on Ag(111), where the HTG approach was used from the beginning, on the Ag(110) substrate this method implicates the formation of randomly oriented MoS_2 rotated domains that invalidates the properties of the SL MoS_2 introducing structural defects. In order to avoid this undesirable structure, the growth was performed in two steps: first, the TPG approach was used up to a coverage of ∼0.07 ML to create MoS_2 nano-crystals and promote the expansion of the islands with a preferential orientation; then the HTG approach was used to increase the coverage to 0.75 ML of MoS_2, where a monolayer (ML) represents one complete layer of MoS_2 on Ag(110). The coverage was calculated from the decrease of the intensity of the Ag 3d spectrum (not reported here) by comparing it with the Ag 3d signal of the MoS_2 on Ag(111) system, as discussed in the previous section.

Figure 4.6 reports the HR XPS spectra of Mo 3d and S 2p core levels after the growth of $\theta \sim 0.75$ ML. The Mo 3d spectrum in figure 4.6 (a), similarly to that reported in figure 4.2 (c) for MoS_2 grown on Ag(111), shows a 3d spin-orbit splitting of 3.15 eV, consistent with the previous known value[21], and can be fitted with only one component for the main peak, i.e. the one

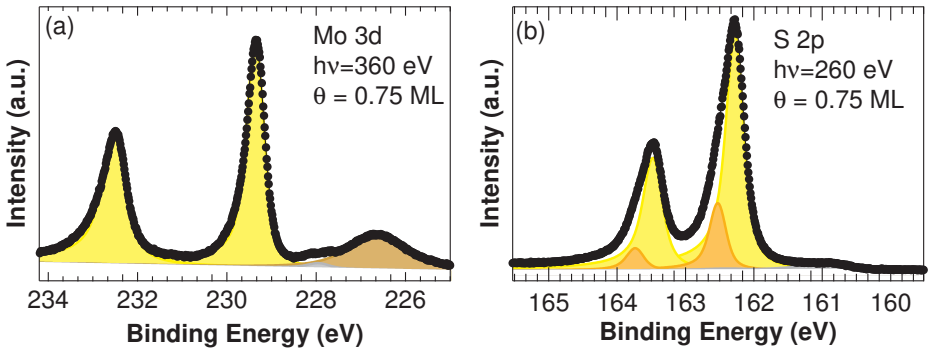

Figure 4.6: Mo 3d (a) and S 2p (b) core level spectra taken at hν=360 eV and hν=260 eV photon energy respectively, for MoS_2 grown on Ag(110)($\theta \sim 0.75$ ML). All the experimental spectra (data points) are presented with the resulting fit (line) and together with the spectral contributions resulting from peak fit analysis (solid areas).

centered at 229.33 eV binding energy, attributable to the basal plane of MoS_2. As previously discussed, the grey component at 227.9 eV BE can be attributed to not completely sulfided species. Finally, the brown component at lower binding energy growing at 226.65 eV is the S 2s core level.

The S 2p spectrum for the same sample is reported in figure 4.6 (b) and it shows a spin orbit doublet separated by 1.19 eV in close agreement with values found in literature[25]. It is fitted with two components, one colored in yellow centered at 162.27 eV and a smaller orange component with a shift of 240 meV to higher BE with respect to the previous one. As motivated in the previous chapter, we attribute the yellow component to the S atoms of the top layer plus the weakly interacting S atoms of the bottom layer of the S-Mo-S structure, while the orange one is attributed to the S atoms of the bottom layer strongly interacting with the Ag(110) substrate.

By comparing the MoS_2/Ag(110) with the MoS_2/Ag(111) systems, some similarities and differences can be appreciated. First of all, the BE positions of the both Mo 3d and S 2p components are centered at the same BE (see table 4.2 and table 4.1) and the components can be fitted with similar fitting parameters. In particular, the asymmetry parameter α=0.08 given to the Mo 3d peak in the case of the Ag(110) substrate is very close to that on Ag(111), α=0.10 and, as discussed in the previous section, thanks to the analogies with the WS_2 system grown on both Ag(111)[13], we attribute this non-zero asymmetry to the metallic behavior of MoS_2 on Ag(110). Looking at the S 2p core level spectra (see figure 4.6 (b) and 4.2 (d)), the orange component at higher BE in that of MoS_2 on Ag(110) is more intense than that for MoS_2 on Ag(111), pointing at a higher interaction of MoS_2 with the

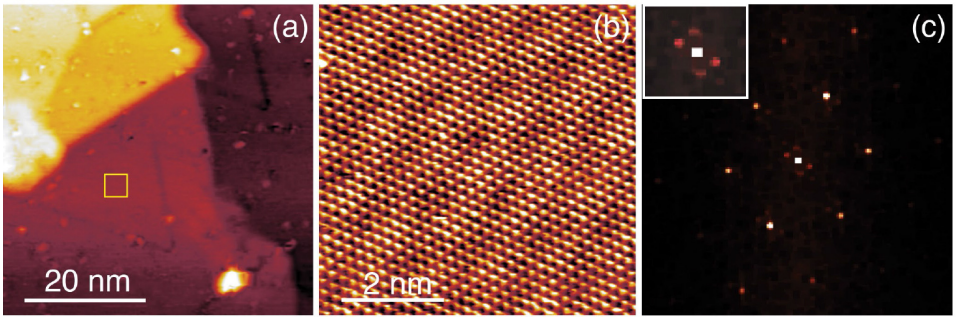

Figure 4.7: STM images showing MoS_2 extended layer at coverage $\theta \sim 0.75$ ML of MoS_2 on Ag(110). (a) 50x50 nm large scale image (V_B=-1.250 V, I_t=0.06 nA). (b) 6x6 nm atomically resolved STM image of the MoS_2 lattice and moiré superstructure of MoS_2/Ag(110) (V_B=-740 mV, I_t=1.51 nA) acquired in the region in the yellow box of (a). (c) FFT of the STM image reported in figure (b).

Ag(110) substrate.

Table 4.2: Doniach-Šunjić line shape parameters for the different components of the Au $4f_{7/2}$, Mo 3d and S 2p core levels acquired at room temperature at 360 eV and 260 eV photon energy, respectively. L is the Lorentzian width, α is the asymmetry parameter and G is the Gaussian width (see section 2.1.2 for detailed information). BE is the binding energy of the components normalized by the Fermi Level.

Mo 3d ($h\nu$=360eV)	L(eV)	α	G(eV)	BE(eV)
$3d_{5/2}$	0.20	0.08	0.35	229.33
$3d_{3/2}$	0.38	0.08	0.35	232.48
S 2p ($h\nu$=260eV)	L(eV)	α	G(eV)	BE(eV)
$2p_{3/2}$ top	0.17	0.06	0.21	162.27
$2p_{1/2}$ top	0.17	0.06	0.21	163.51
$2p_{3/2}$ bottom	0.18	0.06	0.21	162.47
$2p_{1/2}$ bottom	0.18	0.06	0.21	163.71

In order to characterize the structural properties of the MoS_2/Ag(110) system, we first performed STM measurements and figure 4.7 (a) reports a large scale STM image. Differently from the large scale STM images recorded on MoS_2/Ag(111) (see figure 4.3 (a)), where arrays of bright protrusions attributed to the presence of the moiré superstructure are visible, in this image one can only observe the steps and the terraces of the substrate. The presence of the MoS_2 is revealed when going into detail (yellow square in figure 4.7 (a)); indeed, in the atomically-resolved STM image in figure 4.7

(b), the bright protrusions induced by the S atoms of the topmost layer of MoS_2, arranged in a hexagonal pattern, are visible and the features of the moiré superstructure appear with a misalignment with respect to the S rows. In order to determine the features of the moiré superstructure, such as the periodicity and the rotation with respect to the MoS_2 lattice, the 2D FFT analysis of this image was done and is reported in figure 4.7 (c). The most peculiar feature is the rectangular arrangement of satellite spots around each of the main spots belonging to MoS_2. These spots, with a reciprocal space vector length five times smaller than that of MoS_2, show a 30°-rotation with respect to the MoS_2 lattice.

The 2D FFT of the STM image was then compared with the LEED pattern reported in figure 4.8 (a), where the main spots, highlighted with a red circle and related to the MoS_2 layer, are equally bright, resulting in a six-fold symmetric pattern that suggests the coexistence of an equal amount of oppositely oriented domains of MoS_2, as in the case of MoS_2/Ag(111). The other spots in the black circles originate from the Ag(110) substrate and they were identified by comparing this LEED pattern with that of the clean Ag(110) substrate at the same kinetic energy E_k=120 eV (see figure 4.8 (b)). Moreover, as already observed in the 2D FFT in figure 4.7 (c), the MoS_2 spots are surrounded by four satellite spots, due to the formation of the moiré superstructure, arranged in a rectangular pattern, as visible in the inset in figure 4.8 (a). Interestingly, one vertex of the rectangle coincides with the (1,1) diffraction spot of Ag(110), while the other two vertexes correspond to the $(1,\frac{1}{2})$ and $(\frac{4}{5},1)$ spots both referred to the same Ag(110) surface, thus proving that the components of the real space vector of the moiré superstructure are five times and two times the lattice parameters of the Ag(110) surface along the $[1\bar{1}0]$ and [001] directions, respectively. Hence, based on these findings, figure 4.8 (c) shows the ball model of the MoS_2 on Ag(110) system, which can be directly compared with the atomically resolved STM image in figure 4.8 (d). The periodicity and orientation of the moiré superstructure are indicated with the blue arrows. In order to satisfy this periodicity and to match the nearest integer number of Ag atoms underneath, the MoS_2 lattice vector, shown by the red arrow aligned along the $[1\bar{1}0]$ direction of the Ag(110) substrate, must be 3.25 Å long, implicating an elongation of around 3% in that direction, while the lattice vector in the other direction (green arrow) remains the same (3.15 Å) of that reported in literature[29, 30].

As pointed out in the previous paragraph, the six-fold symmetry of the LEED pattern reported in figure 4.8 (a) points at the presence of an equal proportion of anti-parallel domain orientations of MoS_2. Hence, in order to examine quantitatively this aspect, XPD measurements were performed on the sample. In analogy with the case of MoS_2 on Ag(111) and MoS_2 on Au(111), the photon energy was chosen in order to have the electron kinetic energy high for the bottom S atoms, favoring forward scattering processes from the Mo and top S, and low for the Mo and top S atoms, favoring

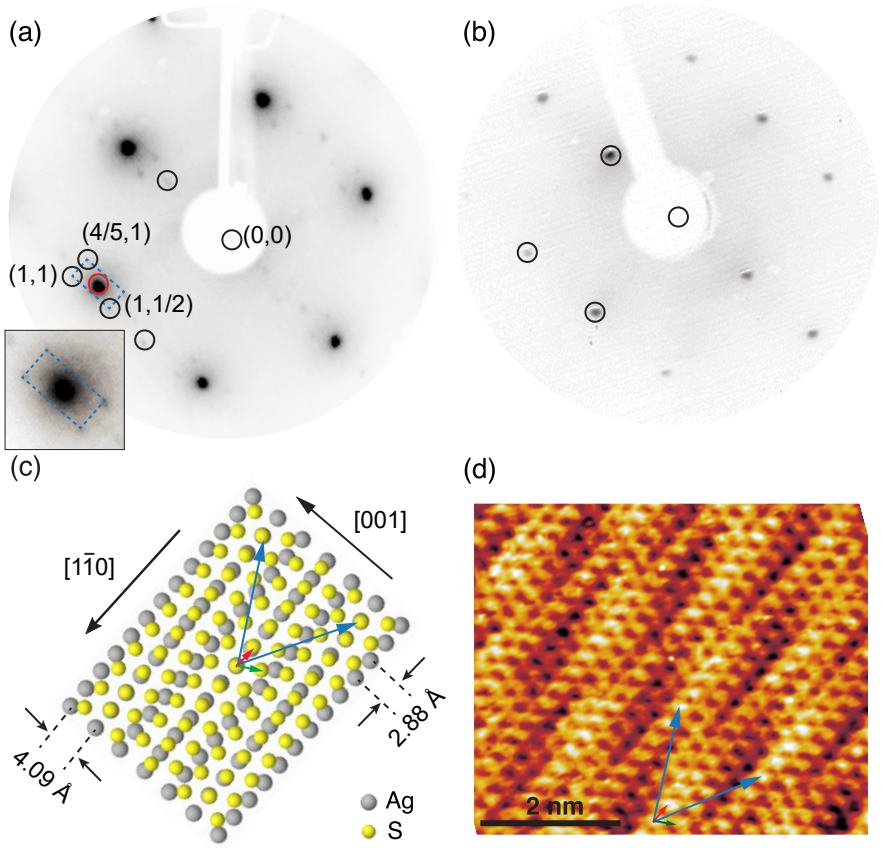

Figure 4.8: LEED patterns of (a) θ ~0.75 ML MoS_2 grown on Ag(110) and (b) the clean Ag(110) surface at E_k=120 eV electron energy. The spots of MoS_2 (red circle) and Ag(110) (black circles) are indicated. (c) Representation of the MoS_2/Ag(110) system, where the yellow balls are the top S atoms and the grey ones the Ag surface atoms. The blue arrows represent the lattice parameters of the moiré superstructure, while the red and green arrows are the lattice parameters of MoS_2. (d) Atomically resolved STM image (V_B=1200 mV, I=2.05 nA) showing the MoS_2 layer and the moiré superstructure.

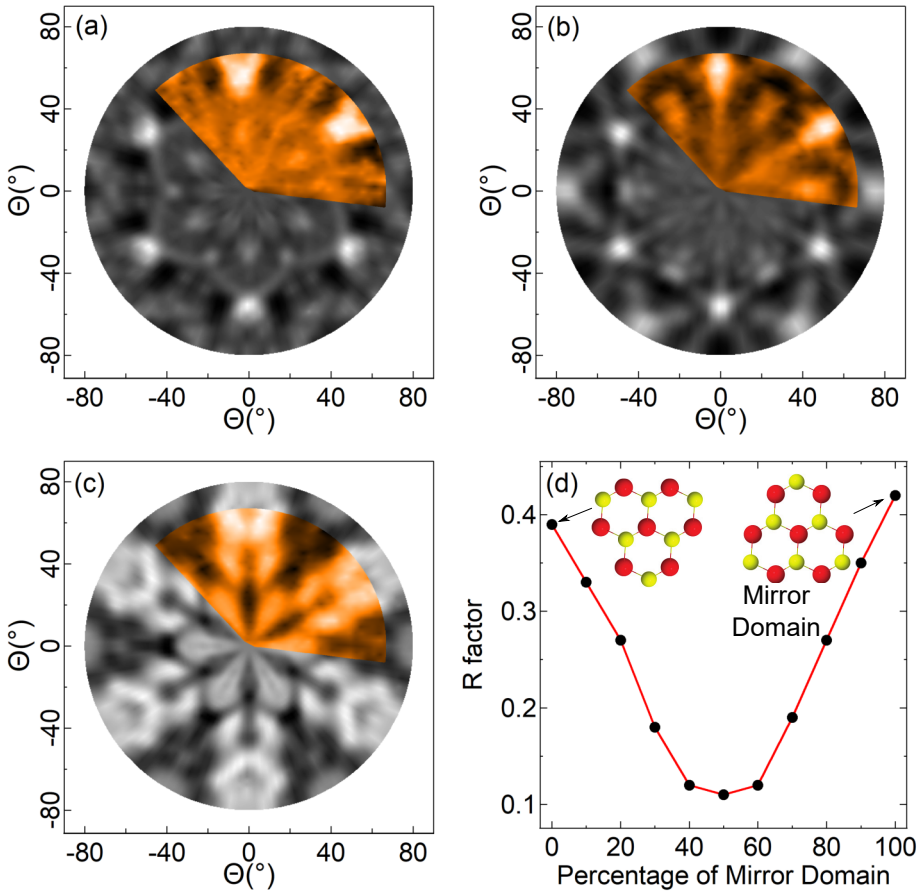

Figure 4.9: Stereographic projections of the integrated photoemission intensity modulation I(θ, ϕ) as a function of emission angle for (a) bottom S 2p (hν= 560 eV; E_k ~397 eV), (b) top S 2p (hν= 270 eV; E_k ~108 eV) and (c) Mo 3d (hν= 360 eV; E_k ~130 eV) core levels. The colored sectors are the experimental data, while the simulations are shown in grey. (d) R-factor behavior for the Mo $3d_{5/2}$ diffraction patters, as a function of the relative amount of the mirror domain.

backscattering processes. We chose hν=560 eV, hν=360 eV and hν=270 eV (397 eV, 130 eV and 108 eV photoelectron kinetic energy) for bottom S, Mo and top S, respectively. For the simulations, the substrate was neglected due to the lack of specific adsorption configuration of MoS_2 layer on Ag(110). They were performed for a 1H phase (see figure 1.2 in the introductive chapter) free standing MoS_2 layer, with a lattice parameter of 3.15 Å and a Mo-S interlayer distance of 1.62 Å[29, 30].

The results are reported in figure 4.9, together with the simulated patterns. Figure 4.9 (a) and (b) report the stereographic projections for the bottom and top S atoms. The first consideration concerns the excellent agreement between experimental data and simulations, which suggests that in the S 2p XPS spectrum, the component at higher BE belongs to the bottom S and the component at lower BE has a prevalent contribution from the top S layer. Moreover, looking also at the Mo 3d diffraction pattern in figure 4.9 (c), one can note a clear six-fold symmetry of the patterns, which is consistent with the presence of two MoS_2 domains with anti-parallel orientations. In order to quantify the percentage of the two oppositely oriented MoS_2 domains, we calculated the R-factor for the experimental diffraction pattern and simulation including weighted percentages of the two domains. Figure 4.9 (d) reports the corresponding R-factor variations. Analogously to MoS_2 on Ag(111), the minimum of R-factor corresponds to 50% of both orientations. This means that two antiparallel orientations are equally probable on the Ag(110) substrate, analogously to the MoS_2 on Ag(111) but differently from what found for MoS_2 on Au(111).

To investigate the mutual orientation of the MoS_2 overlayer with respect to the Ag(110) and to further prove that the MoS_2 layer is aligned with one crystallographic direction of the substrate, we measured the Ag $3d_{5/2}$ core level XPD pattern and we compared it with a simulation performed using three Ag layers, with the atoms in all three layers emitting simultaneously. The pattern is shown in figure 4.10 (a) and it is two-fold symmetric, as expected from the Ag(110) rectangular lattice. From the comparison between experiment and simulation, the crystal orientation was found to be the one reported in figure 4.10 (b). By comparing the orientation of the substrate with that of MoS_2 sketched in figure 4.9 (d), we can obtain the relative orientation, reported in figure 4.10 (c) and (d), of the adlayer with respect to the substrate, assuming that MoS_2 locally adsorbs with the S atoms in the top position. Therefore, based on the experimental data and simulation results, we can prove that the MoS_2 layer is aligned parallel to the dense packed rows along the $[1\bar{1}0]$ direction of the Ag(110) substrate, assuming two equally probable orientations, in agreement with the LEED findings previously discussed.

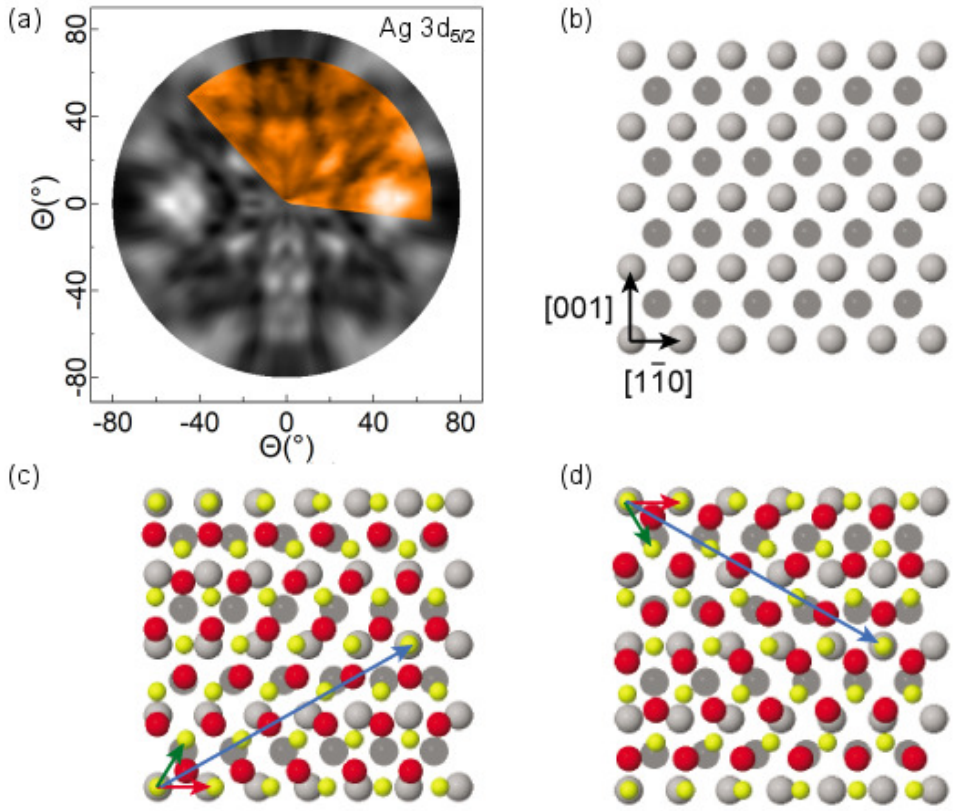

Figure 4.10: (a) Stereographic projections of the integrated photoemission intensity modulation I(θ, ϕ) as a function of emission angle for the Ag $3d_{5/2}$ core level (hν=480 eV; E_k ~112 eV). The colored sectors are the experimental data, while the simulations are shown in grey. (b) Geometric structure used to simulate the Ag(110) substrate. (c) and (d) are the orientations of the two domains of MoS_2 on Ag(110). The MoS_2 lattice vector (red arrow) is aligned with the [1$\bar{1}$0] direction of Ag(110). Mo atoms are colored in red, S atoms in yellow, the Ag surface atoms in light grey, while the Ag second layer atoms in dark grey.

4.4 Conclusions

In this chapter, we studied the growth of MoS_2 on two Ag surfaces, Ag(111) and Ag(110), with the aim of verifying the higher interaction between adlayer and substrate, as predicted by theoretical studies, and understanding if this promotes the formation of extended layers of MoS_2. Moreover, we wanted to investigate the possibility of a semiconductor-to-metal MoS_2 transition. Starting from the Ag(111) substrate, we used the HTG approach that we developed for the growth of MoS_2 on Au(111) and by means of fast-XPS, we studied the dynamics of the process which results in the direct formation of MoS_2. The fitting and the study of the HR XPS spectra excluded the presence of species different from MoS_2 and, moreover, they were useful to make a comparison with the MoS_2/Au(111) system. Indeed, some differences were found: first, all the peaks are shifted towards higher BE in the case of MoS_2 on Ag(111) with respect to that on Au(111). In addition, considering the line shape of Mo 3d and similar studies on WS_2 reported in literature[13], we speculate that MoS_2 on Ag(111) has a metallic behavior. Finally, from the fitting of S 2p core level spectrum, it is possible to affirm that MoS_2 interacts more with Ag(111) than Au(111), as theoretically predicted[11, 12]. Unlike MoS_2 on Au(111), LEED and XPD measurements proved that the HTG method on Ag(111) leads to the formation of an equal amount of the two oppositely oriented domains. However, the STM investigation allowed to evaluate the extension of the layer, that crosses the terraces of the substrate.

We then moved to the anisotropic Ag(110) surface to investigate if the different symmetry of the substrate modifies the structural properties of MoS_2 and we successfully grew SL MoS_2 that was characterized by means of XPS, XPD, LEED and STM measurements. The HR-XPS spectra presented the same features of those of MoS_2 grown on Ag(111), with a higher intensity of the S 2p component related to the bottom S atoms strongly interacting with the substrate, indicating the higher interaction of the adlayer with Ag(110) with respect to the Ag(111), and a non-zero asymmetry in the Mo 3d peak, suggesting the metallic behavior of MoS_2 grown on Ag(110). By means of STM and LEED analyses, we demonstrated the high structural quality of the layer and detected the presence of a moiré superstructure, that in the STM images appears as alternating lines. This superstructure appears misaligned by 30° with respect to the MoS_2 lattice with a periodicity which is 5 times the MoS_2 lattice parameter. Finally, by means of the XPD measurements, we demonstrated the presence of equal amount of oppositely oriented domains of MoS_2.

In conclusion, we showed that our growth approach, leading to highly crystalline MoS_2 extended layers, together with the supposed metallic behavior of MoS_2 due to the interaction with the silver substrate, could open the path towards the development of low contact resistance monolayer MoS_2 based devices.

References

[1] Allain, A.; Kang, J.; Banerjee, K.; Kis, A. Electrical contacts to two-dimensional semiconductors. *Nature Materials* **2015**, *14*, 1195–1205.

[2] Breil, N. et al. Highly-selective superconformai CVD Ti silicide process enabling area-enhanced contacts for next-generation CMOS architectures. 2017 Symposium on VLSI Technology. 2017; pp T216–T217.

[3] Yu, H. et al. Ultralow-resistivity CMOS contact scheme with pre-contact amorphization plus Ti (germano-)silicidation. 2016 IEEE Symposium on VLSI Technology. 2016; pp 1–2.

[4] Adusumilli, P. et al. Ti and NiPt/Ti liner silicide contacts for advanced technologies. 2016 IEEE Symposium on VLSI Technology. 2016; pp 1–2.

[5] Eda, G.; Fujita, T.; Yamaguchi, H.; Voiry, D.; Chen, M.; Chhowalla, M. Coherent Atomic and Electronic Heterostructures of Single-Layer MoS_2. *ACS Nano* **2012**, *6*, 7311–7317.

[6] Kappera, R.; Voiry, D.; Yalcin, S. E.; Branch, B.; Gupta, G.; Mohite, A. D.; Chhowalla, M. Phase-engineered low-resistance contacts for ultrathin MoS_2 transistors. *Nature Materials* **2014**, *13*, 1128–1134.

[7] Kappera, R.; Voiry, D.; Yalcin, S. E.; Jen, W.; Acerce, M.; Torrel, S.; Branch, B.; Lei, S.; Chen, W.; Najmaei, S.; Lou, J.; Ajayan, P. M.; Gupta, G.; Mohite, A. D.; Chhowalla, M. Metallic 1T phase source/drain electrodes for field effect transistors from chemical vapor deposited MoS_2. *APL Materials* **2014**, *2*, 092516.

[8] Popov, I.; Seifert, G.; Tománek, D. Designing Electrical Contacts to MoS_2 Monolayers: A Computational Study. *Physical Review Letters* **2012**, *108*, 156802.

[9] Das, S.; Chen, H.-Y.; Penumatcha, A. V.; Appenzeller, J. High Performance Multilayer MoS_2 Transistors with Scandium Contacts. *Nano Letters* **2013**, *13*, 100–105.

[10] Kang, J.; Liu, W.; Sarkar, D.; Jena, D.; Banerjee, K. Computational Study of Metal Contacts to Monolayer Transition-Metal Dichalcogenide Semiconductors. *Physical Review X* **2014**, *4*, 031005.

[11] Zhong, H.; Quhe, R.; Wang, Y.; Ni, Z.; Ye, M.; Song, Z.; Pan, Y.; Yang, J.; Yang, L.; Lei, M.; Shi, J.; Lu, J. Interfacial Properties of Monolayer and Bilayer MoS_2 Contacts with Metals: Beyond the Energy Band Calculations. *Scientific Reports* **2016**, *6*, 21786–21802.

[12] Farmanbar, M.; Brocks, G. First-principles study of van der Waals interactions and lattice mismatch at MoS_2/metal interfaces. *Physical Review B* **2016**, *93*, 085304.

[13] Dendzik, M.; Bruix, A.; Michiardi, M.; Ngankeu, A. S.; Bianchi, M.; Miwa, J. A.; Hammer, B.; Hofmann, P.; Sanders, C. E. Contact-Induced Semiconductor-to-Metal Transition in Single-Layer WS_2. *ArXiv e-prints* **2017**,

[14] Šrut, I.; Trontl, V. M.; Pervan, P.; Kralj, M. Temperature dependence of graphene growth on a stepped iridium surface. *Carbon* **2013**, *56*, 193–200.

[15] Vinogradov, N. A.; Zakharov, A. A.; Kocevski, V.; Rusz, J.; Simonov, K. A.; Eriksson, O.; Mikkelsen, A.; Lundgren, E.; Vinogradov, A. S.; Mårtensson, N.; Preobrajenski, A. B. Formation and Structure of Graphene Waves on Fe(110). *Physical Review Letters* **2012**, *109*, 026101.

[16] Vinogradov, N. A.; Zakharov, A. A.; Ng, M. L.; Mikkelsen, A.; Lundgren, E.; MÃërtensson, N.; Preobrajenski, A. B. One-Dimensional Corrugation of the h-BN Monolayer on Fe(110). *Langmuir* **2012**, *28*, 1775–1781.

[17] Abrami, A. et al. Super ESCA: First beamline operating at ELETTRA. *Review of Scientific Instruments* **1995**, *66*, 1618–1620.

[18] Rovida, G.; Pratesi, F. Sulfur overlayers on the low-index faces of silver. *Surface Science* **1981**, *104*, 609–624.

[19] Zhang, W.; Zhang, L.; Hui, Z.; Zhang, X.; Qian, Y. Synthesis of nanocrystalline Ag_2S in aqueous solution. *Solid State Ionics* **2000**, *130*, 111–114.

[20] Andersen, J. N.; Hennig, D.; Lundgren, E.; Methfessel, M.; Nyholm, R.; Scheffler, M. Surface core-level shifts of some 4 *d* -metal single-crystal surfaces: Experiments and *ab initio* calculations. *Physical Review B* **1994**, *50*, 17525–17533.

[21] Castañeda, S. I.; Montero, I.; Ripalda, J. M.; Díaz, N.; Galán, L.; Rueda, F. X-ray photoelectron spectroscopy study of low-temperature molybdenum oxidation process. *Journal of Applied Physics* **1999**, *85*, 8415–8418.

[22] Sørensen, S. G.; Füchtbauer, H. G.; Tuxen, A. K.; Walton, A. S.; Lauritsen, J. V. Structure and Electronic Properties of In Situ Synthesized Single-Layer MoS_2 on a Gold Surface. *ACS Nano* **2014**, *8*, 6788–6796.

[23] Bruix, A.; Füchtbauer, H. G.; Tuxen, A. K.; Walton, A. S.; Andersen, M.; Porsgaard, S.; Besenbacher, F.; Hammer, B.; Lauritsen, J. V. In Situ Detection of Active Edge Sites in Single-Layer MoS_2 Catalysts. *ACS Nano* **2015**, *9*, 9322–9330.

[24] Baker, M.; Gilmore, R.; Lenardi, C.; Gissler, W. XPS investigation of preferential sputtering of S from MoS_2 and determination of MoS_x stoichiometry from Mo and S peak positions. *Applied Surface Science* **1999**, *150*, 255–262.

[25] Cavalleri, O.; Gonella, G.; Terreni, S.; Vignolo, M.; Pelori, P.; Floreano, L.; Morgante, A.; Canepa, M.; Rolandi, R. High resolution XPS of the S 2p core level region of the L-cysteine/gold interface. *Journal of Physics: Condensed Matter* **2004**, *16*, S2477.

[26] Kumar, A.; Ahluwalia, P. K. Electronic structure of transition metal dichalcogenides monolayers 1H-MX_2 (M = Mo, W; X = S, Se, Te) from ab-initio theory: new direct band gap semiconductors. *The European Physical Journal B* **2012**, *85*, 186.

[27] Dendzik, M.; Michiardi, M.; Sanders, C.; Bianchi, M.; Miwa, J. A.; Grønborg, S. S.; Lauritsen, J. V.; Bruix, A.; Hammer, B.; Hofmann, P. Growth and electronic structure of epitaxial single-layer WS_2 on Au(111). *Phys. Rev. B* **2015**, *92*, 245442.

[28] Citrin, P. H.; Wertheim, G. K.; Baer, Y. Many-body processes in x-ray photoemission line shapes from Li, Na, Mg, and Al metals. *Phys. Rev. B* **1977**, *16*, 4256–4282.

[29] Holinski, R.; Gänsheimer, J. A study of the lubricating mechanism of molybdenum disulfide. *Wear* **1972**, *19*, 329–342.

[30] Winer, W. Molybdenum disulfide as a lubricant: A review of the fundamental knowledge. *Wear* **1967**, *10*, 422–452.

[31] Coraux, J.; N'Diaye, A. T.; Busse, C.; Michely, T. Structural Coherency of Graphene on Ir(111). *Nano Letters* **2008**, *8*, 565–570.

[32] Grønborg, S. S.; Ulstrup, S.; Bianchi, M.; Dendzik, M.; Sanders, C. E.; Lauritsen, J. V.; Hofmann, P.; Miwa, J. A. Synthesis of Epitaxial Single-Layer MoS_2 on Au(111). *Langmuir* **2015**, *31*, 9700–9706.

Chapter 5

Growth and characterization of single-layer WS_2 on Au(111)

5.1 Introduction

Tungsten disulfide WS_2, like MoS_2, is a direct band gap semiconductor in its single layer (SL) form and consists of a layer of close-packed tungsten atoms sandwiched between two layers of close-packed sulfur atoms, arranged in the stable trigonal prismatic phase (1H). Single-layer WS_2 is commercially used as catalyst in the oil refining processes thanks to its strong hydrogenation function[1]. Another interesting feature of SL WS_2 is the absence of inversion symmetry that, together with the heavy W atoms, leads to a strong lifting of the spin degeneracy in the valence band structure close to the K-points of the Brillouin zone. Furthermore, due to time reversal symmetry, the strong spin polarization in the K and K' valleys is reversed, as shown in figure 1.3[2], leading to a unique spin-valley-locked band structure[3–5]. In the case of single oriented domain SL, such exotic local properties can be preserved over the whole SL making possible to exploit the so-called spin-valleytronic, paving the way towards a new paradigm for store and share information[2, 3]. However, there are basically two big challenges: the first is related to the effective production of spin-valley polarized carriers[6], and the second is related to the life-time of such carriers that should be long enough in order for the information to be effectively managed. In this framework, WS_2 is a promising candidate for such applications due to a combination of spin- and energy-protected scattering[7], described in section 5.3.3 thanks to ARPES technique, that allows for larger life-times if compared with other SL materials such as graphene[8–10] and MoS_2[2, 3]. Therefore, aiming to the application of WS_2 for spin- and valley-tronics, the coexistence of mirror domains is a considerable barrier, as already explained in chapter 3 and the presence of

equal amount of mirror domains results in an overall completely non spin-polarized bands. So far, all the works in the literature show the presence of mirror domains in the growth of TMDCs[11], therefore, we focused on finding a growth approach to obtain a high degree of orientation for future technology.

In this chapter we show that, by modifying a bottom up method already present in the literature[12], which in turn takes inspiration from the procedure described by Füchtbauer et al.[1], it is possible to produce singly oriented SL WS_2 on Au(111). The structural properties of this overlayer were measured using XPD, while through ARPES measurements we characterized the electronic structure and quantified the magnitude of the electron-phonon scattering in the dominant valence band valleys. Moreover, the synthesis of SL WS_2 demonstrated the versatility of the developed growth method, which was already used for the growth of singly oriented MoS_2 and described in chapter 3.

5.2 Experimental details

The Au(111) substrate was prepared by repeated cycles of Ar^+ sputtering at 2 keV, and annealing at 940 K for 10 minutes, with 1 K s^{-1} heating and cooling rate. Two different procedures have been followed for the growth of WS_2 on Au(111). The first, hereon referred to as uptake 1, was performed by dosing atomic W at the rate of 0.007 ML per minute onto a clean Au(111) substrate kept at 873 K in H_2S pressure (1×10^{-6} mbar). During the growth, the sample temperature was varied between 823 K and 923 K. The second method, called uptake 2, consisted in dosing atomic W at much lower rate of 0.004 ML per minute onto a clean Au(111) substrate kept at 923 K in a initial background pressure of 5×10^{-6} mbar of H_2S, which was raised to 1×10^{-5} mbar after 10 percent of the growth and then kept between 1×10^{-5} mbar and 2×10^{-5} mbar. Fast-XPS was performed during the growth looking simultaneously the W 4f and S 2p core levels with 260 eV photon energy[13]. The S 2p, W 4f and Au 4f high resolution spectra were measured using photon energies of 260, 140 and 136 eV, respectively. The patterns for S 2p were acquired at $h\nu = 270$ eV (electron kinetic energy E_k ~108 eV) for the top S layer, and at $h\nu = 560$ eV (E_k ~397 eV) for the bottom S layer. The XPD measurements for W 4f were performed with photon energy of 360 eV and 170 eV corresponding to electron kinetic energies of ~325 eV and 135 eV, respectively.

For a more complete description of the experimental parameters, see chapter 2.10

5.3 Results and discussion

5.3.1 Growth of WS_2

The growth technique employed for the synthesis of WS_2 on Au(111) described in this chapter is based on the procedure already presented in reference [12], where W deposition occurs at room temperature in H_2S background pressure and in a second step the sample is annealed at 923 K for 30 minutes, and also on the HTG approach previously described in chapter 3 for the growth of MoS_2 on Au(111). We here describe the two growth approches that have been used and compared in this chapter.

The first approach for the WS_2 synthesis (uptake 1) was done following the HTG growth of MoS_2 on Au(111) and W was dosed at 0.0075 ML per minute in $1\,x\,10^{-6}$ mbar of H_2S keeping the sample at 873 K. In order to find the best conditions to inhibit the formation of species different from WS_2, the sample temperature was varied between 823 K and 923 K. The second approach (uptake 2) consisted in using a constant sample temperature of 923 K, a lower W rate of 0.0033 ML/min and a higher H_2S pressure of $5\,x\,10^{-6}$ mbar that was then increased between $1\,x\,10^{-5}$ mbar and $2\,x\,10^{-5}$ after 10% of the growth. The two growths were followed by fast-XPS and the spectra were fitted with parameters based on the ones used for the HR spectra, that will be described below. As already done for MoS_2 on Au(111) and Ag(111), the Gaussian parameter was increased to take into account the broadening of the peaks with respect to the HR ones taken ad room temperature. Figure 5.1 (a) reports the photoemission intensity of W $4f_{7/2}$ component of the WS_2 basal plane as a function of the dose time for both uptake 1 and uptake 2, in red and black, respectively. For comparison, the two trends are overlapped and the intensity of the W $4f_{7/2}$ peak is normalized to 1. The red curve has a non-linear behavior as the growth proceeds, whereas the black curve shows a linear trend throughout the whole growth. In general, as observed in figure 3.4 (c) where we report the intensity of the Mo $3d_{5/2}$ component during the growth of MoS_2 on Au(111), the bending of the W 4f core level intensity towards a plateau in the last stages of the growth is ascribable to the proximity to the completeness of one monolayer. However, through the fitting of the HR spectra of Au $4f_{7/2}$ core level that will be described below, we determined a coverage well below 1 ML ($\theta \sim 0.45$ ML for both uptake 1 and uptake 2). Therefore, unlike the linear trend clearly visible in uptake 2, the trend in uptake 1 could indicate also the formation of second layer islands.

After the growth, we measured the HR-XPS spectra of Au 4f, W 4f and S 2p core levels. The fitting parameters and the binding energies are reported in table 5.1. For W 4f and S 2p, the line-shapes of the basal plane WS_2 components have been reported only for uptake 2, as they were the same for both uptakes.

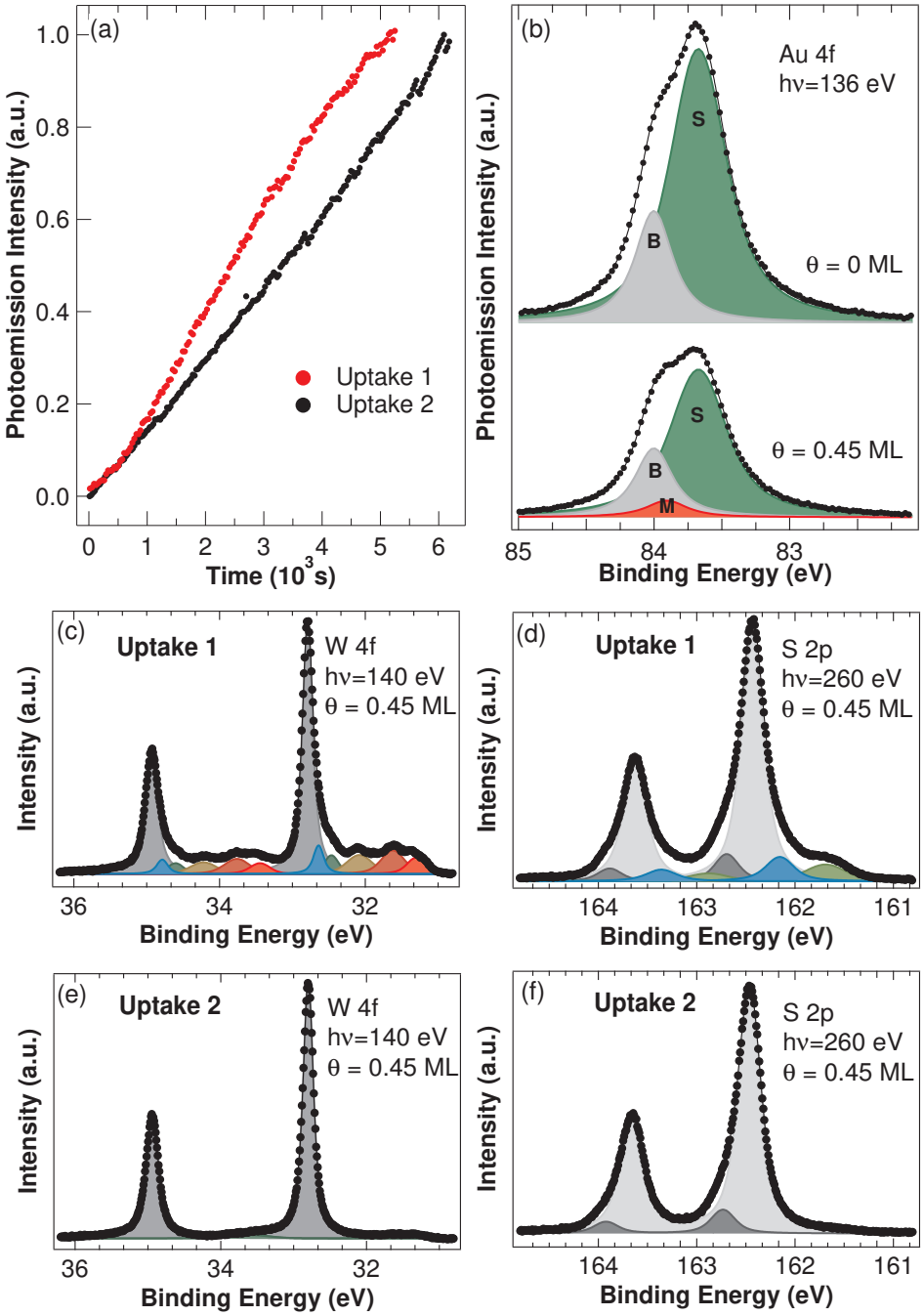

Figure 5.1: (a) Photoemission intensity of the W $4f_{7/2}$ component of the WS_2 basal plane as a function of dose time for uptake 1 (red) and uptake 2 (black). (b) Au $4f_{7/2}$ core level XPS spectra of clean Au(111) surface (top) and after WS_2 growth through uptake 2 with coverage of 0.45 ML (bottom) at 136 eV photon energy. W 4f (c) and S 2p (d) core level spectra taken at 140 eV and 260 eV photon energy respectively, for WS_2 grown through uptake 1 ($\theta \sim 0.45$ ML). W 4f (e) and S 2p (f) core level spectra taken at 140 eV and 260 eV photon energy respectively, for WS_2 grown through uptake 2 ($\theta \sim 0.45$ ML). All the experimental spectra (data points) are presented with the resulting fit (line) and together with the spectral contributions resulting from peak fit analysis (solid areas).

Table 5.1: Doniach-Šunjić line shape parameters for the different components of the Au, the W $4f_{7/2}$ and S 2p core levels acquired at room temperature with 136 eV, 140 eV and 260 eV photon energy, respectively. L is the Lorentzian width, α is the asymmetry parameter and G is the Gaussian width (see section 2.1.2 for detailed information). BE is the binding energy of the components.

Au 4f $_{7/2}$ ($h\nu$=136eV)	L(eV)	α	G(eV)	BE(eV)
Bulk (B)	0.31	0.02	0.09	84.00
Surface (S)	0.37	0.02	0.23	83.67
WS_2 (M)	0.37	0.02	0.23	83.89
W 4f ($h\nu$=140eV)	L(eV)	α	G(eV)	BE(eV)
$4f_{7/2}$	0.13	0.01	0.08	32.78
S 2p ($h\nu$=260eV)	L(eV)	α	G(eV)	BE(eV)
$2p_{3/2}$ top	0.19	0.00	0.16	162.43
$2p_{3/2}$ bottom	0.19	0.00	0.18	162.69

The Au 4f core level spectra for the clean Au(111) surface and for WS_2 coverage of 0.45 ML after uptake 2 are shown in figure 5.1 (b). The Au spectrum after the growth through uptake 1 was omitted because it does not differ from that of uptake 2. The clean sample shows two peaks belonging to the bulk (B), centered at 84.00 eV binding energy, and to the herringbone reconstructed surface (S) (see chapter 3 on MoS_2 on Au(111) for more details), at 83.67 eV, with a surface core level shift of 0.33 eV, in good agreement with the literature[14]. As in the case of MoS_2 on Au(111), the growth of WS_2 affects the Au 4f core levels. In fact, figure 5.1 (b) shows that after the WS_2 growth with a final coverage of 0.45 ML (see below for the coverage determination), the clean surface component decreases while an additional peak (M) centered at 83.89 eV, that lies between the bulk and the surface peaks, rises because of the interaction between WS_2 and Au(111). Our results are different from the ones reported in a previous study, where the Au 4f spectrum, after the growth of 0.7 ML WS_2 (1 ML from here refers to one complete layer of WS_2), was fitted without the addition of an intermediate component, and letting the surface peak move towards the bulk peak, with a new surface core level shift of 0.27 eV[12]. We ascribe this choice to a probably poorer resolution in these measurements. The line-shape and the binding energy position of the M component are the same as the one raising from the interaction between MoS_2 and Au(111) (see table 3.1), suggesting that this interaction is of the same nature. Even though no study has been done on the lifting of the herringbone reconstruction in the presence of WS_2, this is likely to happen, as the systems WS_2/Au(111) and MoS_2 have many common features, and for the latter an extended study on the lifting of the

herringbone reconstruction was carried out in reference [15].

Incidentally, we note that Gao et al. found the magnitude of this interaction to be weak enough to enable the intact transfer of the WS_2 onto arbitrary substrates without sacrificing the Au foil[16], thus making this system interesting for device applications.

The Au 4f spectra were crucial to determine the coverage of WS_2; indeed, as in the case of MoS_2 on Au(111) in chapter 3, the intensity of the S component is maximum for the bare surface, it decreases with the increasing WS_2 coverage and is expected to go to 0 when a full monolayer of WS_2 is on top. Considering that the growth of WS_2 proceeds via islands formation[1], the coverage θ_{WS_2} was calculated from the intensity of the S component normalized to one for the clean surface, as: θ_{WS_2}=1-I_S. The resulting WS_2 coverage was 0.45 ML.

Moving to the HR-XPS spectra of W and S core levels reported in figure 5.1 (c)-(f), it is clear that modest changes in the growth parameters, namely lower W dose rate, higher temperature and higher H_2S pressure for uptake 2 with respect to uptake 1, affect significantly the final result. The W 4f spectra measured after uptake 1 and uptake 2 are shown in figure 5.1 (c) and (e), respectively, and in both uptakes, the main spin-orbit doublet belonging to the basal plane WS_2 is centered at 32.78 eV BE with a spin orbit splitting of 2.14 eV, in perfect agreement with previous findings (BE W $4f_{7/2}$= 32.72 eV and spin orbit splitting of 2.13 eV)[12]. Observing the two spectra, one immediately notes the presence of many small components, most likely due to incompletely sulfided regions WS_{2-x} ($0<x\leq1$) or metallic W clusters[1, 17], in uptake 1. In contrast, they are totally absent in uptake 2.

The S 2p spectra for the two growth approaches are reported in figure 5.1 (d) and (f). For uptake 2, except for a very small component not belonging to the S in the basal plane of WS_2, the spectrum can be fitted with two components centered at 162.43 eV and 162.69 eV BE and with a spin-orbit splitting of 1.2 eV. Considering the similarities between WS_2 and MoS_2 and keeping in mind the study on MoS_2 described in chapter 3, we attribute the peak at higher BE (dark grey) to the strongly interacting bottom S atoms and the component at lower BE (light grey) to the S atoms of the top layer plus the weakly interacting S atoms of the bottom layer.

5.3.2 XPD and LEED measurements

XPD measurements allowed us to determine the structure and the orientation of the WS_2 layer on Au(111). As XPD is very sensitive to the local environment of the emitter[18], it can be used to ascertain the geometry of the layer, i.e. trigonal prismatic (1H) or octahedral (1T), and the distribution of mirror domains, as it was done in the previous chapters. Figure 5.2 (a) and (b) report the diffraction patterns of the strongly interacting bottom S $2p_{3/2}$ and W $4f_{7/2}$ core levels of uptake 2, measured with kinetic energy of 397

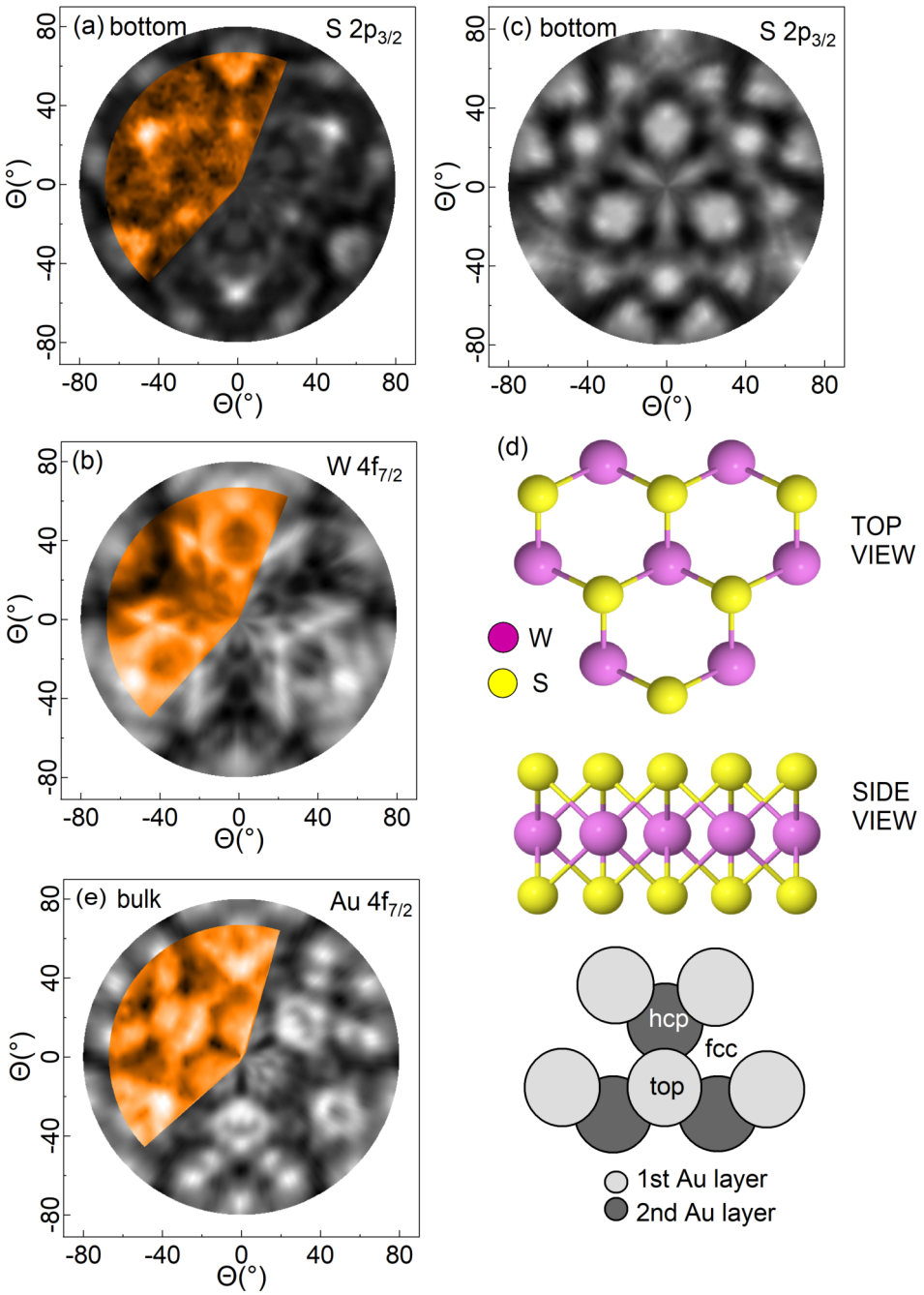

Figure 5.2: Stereographic projections of the integrated photoemission intensity modulation $I(\theta, \phi)$ as a function of emission angle for (a) the dark grey component of the S $2p_{3/2}$ spectrum of figure 5.1 (f) related to the bottom S (Ek∼397 eV; hν=560 eV), (b) W $4f_{7/2}$ (Ek∼135 eV; hν=170 eV) and (e) Au $4f_{7/2}$ bulk component (Ek∼312 eV; hν=400 eV) core levels. The colored sectors are the experimental data, while simulations are shown in grey. (c) simulation for bottom S in a 1T phase. Geometric structures used to simulate these patterns are shown in (d) and (f) for the WS_2 layer (W: red, S: yellow) and the Au(111) substrate, respectively.

eV and 135 eV, respectively, together with simulation results (grey region) calculated using the program EDAC[19] for a free standing WS_2 layer, given the lack of a specific adsorption configuration of WS_2 on Au(111) because of the lattice mismatch between the two (see the discussion about the XPD patterns of MoS_2 on Au(111) in chapter 3). The experimental results in figure 5.2 (a) and (b) on the WS_2 grown through uptake 2 show a three-fold symmetry; assuming that the Au substrate has an irrelevant influence on the symmetry of the pattern and considering that the WS_2 structure is three-fold symmetric (see sketch in figure 5.2 (d)), the three-fold pattern is ascribable to the presence of one single orientation.

To validate the assignment of the peaks in the S $2p_{3/2}$ XPS spectrum in figure 5.1 (f), i.e. the component at higher BE belongs to the bottom S, we used the XPD pattern for the component at higher BE and we compared it to XPD simulations performed for both top and bottom S, assuming a lattice parameter of 3.15 Å and an S-W interlayer distance of 1.57 Å, as found in the literature[20], obtaining a good agreement between the experimental data and the simulation done for the bottom S reported in figure 5.2 (a). In addition, the bottom S pattern is useful for the determination of the polytype of the layer because, with a photon energy of 560 eV, the XPD is dominated by forward scattering processes involving the W atoms, directly giving the orientation of the bottom sulfur layer with respect to the W and top S atoms. In order to verify the polytype of SL WS_2, we compared the bottom S pattern (figure 5.2 (a)) with the 1H and 1T structure simulations performed with the same kinetic energy of 397 eV, reported in figure 5.2 (a) and (c), respectively, finding that single layer WS_2 has a trigonal prismatic phase. Consequently, the simulation for the W 4f pattern was done for a 1H free-standing layer, oriented as sketched in figure 5.2 (d) and the minimum R-factor was obtained for a lattice parameter of 3.15±0.02 Å and a S-W interlayer distance of 1.57±0.03 Å, in agreement with the values reported in literature[20].

In order to determine the absolute orientation of the substrate, we first measured the XPD pattern of the clean Au(111) substrate at high kinetic energy, in order to enhance forward scattering and probe the bulk component (5.2 (e)). The simulation was performed on a bulk terminated Au(111) cluster consisting of four layers oriented as depicted in figure 5.2 (f). The comparison between the XPD patterns of the overlayer and the substrate allowed us to find out the relative orientation of the WS_2 layer with respect to the gold substrate. Interestingly, the orientation results to be the same as that of MoS_2 on Au(111) (see figure 3.12 (a)), suggesting that the symmetry of the gold substrate plays the main role in steering the adlayers towards a preferential orientation. Though there is a clear evidence of this fact, theorethical calculations would provide a valuable insight into the reasons of this particular orientation.

In order to collect quantitative information about the percentage of the

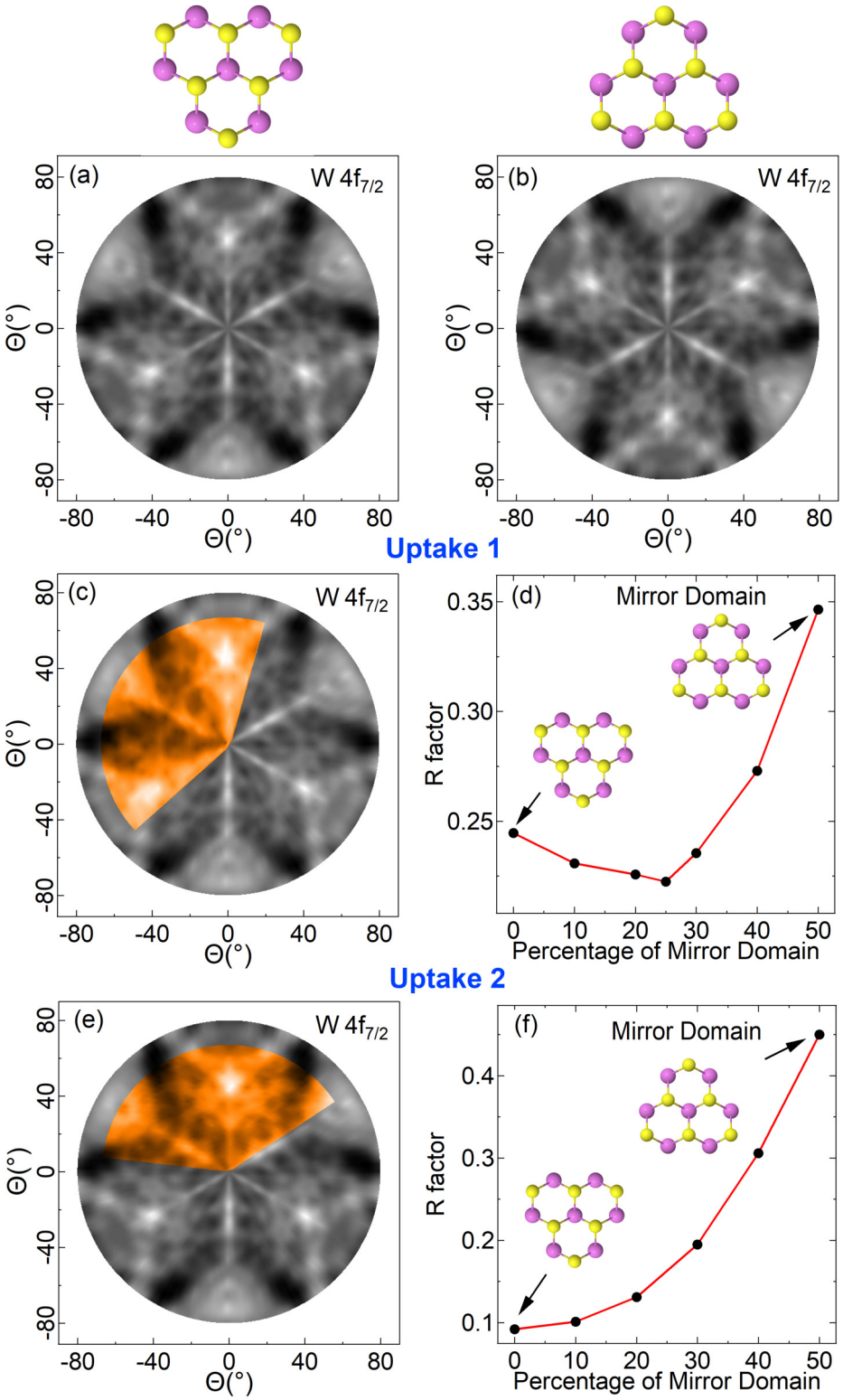

Figure 5.3: Simulated W 4f pattern (E_k=324 eV) for one orientation (a) and for the mirrored orientation (b). Stereographic projections of the integrated photoemission intensity modulation I(θ, ϕ) as a function of emission angle for W 4f (c) uptake 1 and (e) uptake 2 (hν=360 eV; E_k ~324 eV). R-factor behavior for the W $4f_{7/2}$ diffraction patterns, as a function of the relative concentration of twin domains for (d) uptake 1 and (f) uptake 2.

mirror domain in uptake 1 and uptake 2 grown WS_2, XPD patterns of the two oppositely oriented domains were simulated and they are reported in figure 5.3 (a) and (b). As they are originated by two identical but oppositely oriented structures, they present the same features rotated by 180°. We then performed XPD measurements on the uptake 1 sample. The result for W $4f_{7/2}$ core level hν=360 eV (324 eV kinetic energy) is reported in figure 5.3 (c), compared with the analogue at the same kinetic energy on uptake 2 sample in figure 5.3 (e). The degree of mixture of the two orientations was optimized in both cases such that the agreement between experiment and simulation was maximized. Figure 5.3 (d) and (f) show the result of this optimization for the two cases: the R-factor is displayed as a function of the mirror domain admixture. For uptake 1, we find the best agreement between simulation and experimental data when the ratio between one domain and its mirrored is close to 3:1, whereas for uptake 2, a single domain orientation gives the minimum R-factor. In both cases, the R-factor is low, consistent with the excellent agreement between experiment and simulation.

Indications of the single orientation and the mixture of oppositely oriented domains depending on the growth procedure can also be found in the LEED patterns, reported in figure 5.4 for uptake 1 (a) and uptake 2 (b). The most intense spots correspond to the reciprocal lattice of the WS_2, while the first order Au(111) diffraction spots form a hexagon with the same orientation of WS_2 but a larger size, due to the difference of lattice constant between Au ($\alpha_{Au} \sim 0.288\,nm$) and WS_2($\alpha_{MoS_2} \sim 0.315\,nm$)[20]. This lattice mismatch results in a moiré superstructure, which can be observed in the LEED pattern, as it happens for other systems[21, 22], and this extra periodicity leads to the formation of additional moiré induced reciprocal lattice points, arranged in a hexagonal pattern. However, due to the low coverage of the sample, the moiré spots are not well visible. Dendzik et al. report that these extra features, present also for slightly lower coverages (0.3 ML), disappear when the coverage is ∼0.15 ML[12] and this absence is explained by the fact that the growth starts with the formation of small islands[1] that are too small to have sufficient full moiré periods that lead to defined diffraction spots. Moreover, the absence of additional diffraction features rotated with respect to the Au spots indicates that for both uptakes the WS_2 unit cell is aligned parallel with the unit cell of the substrate, in agreement with the previous findings[12].

Comparing the two LEED patterns, one can note that the intensity of some WS_2 spots are more intense than others. This evident asymmetry, which is on average stronger for uptake 2, as it is clearly visible in figure 5.4 (c) from the line profile analysis of the spots along the colored rings containing the WS_2 spots, would not be expected for an equal distribution of domain orientations. Indeed, from the XPD measurements, we know that for uptake 1, the mirror domain is also present, whereas for uptake 2, only one domain is present.

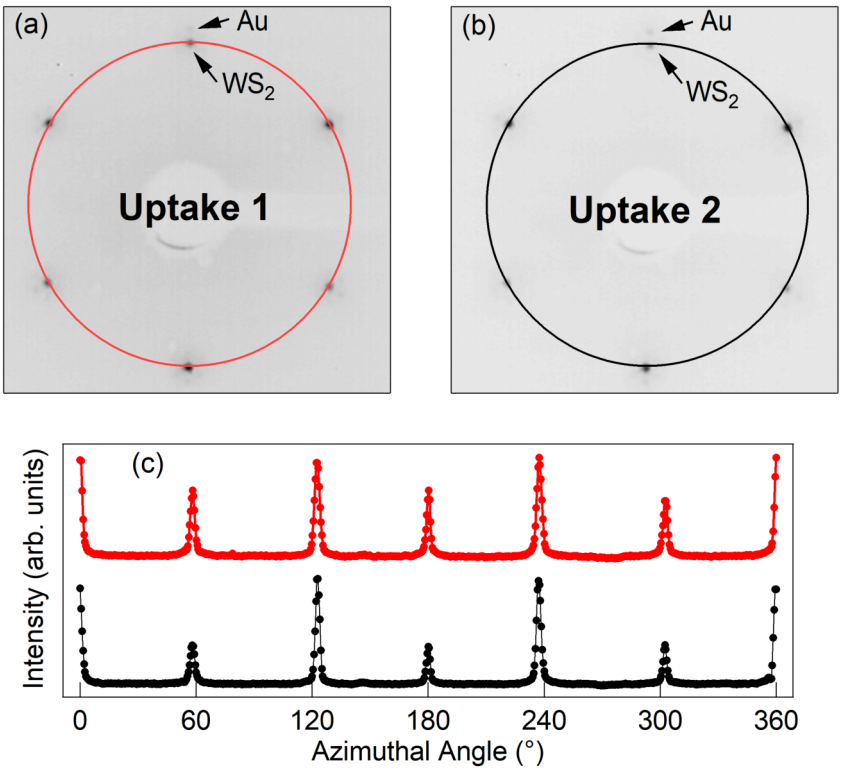

Figure 5.4: LEED patterns measured at 78 eV for WS_2 synthesized according to (a) uptake 1 and (b) uptake 2. (c) The symmetry of the patterns is shown by the line profile analysis along the colored rings containing the WS_2 spots in (a) and (b) with red and black lines, respectively.

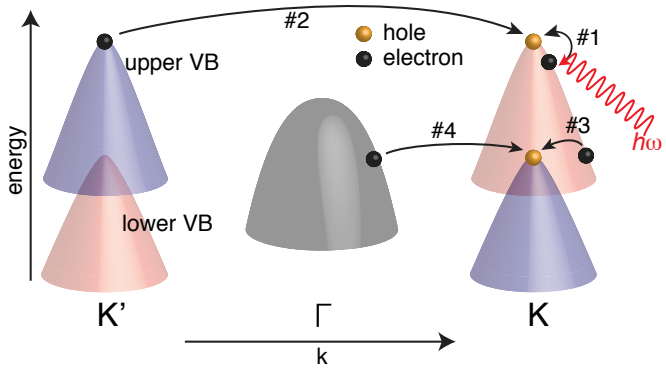

Figure 5.5: Schematic valence band for SL WS_2 with the absolute valence band maxima at K and K' and a local maximum at Γ. The VB at K and K' are spin-split with the color indicating the spin direction. The VB at Γ is spin degenerate. El-ph scattering processes to fill holes at the top of the spin-split band are illustrated. $\hbar\omega$ is the phonon absorbed in process # 1. Adapted from[7]

5.3.3 ARPES measurements

As already mentioned in the introductive part of this chapter, the spin-valley coupling in the valence band at the K-point of the Brillouin zone makes SL WS_2 a promising candidate for spin-valleytronic applications also thanks to the fact that allows for larger electron/hole life-times if compared with other SL materials such as graphene[8–10], MoS_2[2, 3]. In fact, once a spin-valley polarized carrier is created, i.e. a carrier with a given spin and valley index, it can undergo both elastic and inelastic scattering events that, in the time scale of few femto-seconds[4, 23], can restore a thermal-equilibrium condition. In the case of a SL WS_2 without dopant impurities and defects, one can fairly assume that scattering events are mainly assisted by phonons, which are due to lattice vibrations of the atoms with respect to the rest position, therefore a quantitative assessment of the electron-phonon (el-ph) interaction described in this section can be of extreme interest for real device applications.

The sample used for this analysis is that grown through the uptake 2 method since we already demonstrated its single domain orientation and its high crystalline quality. In order to investigate such interactions as reported in reference [7], we used ARPES technique described in Chapter 2, that allows for the simultaneous detection of energy and momentum, namely the energy band dispersion. In particular, by taking a cut along a given k-value, one obtains the so-called energy distribution curve (EDC) and from the linewidth of the spectral lines one can derive the electron-hole life-time (relaxation time)[24].

Figure 5.5 shows a sketch of the WS_2 band structure where are visible the two spin-splitted VB maxima at K and K' symmetry points, with an energy difference of 0.42 eV[12], that, for a matter of clarity will be hereon

referred to as "upper" (for the higher energy band) and "lower" (for the lower energy band). Moreover, it is also reported a spin-degenerate band at the Γ-point (due to time reversal symmetry) with the top of the band 0.22 eV below the upper VB at K-point[12]. The holes created by the photoemission process during ARPES can be filled by electrons thanks to an exchange of both energy and momentum provided by phonons. As shown in figure 5.5, there are several phonon scattering mechanisms and the different possible scenarios as described below. In the case of a hole created close to the top of the upper VB, only electrons that have a lower or equal kinetic energy can fill that vacancy. Moreover, it should be noted that, thanks to the spin flipping at the K and K' point, only few transitions are likely to happen. In particular, electrons belonging to the same upper band can be assisted by an intravalley-phonon scattering mechanism, through a phonon absorption, that can provide the missing energy and momentum to support the transition (#1). Alternatively, one electron belonging to the K' upper VB can elastically scatter and fill the hole in K (#2), but this requires a combination of a large momentum and a spin-flipping since the upper K and K' valleys have reversed spin. Therefore, this latter transition is supposed to be unfavorable because of the last requirement on the spin[25], as well as the transition from K (K') to K' (K) with a lower initial kinetic energy (inter-valley scattering assisted by phonon absorption). In addition, also the transitions from the Γ VB are not likely to happen even if the constraints relative to the spin of the scattered electron are satisfied (Γ valley is in fact spin degenerate), because they require phonons with energy that exceed the separation energy between the Γ VB and the upper bands of 220 meV. In fact, being the Fermi level well above the upper bands (see figure 5.6 (a)), all the electronic states in that energy window are full, therefore multiple electron-phonon-scattering mechanisms that could lead an electron from Γ to K (or K') are forbidden, since the maximum expected phonon energy in this system is ≈ 55 meV[26].

On the other hand, phonon-promoted processes that lead to the filling of holes in the lower VB are several more. In fact, it is found that the spin polarization of the K (K') VB is very strong only exactly at the K-symmetry points, whereas it decreases far from it[3]. Therefore, it is likely that electrons from the upper K band scatter through a phonon-emission or phonon-absorption process to fill the hole (#3). The same process is allowed from the Γ band through either the absorption or emission of a phonon. Therefore, based on this analysis, we expect a stronger el-ph coupling in the lower VB than in the upper thus leading to wider linewidth for the lower bands.

Figure 5.6 (a) shows the experimental VB structure close to the K point, with the two narrow and well separated spin-orbit branches of the VB, originated by the in-plane d-orbitals of W. The nearly parabolic dispersion is discontinued by a kink-like deviation at energies of 174±14 meV and 124±18 meV below the top of the upper and lower VB branches, respectively. To

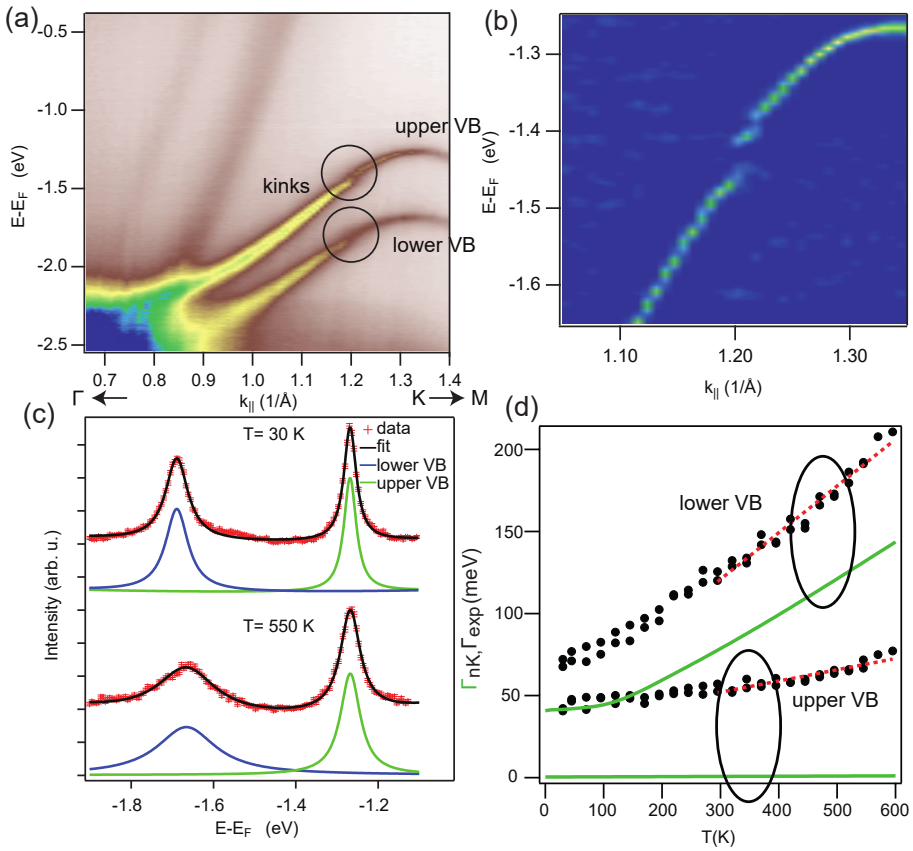

Figure 5.6: (a) Band dispersion along the Γ -K direction measured at 30 K. The black circles mark the position of the kinks. (b) Curvature[27] of the photoemission data reported in (a), showing the kink of the upper band. (c) EDCs acquired through K point at low and high temperature. (d) Lorentzian linewidth of the bands in an EDC curve through K (markers) as a function of the temperature. The green solid lines are the calculated temperature-dependent linewidth for the spin-orbit bands at K. The red dashed lines are a fit of the experimental data at high temperature. Adapted from reference[7]

analyze this behavior, figure 5.6 (b) shows a magnification of the kink in the upper band revealing the presence of a gap. This has been ascribed to the moiré superstructure formed by the WS_2 that opens a mini-gap close to the K-symmetry point of the Brillouin zone[7].

In addition, the moiré pattern might influence the measured spectral function by generating band replicas, that might affect the determined width of the energy dispersion curves. In our data no replicas were observed, situation quite different from graphene/Ir(111), where replica bands are visible[28]. ARPES measurements give also a further proof that the sample is single layer, indeed, we observe a degenerate valence band in Γ (not reported here) with a binding energy higher than the upper VB at K.

The effect of the el-ph coupling on the two spin-split branches is determined by analyzing the energy distribution curves (EDC) through the K point. Specifically, a small angle scan around the K point ($\pm 0.1 Å^{-1}$) was taken at each temperature in ascending and descending series. Figure 5.6 (c) shows a comparison between spectra taken at 30 K and 550 K. The broadening of the peaks with the increased temperature, especially for the lower VB, is a signature of an increased temperature-dependent scattering that, at least qualitatively, well agrees with the interpretation described above based on the el-ph scattering.

In order to obtain a quantitative assessment of such broadening, figure 5.6 (d) reports the spectral linewidths versus a wide range of temperatures, obtained through a fitting of the EDC curves with a polynomial background and two Lorentzian peaks. The almost linear behavior with the increased temperature is a clear signature of the el-ph coupling, since at high temperature the squared matrix element for the electron-phonon scattering is a linear function of the temperature. To further support this argument, figure 5.6 (b) shows a comparison with theoretical linewidth calculations. These are based on the calculation of the imaginary part of the lowest order el-ph self-energy obtained within the framework of density functional theory ad described in detail in reference [7].

Despite the similar trends, there is a non negligible offset between experimental and simulation results. This can be ascribed to the contribution given by electron-electron interactions, as well as by electron-defect interactions not accounted in the theoretical model used for the simulations of figure 5.6 (d), that, however, are temperature independent.

As it was theoretically foreseen, the el-ph coupling strength in the spin-split valence band states at K in WS_2 is very different for the two bands. Because of the less strong el-ph coupling, holes in the upper band can be expected to have a very long life-time in contrast to the ones in the lower band.

5.4 Conclusions

In conclusion, in this chapter we demonstrated that by properly tuning the growth parameters, the procedure that was developed for the growth of single domain MoS_2 on Au(111) is also suitable for the growth of highly pure singly oriented domains of WS_2 on Au(111). This system was characterized by HR-XPS, gaining information about the quality of the layer, as presulfided species were not detected. The LEED and the XPD measurements exhibit 3-fold symmetry which is consistent with the presence of only one single orientation of the WS_2 layer. Finally, ARPES measurements were performed in order to study the electron-phonon coupling, which strength is drastically different in the spin-split VB states at the K point of the Brillouin zone.

References

[1] Fuchtbauer, H. G.; Tuxen, A. K.; Moses, P. G.; Topsoe, H.; Besenbacher, F.; Lauritsen, J. V. Morphology and atomic-scale structure of single-layer $WS2_2$ nanoclusters. *Physical Chemistry Chemical Physics* **2013**, *15*, 15971–15980.

[2] Xu, X.; Yao, W.; Xiao, D.; Heinz, T. F. Spin and pseudospins in layered transition metal dichalcogenides. *Nature Physics* **2014**, *10*, 343–350.

[3] Xiao, D.; Liu, G.-B.; Feng, W.; Xu, X.; Yao, W. Coupled Spin and Valley Physics in Monolayers of MoS_2 and Other Group-VI Dichalcogenides. *Physical Review Letters* **2012**, *108*, 196802.

[4] Mak, K. F.; He, K.; Shan, J.; Heinz, T. F. Control of valley polarization in monolayer MoS_2 by optical helicity. *Nature Nanotechnology* **2012**, *7*, 494–498.

[5] Mak, K. F.; McGill, K. L.; Park, J.; McEuen, P. L. The valley Hall effect in MoS_2 transistors. *Science* **2014**, *344*, 1489–1492.

[6] Zeng, H.; Dai, J.; Yao, W.; Xiao, D.; Cui, X. Valley polarization in MoS_2 monolayers by optical pumping. *Nature Nanotechnology* **2012**, *7*, 490–493.

[7] Hinsche, N. F. et al. Spin-dependent electron-phonon coupling in the valence band of single-layer WS_2. *Physical Review B* **2017**, *96*, 121402.

[8] Rycerz, A.; Tworzydlo, J.; Beenakker, C. W. J. Valley filter and valley valve in graphene. *Nature Physics* **2007**, *3*, 172–175.

[9] Xiao, D.; Yao, W.; Niu, Q. Valley-Contrasting Physics in Graphene: Magnetic Moment and Topological Transport. *Physical Review Letters* **2007**, *99*, 236809.

[10] Akhmerov, A. R.; Beenakker, C. W. J. Detection of Valley Polarization in Graphene by a Superconducting Contact. *Physical Review Letters* **2007**, *98*, 157003.

[11] Lehtinen, O.; Komsa, H.-P.; Pulkin, A.; Whitwick, M. B.; Chen, M.-W.; Lehnert, T.; Mohn, M. J.; Yazyev, O. V.; Kis, A.; Kaiser, U.; Krasheninnikov, A. V. Atomic Scale Microstructure and Properties of Se-Deficient Two-Dimensional $MoSe_2$. *ACS Nano* **2015**, *9*, 3274–3283.

[12] Dendzik, M.; Michiardi, M.; Sanders, C.; Bianchi, M.; Miwa, J. A.; Grønborg, S. S.; Lauritsen, J. V.; Bruix, A.; Hammer, B.; Hofmann, P. Growth and electronic structure of epitaxial single-layer WS_2 on Au(111). *Physical Review B* **2015**, *92*, 245442.

[13] Abrami, A. et al. Super ESCA: First beamline operating at ELETTRA. *Review of Scientific Instruments* **1995**, *66*, 1618–1620.

[14] Heimann, P.; van der Veen, J.; Eastman, D. Structure-dependent surface core level shifts for the Au(111), (100), and (110) surfaces. *Solid State Communications* **1981**, *38*, 595–598.

[15] Grønborg, S. S.; Ulstrup, S.; Bianchi, M.; Dendzik, M.; Sanders, C. E.; Lauritsen, J. V.; Hofmann, P.; Miwa, J. A. Synthesis of Epitaxial Single-Layer MoS_2 on Au(111). *Langmuir* **2015**, *31*, 9700–9706.

[16] Gao, Y.; Liu, Z.; Sun, D.-M.; Huang, L.; Ma, L.-P.; Yin, L.-C.; Ma, T.; Zhang, Z.; Ma, X.-L.; Peng, L.-M.; Cheng, H.-M.; Ren, W. Large-area synthesis of high-quality and uniform monolayer WS_2 on reusable Au foils. *Nature Communications* **2015**, *6*, 8569–8579.

[17] Shpak, A.; Korduban, A.; Kulikov, L.; Kryshchuk, T.; Konig, N.; Kandyba, V. XPS studies of the surface of nanocrystalline tungsten disulfide. *Journal of Electron Spectroscopy and Related Phenomena* **2010**, *181*, 234–238.

[18] Woodruff, D. Adsorbate structure determinationusing photoelectron diffraction: Methods and applications. *Surface Science Reports* **2007**, *62*, 1–38.

[19] García de Abajo, F. J.; Van Hove, M. A.; Fadley, C. S. Multiple scattering of electrons in solids and molecules: A cluster-model approach. *Physical Review B* **2001**, *63*, 075404.

[20] Schutte, W.; Boer, J. D.; Jellinek, F. Crystal structures of tungsten disulfide and diselenide. *Journal of Solid State Chemistry* **1987**, *70*, 207–209.

[21] N'Diaye, A. T.; Coraux, J.; Plasa, T. N.; Busse, C.; Michely, T. Structure of epitaxial graphene on Ir(111). *New Journal of Physics* **2008**, *10*, 043033.

[22] Orlando, F.; Lacovig, P.; Omiciuolo, L.; Apostol, N. G.; Larciprete, R.; Baraldi, A.; Lizzit, S. Epitaxial Growth of a Single-Domain Hexagonal Boron Nitride Monolayer. *ACS Nano* **2014**, *8*, 12063–12070.

[23] Wang, Q. H.; Kalantar-Zadeh, K.; Kis, A.; Coleman, J. N.; Strano, M. S. Electronics and optoelectronics of two-dimensional transition metal dichalcogenides. *Nature Nanotechnology* **2012**, *7*, 699–712.

[24] Calandra, M.; Mauri, F. Electron-phonon coupling and electron self-energy in electron-doped graphene: Calculation of angular-resolved photoemission spectra. *Physical Review B* **2007**, *76*, 205411.

[25] Fabian, J.; Das Sarma, S. Phonon-Induced Spin Relaxation of Conduction Electrons in Aluminum. *Physical Review Letters* **1999**, *83*, 1211–1214.

[26] Molina-Sánchez, A.; Wirtz, L. Phonons in single-layer and few-layer MoS_2 and WS_2. *Physical Review B* **2011**, *84*, 155413.

[27] Zhang, P.; Richard, P.; Qian, T.; Xu, Y.-M.; Dai, X.; Ding, H. A precise method for visualizing dispersive features in image plots. *Review of Scientific Instruments* **2011**, *82*, 043712.

[28] Pletikosić, I.; Kralj, M.; Pervan, P.; Brako, R.; Coraux, J.; N'Diaye, A. T.; Busse, C.; Michely, T. Dirac Cones and Minigaps for Graphene on Ir(111). *Physical Review Letters* **2009**, *102*, 056808.

Chapter 6

Study of oxygen adsorption on Ir(111) and its intercalation under graphene grown on Ir(111)

6.1 Introduction

After the isolation of graphene, the research focused on its growth on different substrates. The synthesis of graphene on transition metals has been deeply investigated in particular by using chemical vapour deposition (CVD) that consists in exposing the metal surface to gaseous hydrocarbon precursors which decomposition provides atomic carbon. A large number of metal/graphene interfaces have been successfully studied and several reviews have been written[1–3]. The choice of the metal is a critical issue because it determines the magnitude of the interaction between graphene and the substrate. Indeed, if the coupling between graphene and the substrate is very strong, as in the case of Ru(0001)[4], Rh(111)[5] and Re(0001)[6], the graphene-like properties are not preserved. For example, in the case of Ni(111), the interaction is so strong that the electronic structure of graphene is perturbed in such a way that the linear band dispersion of graphene is lost[7]. Conversely, i.e. when graphene poorly interacts with the substrate, as for Pt(111)[8] and Pd(111)[9], the epitaxial growth leads to a non-ordered graphene domains with different orientations and domain boundaries. Therefore, high structural quality is difficultly achieved on these substrates.

One solution that has been intensively studied, in order to obtain highly ordered graphene with its electronic structure preserved, is to use a substrate that allows sufficiently strong interaction with graphene, and subsequently decouple it from the metal surface by intercalation of metals[5, 7, 10], silicon[11], or atoms like hydrogen[12], fluorine[13] and oxygen[14, 15].

One substrate that gained a lot of attention in this perspective is Ir(111). Indeed, the coupling with graphene is strong enough to allow the large scale growth of perfectly aligned graphene[16], but is sufficiently weak to preserve the band structure of freestanding graphene, although with the rise of a moiré superstructure that affects the valence band structure with the presence of replica bands and minigaps near the Fermi level. One effective intercalant for the decoupling of graphene from Ir(111) is oxygen, that works not only for incomplete monolayers or islands[17], but also for a complete graphene layer[18, 19].

In this framework this chapter addresses the topic of the oxygen adsorption on Ir(111), the structures that oxygen can form on Ir and the possible role played by graphene on the adsorption of the intercalated oxygen at the graphene-Ir(111) interface. Martines-Galera et al. found that, depending on the dosing conditions, i.e. O_2 pressure, sample temperature and the duration of the O_2 exposure, different oxygen superstructures such as O-(2x2), O-($\sqrt{3}$x$\sqrt{3}$)-R30°, O-(2x1) and O-($2\sqrt{3}$x$2\sqrt{3}$)-R30° form for the oxygen intercalated graphene/Ir(111) system, with the maximum coverage of 0.5 ML[20]. On the contrary, Larciprete et al. found that the oxygen coverage below graphene can be higher than 0.6 ML[18]. On the other hand, Bianchi et. al showed that on the bare Ir(111) surface, dosing oxygen at low temperature, a maximum coverage of 0.38 ML can be reached, which structure consists of patches of O-(2x2) and O-(2x1) superstructures on the surface[21]. However, by dosing oxygen at room temperature on the clear Ir(111) surface, Marinova et al. found a coverage of 0.52 ML[22].

In this chapter we experimentally demonstrate for the first time that the oxygen coverage limit of 0.5 ML can be exceeded, up to 0.66 ML, on both clean Ir(111) and under graphene grown on Ir(111), obtaining the same superstructure 2O-($\sqrt{3}$x$\sqrt{3}$)-R30° and proving that no changes in the adsorbate-substrate interaction occur due to the presence of graphene cover, as claimed in previous studies[18, 20]. We found that, while the maximum oxygen coverage under graphene is achieved dosing molecular oxygen, in order to obtain 0.66 ML coverage on bare Ir(111), it is necessary to use a strongly oxidizing molecule such as NO_2. In addition, while it was demonstrated through DFT calculation that oxygen adsorbs in the fcc-hollow sites on bare iridium[23], this was not proved for oxygen under graphene. Here, we also show by means of XPD measurements that the adsorption site of oxygen under graphene is the fcc-hollow sites.

6.2 Experimental details

The Ir(111) substrate was cleaned by repeated cycles of Ar^+ sputtering and annealing up to 1070 K. The sample quality was checked by XPS and no contaminants were detected. The Ir $4f_{7/2}$ core level showed the core level

shifted component typical of the clean surface[21]. The long-range order was verified by acquiring LEED patterns on the prepared sample, showing a hexagonal (1x1) pattern. Oxygen adsorption on clean Ir(111) was performed using two different precursors: O_2, dosed at 523 K with a O_2 pressure between 5×10^{-8} and 5×10^{-7} mbar for a total of 90 Langmuir (L); NO_2, dosed at 423 K for 30 minutes at a pressure of 1×10^{-7} mbar, with an overall exposure of 180 L. Graphene was grown on Ir(111) by performing six cycles of temperature programmed growth, dosing ethylene (C_2H_4) at 570 K and annealing at 1370 K[24]. Oxygen intercalation under graphene was achieved by dosing molecular oxygen with a home-made doser for 20 minutes at 473 K and 40 minutes at 423 K in a background pressure of 5×10^{-4} mbar. The doser consists of a molybdenum tube of 6 mm diameter, placed at less than half millimeter from the sample surface. Thanks to this setup, we estimate that the pressure at the sample surface is at least one order of magnitude higher with respect to the background pressure. The HR-XPS spectra were measured at 77 K using a photon energy of 250 eV for the Ir 4f and 650 eV for the O 1s. The XPD patterns for the Ir $4f_{7/2}$ were acquired at $h\nu = 180$ eV ($E_k \sim 90$ eV). The patterns for the O 1s were acquired at $h\nu = 620$ eV ($E_k \sim 90$ eV). The XPD measurements for the C 1s were performed with photon energy $h\nu = 400$ eV corresponding to $E_k \sim 115$ eV.

For a more complete description of the experimental parameters, see chapter 2.10

6.3 Results and discussion

6.3.1 O_2 dose on Ir(111)

In order to have a complete set of measurements and compare the results with previous findings[19, 21], we firstly dosed molecular oxygen on the bare Ir(111) surface with a pressure of 1×10^{-7} mbar keeping the substrate at 523 K. Figure 6.1 reports the Ir $4f_{7/2}$ spectrum of the clean surface (a), and the spectrum collected after the oxygen dose, shown in (b). Both spectra were recorded at a temperature of 77 K. As already known, the spectrum of the clean Ir(111) shows two components at 60.85 eV (IrB) and 60.33 (Ir0) eV BE, related to bulk and surface atoms, respectively[21], because the second layer cannot be distinguished from the bulk, differently from the case of the Ru(0001)[26]. The lineshapes for IrB and Ir0 are reported in table 6.1, and they slightly differ from the ones found by Bianchi, presumably due to the different conditions of measurements[21].

When oxygen is dosed, the clean surface component Ir0 clearly decreases and two new components Ir1 and Ir2 appear at 60.64 eV and 61.15 eV BE, respectively. From previous works, we can directly assign them to the surface Ir atoms that are bound to one (Ir1, light blue ball in figure 6.3) or two oxygen atoms (Ir2, purple ball in figure 6.3)[18, 19, 21]. The line shape used for the

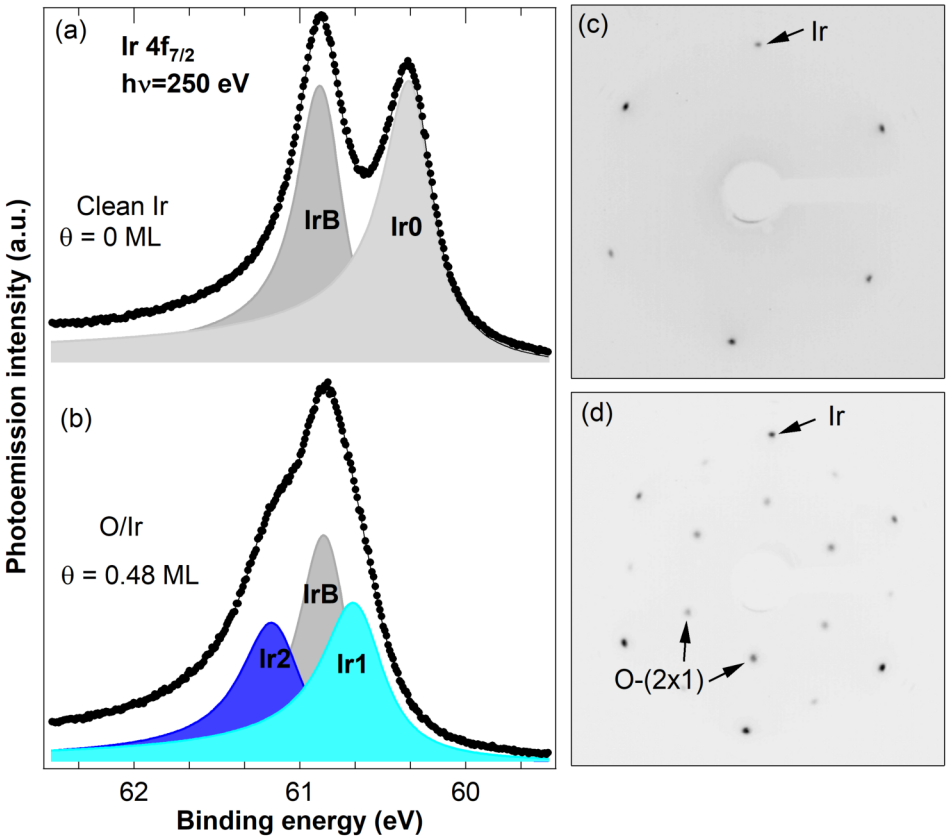

Figure 6.1: Ir $4f_{7/2}$ core level spectra measured at hν=250 eV photon energy for (a) the clean surface and (b) for a 0.48 ML of oxygen coverage obtained by dosing ~90 L of molecular oxygen. IrB is the bulk component, Ir0 is the clean surface peak, Ir1 is the surface component relative to the Ir atoms bound to one oxygen atom, Ir2 is the surface component relative to the Ir atoms bound to two oxygen atoms. The dots represent the experimental results, while the solid line in between is the fit. LEED patterns at 71 eV for (c) bare Ir(111) and (d) after O_2 dose. The O-(2x1) spots are marked by arrows and, due to the presence of 120° oxygen rotated domains, the LEED pattern shows an apparent O-(2x2) structure[25]. The XPS spectra and the LEED patterns were measured at a temperature of 77 K.

Ir1 and Ir2 components are reported in table 6.1 and will be discussed later.

In order to calculate the oxygen coverage θ from the Ir $4f_{7/2}$ XPS spectrum, one can normalize the intensities of the Ir $4f_{7/2}$ surface components (Ir0, Ir1 and Ir2) to the total surface intensity (Ir0+Ir1+Ir2) obtaining the coverages θ_0, θ_1 and θ_2 and, taking into account that the oxygen coverage is one third of the sum of the coverages of the surface atoms, each multiplied by their number of bonds, one can use the formula[19]

$$\theta_{Ox} = 1/3 \cdot (0 \cdot \theta_0 + 1 \cdot \theta_1 + 2 \cdot \theta_2). \tag{6.1}$$

It must be stressed this method might suffer of some errors, that is Ir1 and Ir2 intensities can be affected by photoelectron diffraction effects. From the deconvolution of the Ir $4f_{7/2}$ peak, and according to the above expression, we obtained a coverage of 0.48 ML, where one monolayer is defined with respect to the Ir surface atom density (1.56×10^{15} atoms/cm^2), in agreement with the maximum obtainable coverage with a O_2 dose of 0.5 ML reported in the literature[22, 25].

In order to determine and compare the ordered structures that oxygen forms on bare Ir(111), we acquired LEED measurements. Figure 6.1 (c) reports the LEED pattern of the bare Ir(111) surface, after the cycles of sputtering and annealing, acquired at 71 eV electron energy. The sharp spots are arranged in an hexagonal pattern, reflecting the six-fold symmetry of the Ir(111) surface. This pattern will be used to identify the spots belonging to the substrate during the following LEED measurements after the oxygen dose. The spots distribution in figure 6.1 (c), after the dose of 90 Langmuir (L) of molecular oxygen keeping the substrate at 523 K , suggest the formation of an O-(2x2) superstructure. However, based on the XPS analysis described before and shown in figure 6.1 (b), the apparent O-(2x2) structure can only come from the superposition of three O-(2x1) domains rotated by 120°, corresponding to a θ=0.5 ML coverage of oxygen on Ir(111)[22, 25, 27, 28], in agreement with the coverage calculated by means of the Ir $4f_{7/2}$ spectrum components.

6.3.2 NO_2 dose on Ir(111)

Since the attempt to increase the coverage of 0.5 ML by using molecular oxygen even with prolonged oxygen dose was not successful, we changed the oxygen source. One strongly oxidizing molecule, that has been already used to enhance the coverage on Ru(0001) up to 1 ML[29, 30] and Pd(111)[31] is nitrogen dioxide (NO_2). Indeed, NO_2 dissociation requires only one adsorption site per molecule[32], differently from molecular oxygen that needs two adjacent free sites[33]. It is evident that, above a certain coverage, the probability of finding two neighboring sites becomes low, setting a limit to the maximum coverage obtainable through molecular oxygen dosing. For

this reason, NO_2 was dosed at 423 K for 30 minutes at a pressure of 1×10^{-7} mbar.

Figure 6.2 reports the O 1s and the Ir $4f_{7/2}$ XPS spectra measured at 77 K after the NO_2 dose and after several annealings, that allowed us to stepwise remove oxygen atoms from the surface, to analyze the possible configurations of oxygen on the Ir(111) surface. Starting from the O 1s series of spectra reported on the left side of the figure, one can note that the intensity of the O 1s peak decreases with decreasing oxygen coverage, and a shift of 200 meV at higher BE occurs above 513 K annealing. The BE of the Ir atoms bound to one and two oxygen atoms and of the O 1s peak are reported in table 6.2. The O 1s peak series was used to calculate the oxygen coverage differently with respect to the previous case of O_2 dosed on Ir(111). Indeed, assuming that the top O 1s spectrum corresponds to 0.66 ML coverage (see next paragraph about the Ir $4f_{7/2}$ spectra series for the calculation of the coverage) and that at 0 ML coverage the intensity of the oxygen peak must be zero, we assume a linear behavior of the oxygen peak intensity with respect to the oxygen coverage and calculate the amount of oxygen on the surface. This method, compared to that based on the components of the Ir $4f_{7/2}$ spectrum, has the great advantage of avoiding the problems related to the diffraction effects on Ir1 and Ir2 components. Nevertheless, we find a good agreement between the values of coverage calculated with the two methods, meaning that diffraction effects are not important.

Looking at the right part of figure 6.2, where the Ir $4f_{7/2}$ spectra are reported, it is possible to see how the Ir component intensities change while annealing the sample. The first spectrum belongs to the as dosed sample and can be fitted with two components, centered at 61.11 eV and 60.82 eV BE, attributed to the iridium bound to two oxygen atoms (Ir2) and the bulk (IrB), respectively. From this fitting, using the formula 6.1, we calculated a coverage of 0.66 ML. This spectrum is also of extreme importance to extract the line shape for the Ir2 component, as the bulk is already known from the clean iridium spectrum and no other components are present. The fitting parameters are reported in table 6.1; one can note that the Lorentzian parameter of Ir2 is much broader than that of Ir0, while the Gaussian broadening is comparable for the two components.

Immediately after the first annealing, the Ir2 component decreases and finally disappears in spectrum (g), while the Ir1 component appears and it increases up to the spectrum (f) in figure 6.2. As Ir1 is the predominant surface component in the two spectra (f) and (g), they can be used to extract the line shape of this component. From the fitting, it comes out that the line shape of Ir1 is similar to that of the Ir2 component. Finally, further annealing the system, the Ir0 component appears and its intensity increases as the coverage decreases.

The behavior of the surface components can be understood making some considerations about the structures that oxygen forms on the Ir(111) surface.

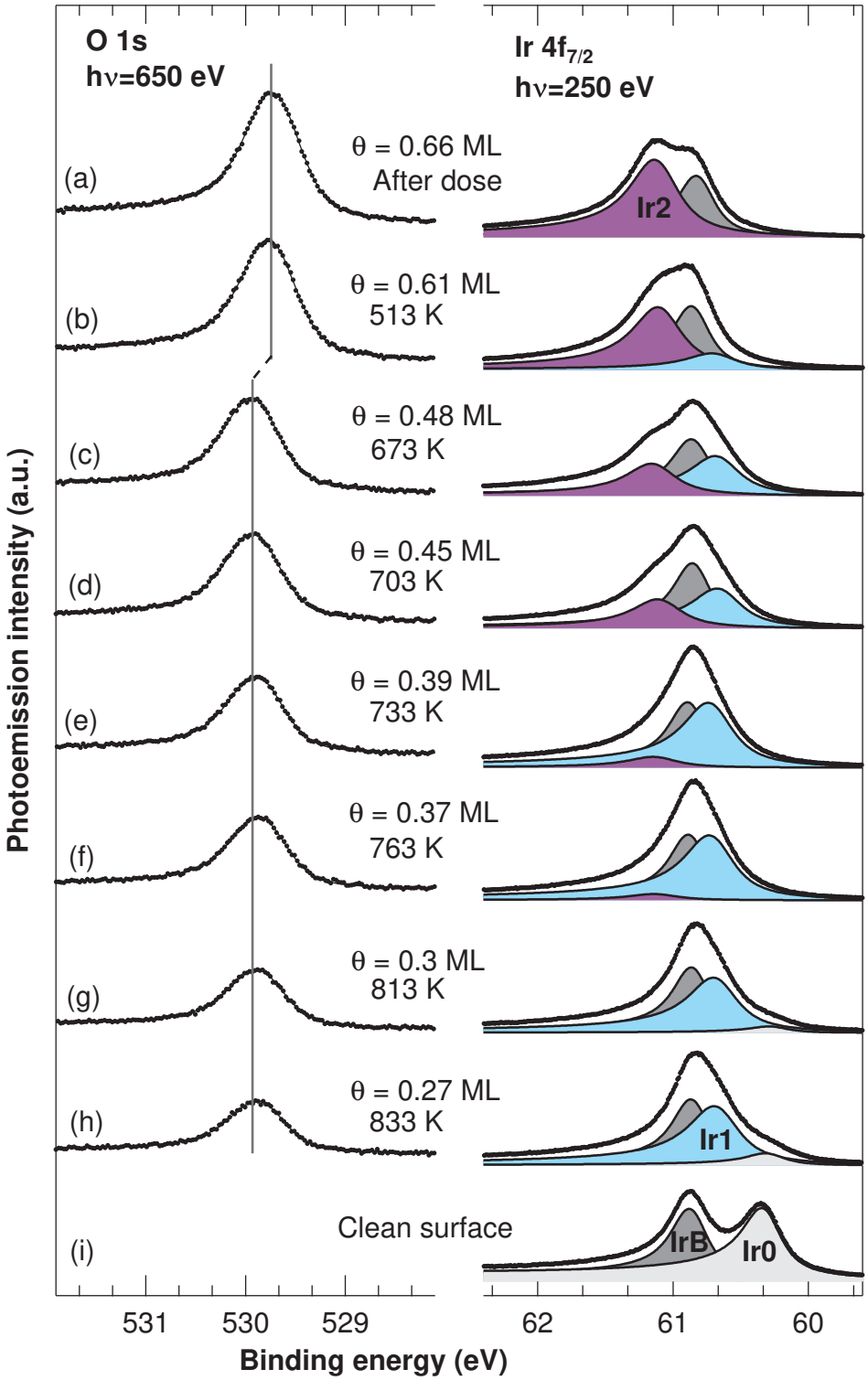

Figure 6.2: O 1s (left), measured at hν=650 eV photon energy, and Ir $4f_{7/2}$ (right), at hν=250 eV photon energy, core level spectra for maximum coverage (a) and different oxygen structures after annealing at (b) 513 K (c) 673 K, (d) 703 K, (e) 733 K, (f) 763 K, (g) 813 K, (h) 833 K. (i) Ir 4f spectrum for the clean surface. The dots represent the experimental results, while the line in between is the fit. The spectra were measured at a temperature of 77 K. The oxygen coverage θ was calculated from the O 1s intensity, as explained in the text.

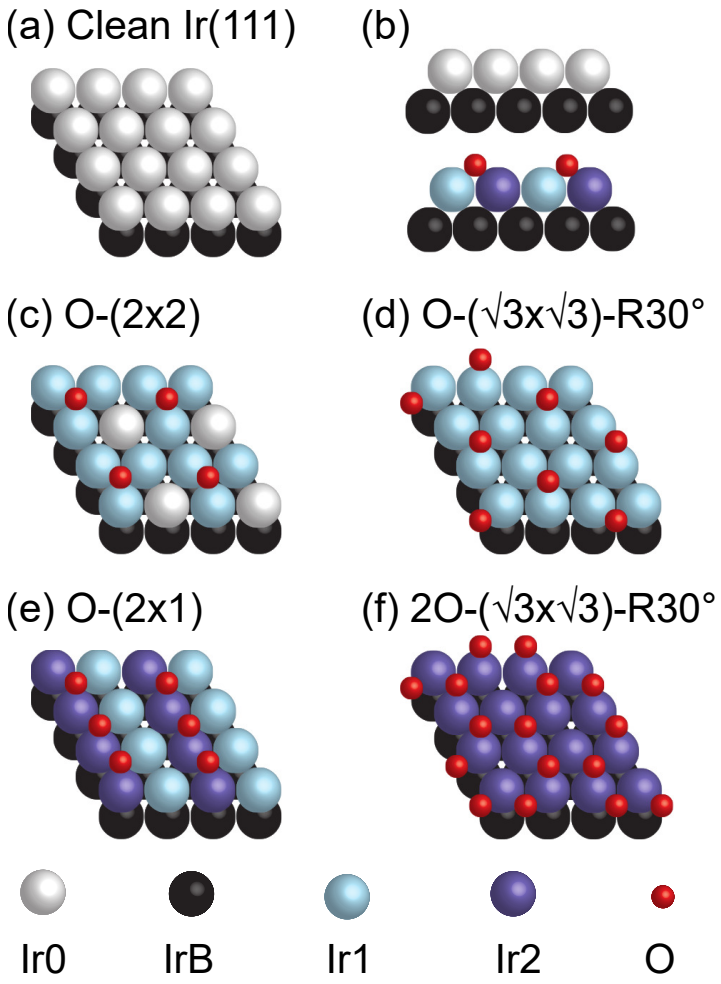

Figure 6.3: Oxygen adlayer structures on Ir(111) surface with increasing coverage with the oxygen atoms adsorbed always in three-fold fcc adsorption sites. Ir0, Ir1 and Ir2 are the first layer Ir atoms bound to no, one and two oxygen atoms, respectively. The bulk IrB includes the second and all deeper layers of Ir atoms.

Table 6.1: Doniach-Šunjić line shape parameters for the different components for Ir $4f_{7/2}$ core level at 250 eV photon energy and O 1s core level at 650 eV photon energy, acquired at 77 K. L is the Lorentzian width, α is the asymmetry parameter and G is the Gaussian width (see section 2.1.2 for detailed information).

Components	L(eV)	α	G(eV)
IrB	0.24	0.13	0.13
Ir0	0.26	0.20	0.11
Ir1	0.34	0.16	0.14
Ir2	0.35	0.13	0.14
O 1s	0.26	0.15	0.46

Table 6.2: BE positions of Ir1 and Ir2 components for Ir $4f_{7/2}$ core level acquired at 77 K with 250 eV photon energy, and BE position of the O 1s core level spectrum acquired at 77 K with 650 eV photon energy, for the most significant oxygen coverages calculated as explained in the text.

θ	Ir1(eV)	Ir2(eV)	O 1s (eV)
0.66 ML	—	61.11	529.68
0.48 ML	60.66	61.13	529.89
0.37 ML	60.70	61.12	529.82
0.27 ML	60.67	—	529.84

It is known from the literature, and further proved by the XPD measurements presented in section 6.3.4, that oxygen adsorbs in the fcc-hollow sites of the Ir(111) surface[23, 33–35]. With this piece of information, we can propose the structures starting from the highest coverage of 0.66 ML. In this case, the only possible structure that can exist with all the Ir atoms bound to two oxygen atoms is the 2O-($\sqrt{3}$x$\sqrt{3}$)-R30°, as shown in figure 6.3 (f), where the oxygen is represented by small red balls and the iridium bound to two oxygen atoms by purple balls. All the other configurations at lower coverage (figure 6.3 reports only the most representative ones) present also iridium atoms bound to one (light blue balls) or zero oxygen atoms (light grey balls), and therefore the XPS spectra related to them would result in having also Ir1 or Ir0 components. It is interesting to notice that 0.66 ML was the maximum obtainable coverage, suggesting that three oxygen atoms cannot be coordinated to the same Ir atom, as they are not stable, differently from what happens for oxygen on Ru(0001)[26]. Keeping on removing oxygen atoms from the surface, a situation is present in which half of the iridium atoms are bound to one oxygen atom, the other half to two oxygen atom (figure 6.3 (e), corresponding to a O-(2x1) structure with 0.5 ML coverage.

It is worth noticing that in order to form this structure, part of the oxygen atoms needs to rearrange on the surface. A further removal of oxygen atoms from the surface leads to another rearrangement and the formation of a O-($\sqrt{3}$x$\sqrt{3}$)-R30° structure with only surface iridium atoms bound to one oxygen (figure 6.3 (d)). This structure corresponds to a coverage of 0.33 ML, and it is in agreement with the intensity of the Ir1 component in the Ir $4f_{7/2}$ spectra (f) and (g) in figure 6.2. Finally, the last low coverage structure is a O-(2x2), corresponding to a coverage of 0.25 ML (figure 6.2 (c)), where 1/4 of the surface is not bound to oxygen atoms.

In order to experimentally study the oxygen superstructures formed upon desorption from the 0.66 ML coverage structure and to validate the models just discussed, we monitored the surface changes notably through the XPS measurements of figure 6.2 but also through LEED measurements at low temperature (77 K). Figure 6.4 (a) shows the LEED pattern of the sample immediately after the NO_2 dose and it shows a sharp ($\sqrt{3}$x$\sqrt{3}$)-R 30° pattern. This structure can be attributed both to a O-($\sqrt{3}$x$\sqrt{3}$), as sketched in figure 6.3 (d) with an oxygen coverage of 0.33 ML or to a 2O-($\sqrt{3}$x$\sqrt{3}$), with an oxygen coverage of 0.66 ML, as sketched in figure 6.3 (f). Thanks to the Ir $4f_{7/2}$ spectrum, that can be fitted only with two components, bulk (IrB) and iridium coordinated to two oxygen atoms (Ir2), it is possible to attribute this pattern to the presence of 2O-($\sqrt{3}$x$\sqrt{3}$)-R 30° superstructure, corresponding to a coverage of 0.66 ML. We stress again that this coverage was never observed before for the oxygen adsorption on Ir(111). In addition, the ($\sqrt{3}$x$\sqrt{3}$)-R 30° structure was never detected and considered not likely to exist on bare Ir(111), while it was found when oxygen is intercalated under graphene, with a coverage of 0.33 ML[20].

After annealing at 513 K (figure 6.4 (b)), the LEED pattern changes and shows a mixture of ($\sqrt{3}$x$\sqrt{3}$)-R30° and apparent (2x2) structures, suggesting that oxygen partially desorbs and 2O-($\sqrt{3}$x$\sqrt{3}$) and O-(2x1) structures coexist on the substrate, with an overall oxygen coverage of 0.61 ML. Increasing the annealing temperature at 653 K (figure 6.4 (c)), the ($\sqrt{3}$x$\sqrt{3}$)-R30° pattern disappears and the (2x2) periodicity is well defined, suggesting a well ordered (2x1) oxygen overlayer (see figure 6.3 (d)) that is distributed in the three equivalent orientations, as also found out through STM measurements by Martinez-Galera et al.[20], with an oxygen coverage of 0.5 ML. Increasing further the temperature (figure 6.4 (d), (e), (f)), the LEED pattern gradually changes again into a ($\sqrt{3}$x$\sqrt{3}$)-R30° pattern (figure 6.4 (g)), suggesting the formation of a O-($\sqrt{3}$x$\sqrt{3}$) structure, correspondent to a coverage of θ=0.33 ML. The annealing at temperatures higher than 800 K (figure 6.4 (h)) leads to the formation of a blurred (2x2) pattern, corresponding to a O-(2x2) oxygen structure sketched in figure 6.3 (c), with a coverage of θ=0.27 ML, calculated by the corresponding Ir 4f and O 1s XPS spectra. However, the poor sharpness of the pattern points to a not well ordered system, with small patches of O-(2x2) structure.

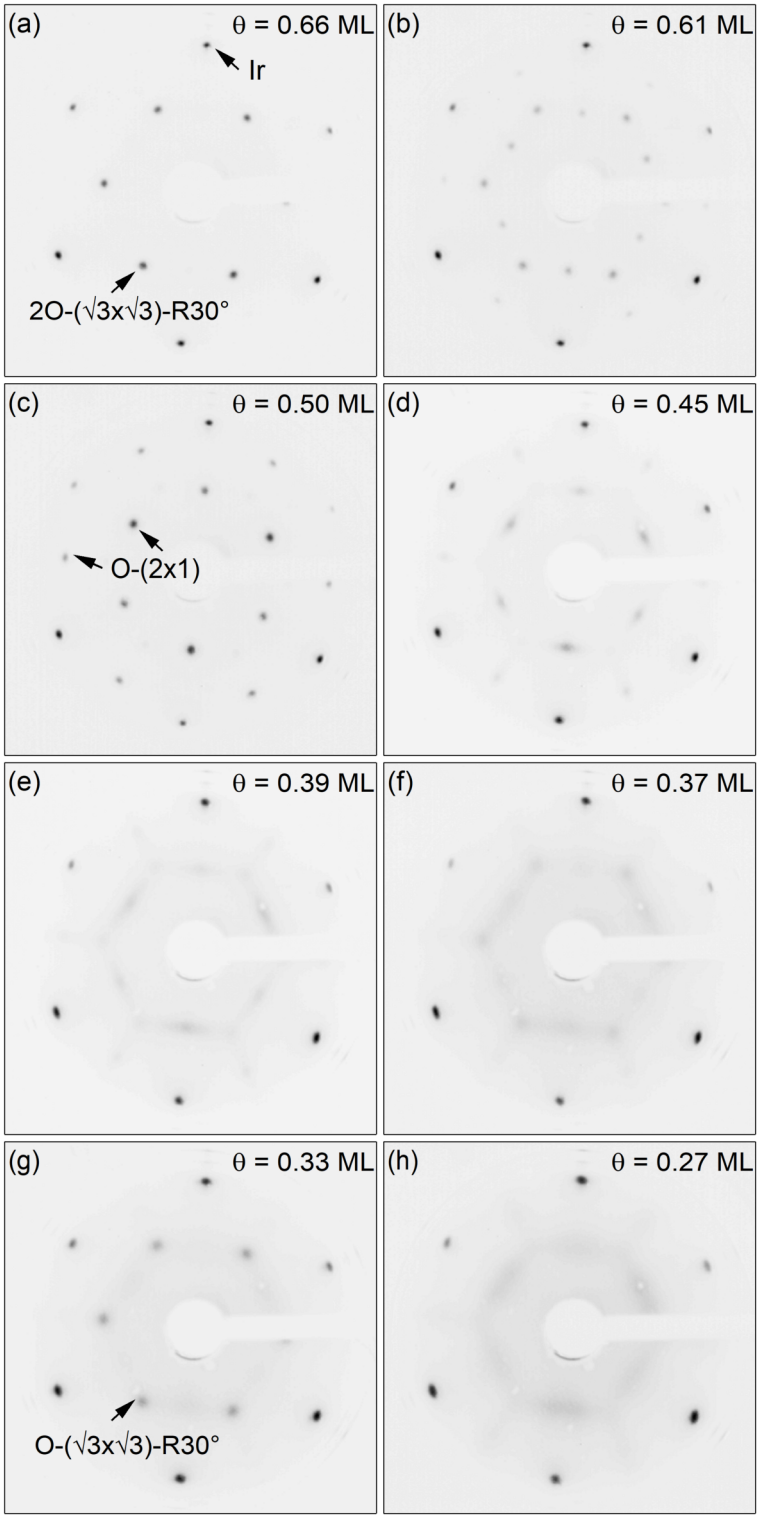

Figure 6.4: LEED patterns at 71 eV for oxygen adsorbed on Ir(111) after (a) NO_2 dose and after annealing at (b) 513 K, (c) 653 K, (d) 703 K, (e) 733 K, (f) 763 K, (g) 793 K, (h) 833 K. All the LEED patterns were acquired at 77 K. The oxygen coverage was calculated as for the measurements in figure 6.2.

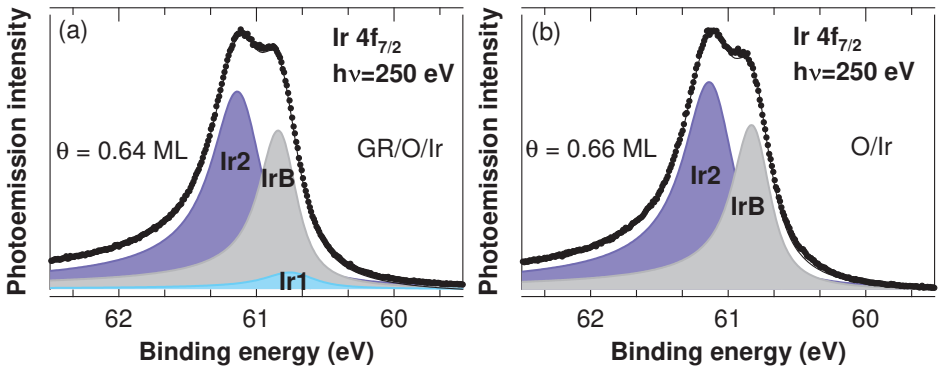

Figure 6.5: Ir $4f_{7/2}$ core level XPS spectra after (a) oxygen intercalation under graphene and (b) NO_2 dose on Ir(111) at 250 eV photon energy. The dots represent the experimental results, while the solid line in between is the fit. The spectra were measured at a temperature of 77 K. The components of the deconvoluted spectra IrB, Ir1 and Ir2 are added in the figure.

6.3.3 Oxygen intercalation under graphene grown on Ir(111)

The previous section showed for the first time that it is possible to reach an oxygen coverage of 0.66 ML on the bare Ir surface and described the formation of the 2O-($\sqrt{3}$x$\sqrt{3}$)-R30° structure. The aim of this section is to extend this study to the case of graphene over Ir(111) to understand if graphene plays a role in the adsorption of oxygen on Ir(111). Thus, a complete monolayer of graphene was grown on Ir(111) following a procedure reported in the literature[18], and oxygen intercalation was performed dosing molecular oxygen in a background pressure of 5×10^{-4} mbar for 20 minutes at 473 K and for 40 minutes at 423 K. It is known that intercalation occurs through the defects and the grain boundaries that are present before the oxygen exposure[36] and through the possible new defects caused by the oxygen itself[17].

Figure 6.5 (a) reports the Ir $4f_{7/2}$ spectrum acquired at 77 K with a photon energy of hν=250 eV after the intercalation of oxygen under graphene, together with the spectrum of the maximum coverage of oxygen on bare Ir(111) for a direct comparison (figure 6.5 (b)). The former can be fitted with three peaks centered at 60.65 eV, 60.82 eV and 61.11 eV, attributed to Ir1, IrB and Ir2, respectively. The line shapes for these components are identical to those found for the oxygen on bare Ir(111) discussed in section 6.3.2. The spectrum in figure 6.5 (a) demonstrates that, also under graphene, oxygen can reach a coverage of almost 0.66 ML, as in the case of the bare Ir(111) surface. Using the expression 6.1 for the determination of the oxygen coverage[19], we calculated a coverage of 0.64 ML. This result is in agreement with Larciprete et al., who found that for an intercalation temperature of 520 K, the oxygen coverage is θ ~0.6 ML[18]. Conversely, this value is in

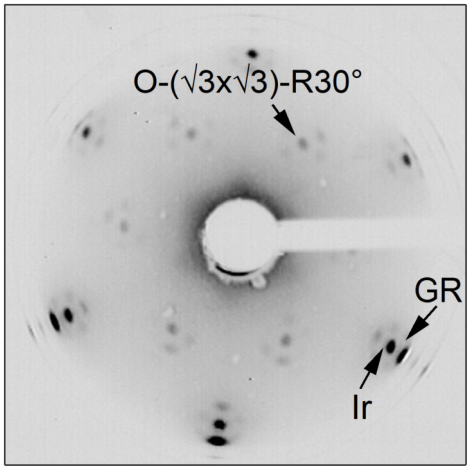

Figure 6.6: LEED pattern at 69 eV electron energy for oxygen intercalated under graphene on Ir(111) after O_2 dose. The LEED pattern was acquired at 77 K.

contrast with what asserted by Martinez-Galera et al, who found a maximum oxygen coverage under graphene of 0.5 ML[20].

Figure 6.6 (a) reports the LEED pattern after oxygen intercalation under graphene over Ir(111). The iridium main spots are surrounded by satellites spots due to the moiré superstructure given by the lattice mismatch between graphene (lattice constant $\alpha_{GR} \sim 0.246\,nm$) and the substrate ($\alpha_{Ir} \sim 0.271\,nm$). The inner spots, instead, form a ($\sqrt{3}$x$\sqrt{3}$)-R30° pattern. This pattern, as in the case of oxygen on bare Ir(111), can be attributed to a O-($\sqrt{3}$x$\sqrt{3}$) with a coverage of 0.33 ML, or to a 2O-($\sqrt{3}$x$\sqrt{3}$), with a 0.66 ML coverage. However, as reported in section 6.3.2, thanks to the knowledge of the oxygen coverage of 0.64 ML, the pattern shown in figure 6.6 (a) can only result from an almost complete 2O-($\sqrt{3}$x$\sqrt{3}$) structure.

6.3.4 XPD measurements

Thanks to LEED I/V measurements, already in 1979 it was found that on Ir(111) oxygen adsorbs in a three-fold coordinated site, namely hcp and fcc[37]. Subsequent theoretical studies pointed to the fcc site univocally[23, 33–35] but an experimental evidence, in particular for the oxygen adsorption under graphene, has not been provided yet. Larciprete et al. observed that the Ir $4f_{7/2}$ and O 1s spectra taken for the systems O/Ir(111) and GR/O/Ir(111) are very similar, suggesting that the oxygen adsorption site is the same on bare Ir(111) and under graphene[18]. In order to demonstrate that oxygen adsorbs in fcc-hollow sites also below graphene, we performed XPD measurements. In order to provide a compelling evidence that the oxygen sits in fcc sites, we first measured the XPD diffraction patterns of the Ir $4f_{7/2}$ core level to obtain the orientation of the substrate, reported in figure 6.7

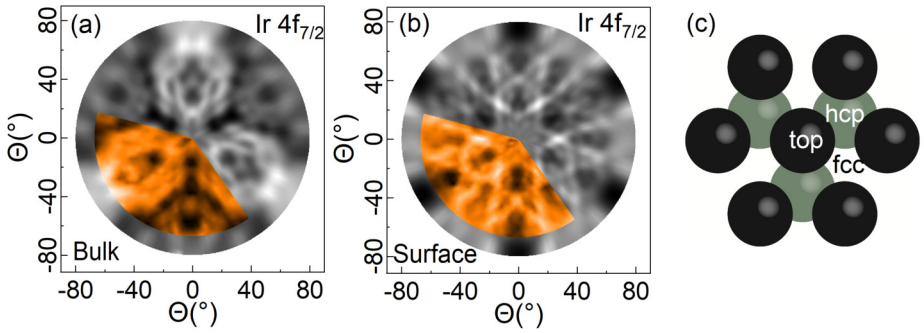

Figure 6.7: Stereographic projections of the integrated photoemission intensity modulation I(θ, ϕ) as a function of emission angle for Ir $4f_{7/2}$ (hν=180 eV; E_k ~115 eV) for the bulk (a) and surface (b). The colored sectors are the experimental data, while simulations are shown in grey. (c) Geometric structure used to simulate these patterns.

(a) and (b) for the bulk and the surface component, respectively. The bulk pattern is clearly 3-fold symmetric. The surface component, instead, shows a more pronounced 6-fold symmetry. The simulations were performed using four iridium layers and the very good agreement between the experiments and the simulations allows to define the orientation of the crystal as the one shown in figure 6.7 (c).

As in the case of the XPS and LEED measurements, we first performed the experiments on the O/Ir(111) system after the molecular oxygen dose, and the O 1s diffraction pattern, measured with a photon energy of hν= 620 eV was compared with simulations performed with a cluster made up of four layers of Ir(111) and oxygen adsorbed in fcc (figure 6.8 (a)) and hcp (figure 6.8 (b)) sites with O-Ir distance of 1.31 Å[33] at a kinetic energy of 90 eV. The experimental pattern is the colored region, while the simulations are in grey scale. Looking at the two simulations, as expected from the symmetry of the adsorbate structure, the patterns are threefold symmetric and the features displayed by the two simulations are similar but rotated by 180°. From a visual analysis, it is clear that the experimental pattern fits with the simulation where oxygen has been put in a fcc site, that is the one presented in figure 6.8 (a). Therefore, from this evidence, we demonstrate that the adsorption of oxygen on Ir(111) occurs in the fcc site.

As the oxygen coverage on this sample was more than 0.25 ML, in the simulation we included also part of a O-(2x1) structure. The R-factor analysis was done on patterns simulated mixing different percentage of O-(2x2) and O-(2x1) structure, finding the minimum when 70% of the O-(2x2) structure is present in the simulation. Therefore, in figure 6.9 (a), the experimental pattern is overlapped to a pattern made of 70% of the O-(2x2) structure and 30% of the O-(2x1) structure.

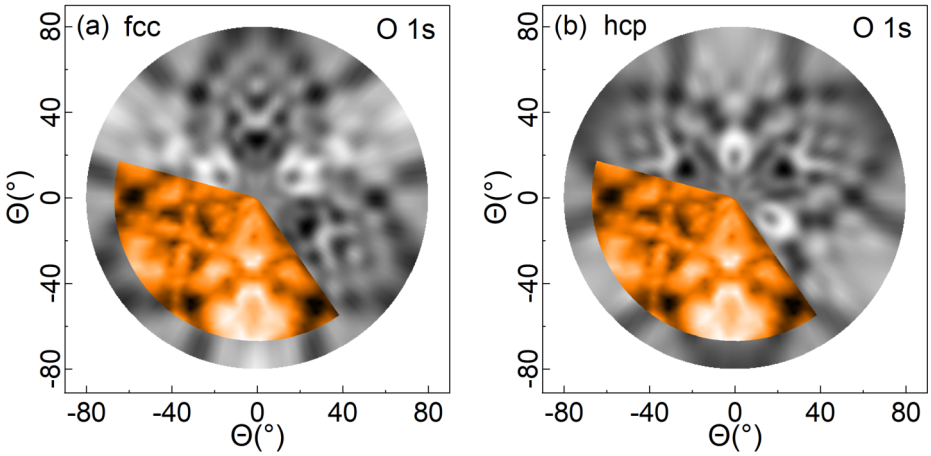

Figure 6.8: Stereographic projections of the integrated photoemission intensity modulation I(θ, ϕ) as a function of emission angle of O 1s core level (hν=620 eV; E_k ~90 eV) for the system O/Ir compared with simulations of O 1s for a (2x2) structure of oxygen sitting in (a) fcc and (b) hcp sites of the Ir surface. The colored sectors are the experimental data, while simulations are shown in grey.

We then performed XPD analyses for the system Gr/O/Ir(111) and the pattern is shown in figure 6.9 (b). In this simulation, we put four layers of Ir(111) and a 2O-($\sqrt{3}$x$\sqrt{3}$) oxygen structure in fcc sites. Graphene was not taken into account in the simulation, because of the lattice mismatch between graphene and both substrate and the structure formed by the adsorbed oxygen. The very good agreement between the experimental pattern and the simulation proves that also under graphene fcc sites are the favorite adsorption sites.

The XPD measurements were also used to find the O-Ir distance. The z position, measured as the height from the plane of the centers-of-mass of the top-layer iridium to the center-of-mass of the O atoms, was varied from 1.21 Å to 1.42 Å in the diffraction simulations and the R-factor was evaluated. The minimum of the curve falls on the z distance of 1.33 Å, as shown in figure 6.9 (c) for O/Ir system, in agreement with what theoretically predicted by Xu et al[33]. With the same procedure, we can confirm that also in the system GR/O/Ir, the z distance that minimizes the R-factor is 1.33 Å, as reported in figure 6.9 (d). This evidence proves that the presence of graphene does not affect the interaction between the adsorbed oxygen and the iridium substrate.

On this last sample, also the C 1s core level was probed and the resulting XPD pattern is shown in figure 6.10. This pattern is almost identical to that for the system Gr/Ir(111), reported in the literature[38]. The simulation has been done for a free-standing flat graphene layer at a kinetic energy of 115 eV. The similarity with the Gr/Ir(111) system and the excellent agreement

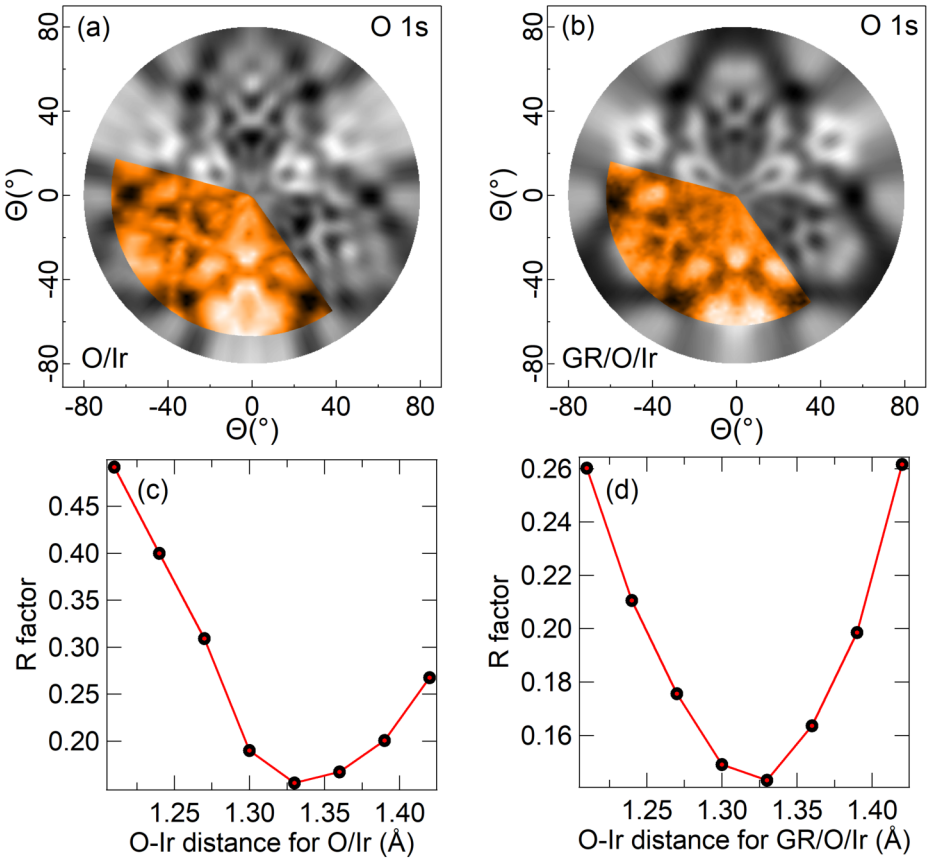

Figure 6.9: Stereographic projections of the integrated photoemission intensity modulation I(θ, ϕ) as a function of emission angle of O 1s core level (hν=620 eV; E_k ~90 eV) for the system (a) O/Ir and (b) GR/O/Ir. The colored sectors are the experimental data, while simulations are shown in grey. R-factor behavior for the O 1s diffraction patters, as a function of the distance between the oxygen atom and the Ir surface in the (c) O/Ir(111) and (d) GR/O/Ir(111) systems.

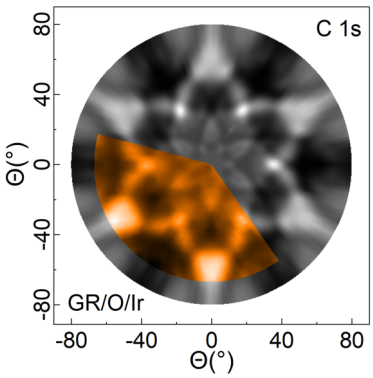

Figure 6.10: Stereographic projection of the integrated photoemission intensity modulation I(θ, ϕ) as a function of emission angle of C 1s core level for the system GR/O/Ir (hν=400 eV; E_k ~115 eV). The colored sector is the experimental data, while the simulation is shown in grey.

between experiment and simulation in figure 6.10 allows us to verify that oxygen does not produce appreciable changes to the graphene structure.

6.4 Conclusions

In this chapter, with the aim to verify whether the presence of graphene changes the adsorption geometry of the oxygen atoms on Ir(111), we studied the oxygen intercalation under graphene grown on Ir(111) and compared the results with those of oxygen adsorption on the bare Ir(111) surface by dosing molecular oxygen. We found that the graphene layer allows to reach a higher oxygen coverage on Ir, with the oxygen atoms sitting always in the same adsorption site, that was found to be the fcc hollow site. This may be due to the presence of graphene locking the O atoms close to the metal surface[18]. However, the same coverage of 0.66 ML can be reproduced on bare Ir(111) by dosing strongly oxidizing species such as NO_2. This leads us to conclude that graphene does not affect the adsorbate-substrate interaction because the same oxygen overlayers are obtained on both bare Ir(111) and under graphene grown on Ir(111).

References

[1] Batzill, M. The surface science of graphene: Metal interfaces, {CVD} synthesis, nanoribbons, chemical modifications, and defects. *Surface Science Reports* **2012**, *67*, 83–115.

[2] Wintterlin, J.; Bocquet, M.-L. Graphene on metal surfaces. *Surface Science* **2009**, *603*, 1841–1852.

[3] Voloshina, E.; Dedkov, Y. Graphene on metallic surfaces: problems and perspectives. *Physical Chemistry Chemical Physics* **2012**, *14*, 13502–13514.

[4] Sutter, P. W.; Flege, J.-I.; Sutter, E. A. Epitaxial graphene on ruthenium. *Nature Materials* **2008**, *7*, 406–411.

[5] Sicot, M.; Bouvron, S.; Zander, O.; Rüdiger, U.; Dedkov, Y. S.; Fonin, M. Nucleation and growth of nickel nanoclusters on graphene Moiré on Rh(111). *Applied Physics Letters* **2010**, *96*, 093115.

[6] Miniussi, E.; Pozzo, M.; Baraldi, A.; Vesselli, E.; Zhan, R. R.; Comelli, G.; Menteş, T. O.; Niño, M. A.; Locatelli, A.; Lizzit, S.; Alfè, D. Thermal Stability of Corrugated Epitaxial Graphene Grown on Re(0001). *Phys. Rev. Lett.* **2011**, *106*, 216101.

[7] Varykhalov, A.; Sánchez-Barriga, J.; Shikin, A. M.; Biswas, C.; Vescovo, E.; Rybkin, A.; Marchenko, D.; Rader, O. Electronic and Magnetic Properties of Quasifreestanding Graphene on Ni. *Physical Review Letters* **2008**, *101*, 157601.

[8] Merino, P.; Švec, M.; Pinardi, A. L.; Otero, G.; Martín-Gago, J. A. Strain-Driven Moiré Superstructures of Epitaxial Graphene on Transition Metal Surfaces. *ACS Nano* **2011**, *5*, 5627–5634.

[9] Murata, Y.; Starodub, E.; Kappes, B. B.; Ciobanu, C. V.; Bartelt, N. C.; McCarty, K. F.; Kodambaka, S. Orientation-dependent work function of graphene on Pd(111). *Applied Physics Letters* **2010**, *97*, 143114.

[10] Voloshina, E. N.; Generalov, A.; Weser, M.; Böttcher, S.; Horn, K.; Dedkov, Y. S. Structural and electronic properties of the graphene/Al/Ni(111) intercalation system. *New Journal of Physics* **2011**, *13*, 113028.

[11] Mao, J. et al. Silicon layer intercalation of centimeter-scale, epitaxially grown monolayer graphene on Ru(0001). *Applied Physics Letters* **2012**, *100*, 093101.

[12] Riedl, C.; Coletti, C.; Iwasaki, T.; Zakharov, A. A.; Starke, U. Quasi-free-standing epitaxial graphene on SiC obtained by hydrogen intercalation. *Physical Review Letters* **2009**, *103*, 246804.

[13] Wong, S. L.; Huang, H.; Wang, Y.; Cao, L.; Qi, D.; Santoso, I.; Chen, W.; Wee, A. T. S. Quasi-Free-Standing Epitaxial Graphene on SiC (0001) by Fluorine Intercalation from a Molecular Source. *ACS Nano* **2011**, *5*, 7662–7668, PMID: 21870857.

[14] Sutter, P.; Sadowski, J. T.; Sutter, E. A. Chemistry under cover: tuning metal-graphene interaction by reactive intercalation. *Journal of the American Chemical Society* **2010**, *132*, 8175–8179.

[15] Oida, S.; McFeely, F. R.; Hannon, J. B.; Tromp, R. M.; Copel, M.; Chen, Z.; Sun, Y.; Farmer, D. B.; Yurkas, J. Decoupling graphene from SiC(0001) via oxidation. *Physical Review B* **2010**, *82*, 041411.

[16] Coraux, J.; N'Diaye, A. T.; Busse, C.; Michely, T. Structural Coherency of Graphene on Ir(111). *Nano Letters* **2008**, *8*, 565–570.

[17] Starodub, E.; Bartelt, N. C.; McCarty, K. F. Oxidation of Graphene on Metals. *The Journal of Physical Chemistry C* **2010**, *114*, 5134–5140.

[18] Larciprete, R.; Ulstrup, S.; Lacovig, P.; Dalmiglio, M.; Bianchi, M.; Mazzola, F.; Hornekær, L.; Orlando, F.; Baraldi, A.; Hofmann, P.; Lizzit, S. Oxygen Switching of the Epitaxial Graphene-Metal Interaction. *ACS Nano* **2012**, *6*, 9551–9558.

[19] Grånäs, E.; Knudsen, J.; Schröder, U. A.; Gerber, T.; Busse, C.; Arman, M. A.; Schulte, K.; Andersen, J. N.; Michely, T. Oxygen Intercalation under Graphene on Ir(111): Energetics, Kinetics, and the Role of Graphene Edges. *ACS Nano* **2012**, *6*, 9951–9963.

[20] Martinez-Galera, A. J.; Schroder, U. A.; Huttmann, F.; Jolie, W.; Craes, F.; Busse, C.; Caciuc, V.; Atodiresei, N.; Blugel, S.; Michely, T. Oxygen orders differently under graphene: new superstructures on Ir(111). *Nanoscale* **2016**, *8*, 1932–1943.

[21] Bianchi, M.; Cassese, D.; Cavallin, A.; Comin, R.; Orlando, F.; Postregna, L.; Golfetto, E.; Lizzit, S.; Baraldi, A. Surface core level shifts of clean and oxygen covered Ir(111). *New Journal of Physics* **2009**, *11*.

[22] Marinova, T.; Kostov, K. Interaction of oxygen with a clean Ir(111) surface. *Surface Science* **1987**, *185*, 203 – 212.

[23] Zhang, H.; Soon, A.; Delley, B.; Stampfl, C. Stability, structure, and electronic properties of chemisorbed oxygen and thin surface oxides on Ir(111). *Physical Review B* **2008**, *78*, 045436.

[24] Pletikosić, I.; Kralj, M.; Pervan, P.; Brako, R.; Coraux, J.; N'Diaye, A. T.; Busse, C.; Michely, T. Dirac Cones and Minigaps for Graphene on Ir(111). *Physical Review Letters* **2009**, *102*, 056808.

[25] Zhdan, P.; Boreskov, G.; Boronin, A.; Egelhoff, W.; Weinberg, W. An XPS investigation of the chemisorption of oxygen on the iridium (111) surface. *Surface Science* **1976**, *61*, 25 – 36.

[26] Lizzit, S.; Baraldi, A.; Groso, A.; Reuter, K.; Ganduglia-Pirovano, M. V.; Stampfl, C.; Scheffler, M.; Stichler, M.; Keller, C.; Wurth, W.; Menzel, D. Surface core-level shifts of clean and oxygen-covered Ru(0001). *Physical Review B* **2001**, *63*, 205419.

[27] Ivanov, V.; Boreskov, G.; Savchenko, V.; Egelhoff, W.; Weinberg, W. The chemisorption of oxygen on the iridium (111) surface. *Surface Science* **1976**, *61*, 207–220.

[28] Davis, J. E.; Nolan, P. D.; Karseboom, S. G.; Mullins, C. B. Kinetics and dynamics of the dissociative chemisorption of oxygen on Ir(111). *The Journal of Chemical Physics* **1997**, *107*, 943–952.

[29] Malik, I. J.; Hrbek, J. Very high atomic oxygen coverages on Ru(001). *Journal of Vacuum Science & Technology A: Vacuum, Surfaces, and Films* **1992**, *10*, 2565–2569.

[30] Gsell, M.; Stichler, M.; Jakob, P.; Menzel, D. Formation and geometry of a high-coverage oxygen adlayer on Ru(001), the p(2x2)-3O phase. *Israel Journal of Chemistry* **1998**, *38*, 339–348.

[31] Banse, B. A.; Koel, B. E. Interaction of oxygen with Pd(111): High effective $\{O_2\}$ pressure conditions by using nitrogen dioxide. *Surface Science* **1990**, *232*, 275 – 285.

[32] Getman, R. B.; Schneider, W. F.; Smeltz, A. D.; Delgass, W. N.; Ribeiro, F. H. Oxygen-coverage effects on molecular dissociations at a Pt metal surface. *Physical Review Letters* **2009**, *102*, 076101.

[33] Xu, Y.; Mavrikakis, M. Adsorption and dissociation of O_2 on Ir(111). *The Journal of Chemical Physics* **2002**, *116*, 10846–10853.

[34] Krekelberg, W. P.; Greeley, J.; Mavrikakis, M. Atomic and Molecular Adsorption on Ir(111). *The Journal of Physical Chemistry B* **2004**, *108*, 987–994.

[35] Miller, S. D.; İnoğlu, N.; Kitchin, J. R. Configurational correlations in the coverage dependent adsorption energies of oxygen atoms on late transition metal fcc(111) surfaces. *The Journal of Chemical Physics* **2011**, *134*, 104709.

[36] Banhart, F.; Kotakoski, J.; Krasheninnikov, A. V. Structural Defects in Graphene. *ACS Nano* **2011**, *5*, 26–41.

[37] Chan, C. M.; Weinberg, W. H. Low energy electron diffraction structural analysis of the (2x2) oxygen overlayer on the iridium (111) surface. *The Journal of Chemical Physics* **1979**, *71*, 2788–2792.

[38] Lizzit, S.; Zampieri, G.; Petaccia, L.; Larciprete, R.; Lacovig, P.; Rienks, E.; Bihlmayer, G.; Baraldi, A.; Hofmann, P. Band dispersion in the deep 1s core level of graphene. *Nature Physics* **2010**, *6*, 345–349.

Chapter 7

Concluding remarks and outlook

This thesis investigates the growth of single-layer transition metal dichalcogenides, such as MoS_2 and WS_2, through physical vapor deposition. This class of materials indeed is of enormous interest in the scientific community thanks to their extraordinary properties that make them suitable for applications in the fields of electronics and optoelectronics. However, in order to exploit their innovative potential in technological devices, a growth approach capable to confer to the final product highly crystalline quality on a large scale is a bottleneck nowadays.

Here, we present a synthesis approach that allows to produce high quality samples in terms of crystalline order and size of the islands, with a single orientation for some systems. The structural properties have been demonstrated using a combination of surface science techniques, including synchrotron radiation photoemission and photoelectron diffraction. Angle-resolved photoemission was used to study the electronic structure of the synthesized samples.

In the first part of the thesis work, we investigated the dynamics of the growth of MoS_2 on Au(111) and we developed a new synthesis method for the formation of singly oriented domains. This finding may open the path to new concepts of devices based on the the spin and valley degrees of freedom.

Once the new growth procedure was optimized for the growth of MoS_2 on Au(111), we made a step further and studied the growth of MoS_2 on different substrates, that could have a higher interaction with the adlayer. In particular, we studied two Ag surfaces, Ag(111) and Ag(110). The same growth approach developed on Au(111), properly tuned, was used on the Ag(111) substrate, while a first step of "seeding" of MoS_2 nano-crystals using the TPG approach was found to be necessary to avoid randomly oriented domains on Ag(110). We verified the higher interaction between adlayer and substrate, as predicted by theoretical studies, and verified that this promotes

the formation of extended layers of MoS_2. Differently from the MoS_2/Au(111) system, here an equal amount of mirror domain aligned with the substrate is present. Moreover, the experimental findings indicate that MoS_2 on both Ag(111) and Ag(110) has metallic character. This result opens the path towards the development of MoS_2 based devices with low contact resistance.

With the aim of evaluating if the growth approach developed for MoS_2 was applicable also for the growth of other transition metal dichalcogenides, we moved to WS_2, a material relevant for technological applications thanks to the large spin splitting of the bands at the K point. By properly tuning the growth parameters, the procedure that was developed for the growth of MoS_2 on Au(111) was found to be suitable for the growth of singly oriented domains of single-layer WS_2 on Au(111).

To sum up, this thesis demonstrates that the growth of high quality single layers of transition metal dichalcogenides can be achieved on different substrates exhibiting variable interaction strength with the layer and also on substrates with a different symmetry. One of the major outcomes is represented by the development of a synthesis procedure to grow single-layer dichalcogenides with a single orientation. A step forward towards the realization of new devices based on these 2D materials exploiting also the single orientation character could be the development of methods for the lifting of the layers from the metallic substrates they are grown on, in order to transfer them onto insulating substrates, or to directly grow them on top of insulators. The knowledge acquired in this thesis work may be relevant for the production of high-quality single-layer transition metal dichalcogenides on different substrates and could be the key for the realization of devices featuring outstanding properties.

Acknowledgments

These three years of PhD have been a turning point for my personal growth. I discovered new attitudes that otherwise would have never surfaced. I ascribe this fact to the highly creative environment in which I lived and, of course, to the incredible people I had the honor to work with. I would like to start from my supervisor Silvano, who introduced me to a completely different branch of the scientific knowledge, the surface science, and a totally new way of doing experiments, such as UHV chambers and synchrotron radiation. I am grateful to him for having patiently raised me, and let me explore other activities related to the scientific research world. I have also to thank my co-supervisor Alessandro for his fundamental teaching at university and all the help for the completion of the PhD project. I have to mention all the colleagues of the SuperESCA beamline and the Surface Science Laboratory. Harsh, the best mate ever, the purest soul I have ever met; thank you in particular for the close and constant collaboration, these years would have been totally different without you. Luca, not just a colleague, but also a dear friend, with whom to share nice moments. Daniel, I am deeply indebted to you for helping me with the thesis, I do not need to spend further words, thank you. Paolo, beamtimes with you are funny, I liked working by your side. I have to mention also Rosanna, who hosted me in her laboratory in Frascati, and encouraged me to use the optical images of the experiments for photo contests. Big Luca, Davide, Dario, Franz, you helped me anytime I needed, you taught me how to make figures, how to use a tester, how to fit in Igor. Finally, I would like to acknowledge Christian, Gian, Luca, Naila and Nicoleta for the nice moments together. I have to thank all the Communication Office of Elettra for the possibility to get involved in their activity and a special thank goes to Bibi, who first recognized a value in my ideas and supported them. Michele, Cecilia and Giulia, without your support, I would have never entered the world of the European projects. I want in the end to thank my family for the care I received in these years, and Giulio, the best companion, supporter and buddy ever.

List of publications

Peer reviewed publications related to the PhD research project

1. Nicki Frank Hinsche, Arlette S. Ngankeu, Kevin Guilloy, Sanjoy K. Mahatha, Antonija Grubišić Čabo, Marco Bianchi, Maciej Dendzik, Charlotte E. Sanders, Jill A. Miwa, Harsh Bana, Elisabetta Travaglia, Paolo Lacovig, Luca Bignardi, Rosanna Larciprete, Alessandro Baraldi, Silvano Lizzit, Kristian Sommer Thygesen, and Philip Hofmann "Spin-dependent electron-phonon coupling in the valence band of single-layer WS_2" *Physical Review B* 96, 121402(R) (2017).

Submitted or in preparation manuscripts related to the PhD research project

1. Harsh Bana, Elisabetta Travaglia, Luca Bignardi, Paolo Lacovig, Charlotte E. Sanders, Maciej Dendzik, Matteo Michiardi, Marco Bianchi, Daniel Lizzit, Francesco Presel, Dario De Angelis, Nicoleta Apostol, Pranab Kumar Das, Jun Fujii, Ivana Vobornik, Rosanna Larciprete, Alessandro Baraldi, Philip Hofmann, and Silvano Lizzit "Synthesis of Single-Orientation High-Quality MoS_2 Monolayers with Complete Spin Polarization" *submitted, under review.*

2. Harsh Bana, Elisabetta Travaglia, Luca Bignardi, Paolo Lacovig, Daniel Lizzit, Charlotte E. Sanders, Maciej Dendzik, Matteo Michiardi, Marco Bianchi, Nicoleta Apostol, Rosanna Larciprete, Alessandro Baraldi, Philip Hofmann, and Silvano Lizzit "Synthesis of Single-Orientation High-Quality WS_2 Monolayers" *in preparation.*

3. Elisabetta Travaglia, Luca Bignardi, Paolo Lacovig, Daniel Lizzit, Harsh Bana, Rosanna Larciprete, Alessandro Baraldi, and Silvano Lizzit "Oxygen Adsorption on Ir(111) and its Intercalation under Graphene grown on Ir(111)" *in preparation.*

4. Elisabetta Travaglia, Harsh Bana, Luca Bignardi, Paolo Lacovig, Daniel Lizzit, Rosanna Larciprete, Alessandro Baraldi, and Silvano Lizzit "Large area epitaxial growth of MoS_2 on Ag(111)" *in preparation.*

5. Luca Bignardi, Harsh Bana, Elisabetta Travaglia, Paolo Lacovig, Daniel Lizzit, Sanjoy Kr. Mahatha, Rosanna Larciprete, Alessandro Baraldi, Philip Hofmann, and Silvano Lizzit "Growth of single layer MoS_2 on anisotropic Ag(110)" *in preparation.*

Other publications

1. Yujing Ma, Elisabetta Travaglia, Harsh Bana, Luca Bignardi, Paolo Lacovig, Silvano Lizzit, and Matthias Batzill "Periodic Modulation of Graphene by a 2D-FeO/Ir(111) Moiré Interlayer" *The Journal of Physical Chemistry C* 121 (5), 2762-2770 (2017).